Coherent Control of
ᵐᵒˡᵉᶜᵘˡᵃ Rydberg Wave Packets in NO

Russell Stephen Minns

A thesis submitted in
partial fulfilment of
the degree of
Doctor of Philosophy

University College London
University of London
April 2005

UMI Number: U592156

Dissertation Publishing

For my Family

Acknowledgements

I Must firstly thank Prof. Helen Fielding for every thing she has done over the past four years. Her unyielding support and optimism, in the face of absolute doom has been nothing short of remarkable. Thanks must also go to Prof. Christian Jungen who made me feel so welcome on my visits to Paris, and managed to explain the complexities of MQDT in words of one syllable or less so that even an experimental chemist could understand it.

I have also had great pleasure in working with some fantastic people in the group. I owe a great deal to Jan Verlet and Vas Stavros who taught me absolutely everything there is to know about their bowel movements, as well as quite a lot about Rydberg wave packets and laser systems. They were both always willing to answer any stupid questions I had, and helped me get my head around some of the complexities of Rydberg states. Thanks must also go to Rakhee Patel who has always been there to blame when something goes wrong and whom I have had great pleasure in working with on a number of experiments, even if most of them didn't work. I would also like to thank everyone else who has worked in the lab over the years and made it such a fantastic place to be; especially Rob Carley, whose action man knee pads and knowledge of knots was always a source of fun, and Lizzy Boléat, whose love of The Carpenters meant the lab was always full of beautiful music. Both have helped on so many bits and pieces over the past few years that I am sure none of this would have been possible without them.

A big thank you to Dick Waymark at UCL technical support for all the components he has made and fixed for us, and to the chemistry workshop, especially Jim Stevenson, for building a number of things, in particular the most intricate ramp I think the world has ever seen. Also thanks to everyone at Photonic solutions and Coherent; particularly Dave Creasey, Darryl McCoy and Sean McCormack, for answering all my phonecalls.

Finally I must thank Katherine for all her love and support over the past 4 years.

Coherent Control of Molecular Rydberg Wave packets in NO

Russell Stephen Minns
University College London, 2005

Abstract

New experiments and theory contributing to the understanding of the dynamics and control of molecular Rydberg wave packets are presented.

An intuitive scheme for controlling the rotational quantum state of a Rydberg molecule is demonstrated experimentally. We determine the accumulated phase difference between the various components of a molecular electron wave packet, and then employ a sequence of phase-locked optical pulses to selectively enhance or depopulate specific rotational states. The angular momentum composition of the resulting wave packet, and the efficiency of the control scheme, is determined by calculating the multipulse response of the time dependent Rydberg populations.

The dynamics of predissociating Rydberg electron wavepackets are observed using the optical Ramsey method. The time-resolved spectra are hydrogenic and are very well modeled by assuming that only one p Rydberg series contributes to the dynamics. This is in contrast with previous observations of autoionising Rydberg electron wave packets which show quite dramatic deviations from hydrogenic behaviour above the Born-Oppenheimer limit. The origin of these deviations lies in the interplay between electronic and molecular phase. By exploiting these phases we are able to control the ratio of predissociaton to autoionisation

A multichannel quantum defect theory analysis of the Rydberg state of NO is undertaken. The analysis takes into account all the accessible series with $l \leq 3$ and all documented interseries interactions. This analysis is the most complete description of NO to date and will aid in the design of future coherent control experiments.

This thesis is based on the following publications

Chapter 3

Optical control of the rotational angular momentum of a molecular Rydberg wave packet.
R.S. Minns, R. Patel, J.R.R. Verlet and H.H. Fielding.
Phys. Rev. Lett. **91**, 243601 (2003)

Chapter 4

Observation and control of autoionising and predissociating Rydberg electron wave packets in NO.
R.S. Minns, J.R.R. Verlet, L.J. Watkins and H.H. Fielding.
J. Chem. Phys. **119** (12), 5842 (2003)

Chapter 5

Global MQDT representation of the NO molecule.
R.S. Minns, J.W. Hepburn, H.H. Fielding and Ch. Jungen.
J. Mol. Spec. In preparation

Additional publications

Controlling the angular momentum composition of a Rydberg electron wave packet.
J.R.R. Verlet, V.G. Stavros, R.S. Minns and H.H. Fielding.
Phys. Rev. Lett. **89** (26), 263004 (2002).

Controlling the radial dynamics of Rydberg wave packets in Xe using phase-locked optical pulses.
J.R.R. Verlet, V.G. Stavros, R.S. Minns and H.H. Fielding.
J. Phys. B-At. Mol. Opt. Phys. **36** (17), 3683 (2003).

Interfering Rydberg wave packets in Na.
R.E. Carley, E.D. Boléat, R.S. Minns, R. Patel and H.H. Fielding
J. Phys. B-At. Mol. Opt. Phys. In preparation

Table of contents

4 Observation of a dissociating Rydberg electron wave packet and control of the autoionisation:predissociation ratio in NO.

5 Global MQDT representation of the NO molecule

6 Concluding remarks

Table of figures

Table of tables

Chapter 1: Introduction

1.1. Introduction to coherent control

Using coherent light to control the chemical and physical properties of atoms and molecules has been a dream in chemical physics since the advent of the laser. Many different approaches have been devised and implemented on systems ranging in size from atomic [1-8], to biological [9]. Generally speaking, all the control schemes can be divided into two subtypes: control in the time domain or frequency domain control.
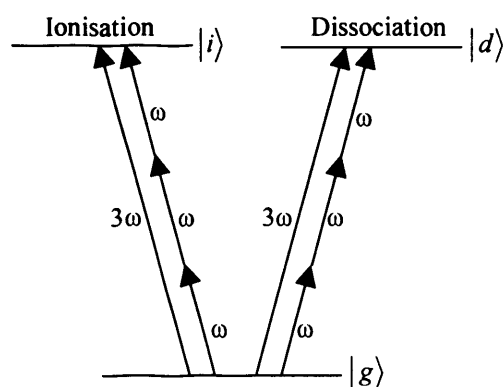
Figure 1.1. Schematic representation of the Brumer-Shapiro scheme used to control the ionisation:dissociation branching ratio in DI. One- and three-photon pathways to both continua are allowed, and by changing the phase difference between the two pathways the total population in either channel can be manipulated.

In the frequency domain approach, usually narrow bandwidth nanosecond or continuous wave (CW) lasers are used to selectively populate a final state or control a

product branching ratio. The two most important schemes are the Brumer-Shapiro [10,11] and STIRAP [12] methods. The scheme first proposed by Brumer and Shapiro is based on the interference of multiple paths to a particular final state. If two excitation pathways to a particular final state exist, the final population is dependent on the relative phases of the two pathways. Controlling the relative phase therefore controls the final state population. The Brumer-Shapiro approach has been demonstrated widely. For example it has been used to control population transfer [13-15] and branching ratios [16-19]. Consider the case of a highly excited-state embedded in both ionisation and dissociation continua. Simultaneous single- and multi-photon excitation leads to a population dependent on the relative phase of the two light pulses. The phase required to maximize the population in the ionisation channel is termed δ_I, while the phase required to maximize the population in the dissociation channel is termed δ_D. If δ_D does not equal δ_I then the ionisation:dissociation ratio can be controlled. The difference between δ_D and δ_I is called the phase lag, and a phase lag of π, provides a system in which maximum control can be achieved. This is because when the phase lag is π, the phase required to maximise the ionisation signal is also the phase required to minimise the dissociation signal. The Gordon group elegantly demonstrated this principle in DI [20-22]. Here, competing one- and three-photon processes provide pathways to ionisation and dissociation continua, and the phase lag in DI is approximately π.

For complete population transfer another method is required. Stimulated Transition Induced by Raman Adiabatic Passage (STIRAP) provides one such route. Consider a three state system with a ground state $|1\rangle$, an excited state $|2\rangle$ and final state $|3\rangle$, in which complete population transfer from state $|1\rangle$ to state $|3\rangle$ is desired. A laser

pulse of frequency ω_{23}, couples states $|2\rangle$ and $|3\rangle$ creating a dressed state, and a delayed, but overlapping laser pulse of energy ω_{12} then couples state $|1\rangle$ to the dressed state causing population to be transferred from state $|1\rangle$ to state $|3\rangle$ adiabatically. ω_{23} is switched off before ω_{12}, preventing population returning from state $|3\rangle$ to state $|1\rangle$. Any internal decay processes of state $|2\rangle$ do not hinder this technique as the population in state $|2\rangle$ is kept to a minimum by the adiabatic process. 100% population transfer has been demonstrated using such methods in many atomic [23,24] and larger [25-30] systems.
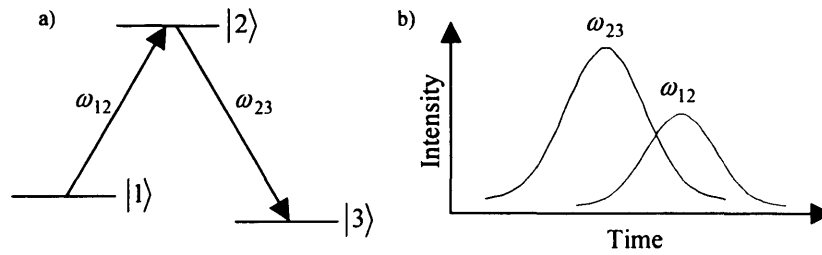
Figure 1.2.Schematic representation of the a) energy level diagram and b) relative pulse timings used in the STIRAP control experiments. A laser pulse of frequency ω_{23} couples states $|2\rangle$ and $|3\rangle$ creating a dressed state, and a delayed, but temporally overlapping laser pulse of frequency ω_{12} then couples state $|1\rangle$ to the dressed state, causing population to be transferred from state $|1\rangle$ to state $|3\rangle$ adiabatically. ω_{23} is switched off before ω_{12}, stopping population returning from state $|3\rangle$ to state $|1\rangle$.

Of most relevance to the work described in this thesis is the time domain approach to coherent control, first discussed by Tannor, Koslof and Rice [31-33]. Broad bandwidth picosecond or femtosecond lasers excite several states coherently; this creates a wave packet, a wave packet is a spatially localised state which evolves with time. Once the wave packet has evolved to a specific position on its potential surface, a second optical pulse can be employed to pump or dump the wave packet onto another

potential surface leading to the desired products. By controlling the time delay between the two pulses, different potential surfaces become accessible and different products can often be attained. Baumert *et al* first demonstrated such control over the ionisation and dissociative ionisation of Na_2 [34-36]. In their experiment, a vibrational wave packet is launched on an excited state potential. The wave packet moves between the classical turning points corresponding to a fully stretched and fully compressed bond. A second laser pulse is then used to ionise the system. If the second laser pulse arrives when the wave packet is at the inner turning point, the molecule is ionized to give Na_2^+, while if the second laser pulse arrives when the wave packet is at the outer turning point, a different potential surface is reached and the molecule dissociatively ionises to give $Na^+ + Na$. Different products are therefore obtained depending on the time delay between the two pulses.

More recently, there has been a great deal of interest in another related time domain approach. Pulse-shaping techniques, which control the phase, amplitude and polarisation of the spectral components of the light pulse, manipulate the composition of the wave packet and thus the ensuing motion. The power of this technique has been harnessed by combining pulse-shaping equipment with feedback controlled learning algorithms [37]. The sample is exposed to a number of random pulse shapes and the products are detected. The pulse shapes that perform best at the chosen task; be it the generation of a desired product or enhanced population of a particular state, are taken onto the next generation, while the weaker pulse shapes are dumped. The fittest pulses are then bred to form a new selection of pulse shapes and this iterative process continues until the optimal pulse shape is achieved. The laser is essentially taught the optimal pulse shape for a given process. Using this method no prior knowledge of the system is required. This approach has been employed successfully with a wide number

4

of complex molecules yielding some quite remarkable results [9,38-48]. However, the pulse shapes produced are often extremely complex and can obscure the underlying control mechanism, making it extremely difficult to learn much from these experiments. As impressive as the feedback-controlled experiments are, it is often more useful to study logical control schemes in simpler systems in order to build up a picture of how the more complex pulse shapes work. Previous work on atomic Rydberg electron wave packets has provided excellent opportunities for such experiments. In the rest of this chapter, we aim to introduce the basic principles behind Rydberg electron wave packets, before discussing some of the more important coherent control experiments on these systems. In the final section molecular Rydberg electron wave packets will be introduced in the context of extending coherent control from atomic to molecular Rydberg systems.

1.2. Radial Rydberg wave packets

1.2.1. Rydberg wavefunctions

A good place to start when discussing Rydberg states is the Rydberg equation [49]

$$E = -\frac{R}{(n-\mu)^2} \qquad (1.1)$$

which gives the energy, E, of state n, where n is the principal quantum number, μ is the quantum defect and R is the Rydberg constant, which can be derived from Bohr theory and Newton's equation of motion. Rydberg states are often defined as high-energy

electronic states, and the large radial distribution functions of these states means they have very little overlap with the remaining ionic core. The Rydberg electron consequently only sees the core as a +1 point charge. By describing the Rydberg electron as moving in the Coulomb potential of the core, we can derive the origin of the Rydberg equation and see why it has such wide applicability.

First consider the Rydberg states of an atom with energies in atomic units,

$$E = -\frac{1}{2v^2}$$
(1.2)

where v is the effective principal quantum number and can be thought of as just another measure of the energy of the Rydberg state. Let us also start by considering the Rydberg states of hydrogen. Hydrogen has only one electron; the electron therefore feels the +1 Coulombic potential of the core regardless of its radial position. This purely Coulombic attraction means the radial Schrödinger equation simplifies to the Coulomb function [49],

$$\left[-\frac{1}{r}\left(\frac{d^2}{dr^2} - \frac{\ell(\ell+1)}{r^2} \right) + [V(r) - E] \right] \psi_l(v,r) = 0.$$
(1.3)

Equation 1.3 has two linearly independent solutions, the regular, $f(v,r)$, and irregular, $g(v,r)$, Coulomb functions. The names refer to the behaviour of the functions at the origin, i.e. the regular function is finite as $r \rightarrow 0$ while the irregular function blows up as $r \rightarrow 0$, where r is the distance of the electron from the ion core. Other Coulomb basis functions can be chosen, but the f and g functions are the ones most

commonly used. In larger many electron systems we set up a boundary between two regions, r_c. In the core region, $r < r_c$, the Rydberg electron feels the complex potential produced by the higher charge of the nucleus, as well as the repulsive forces of the other electrons. Outside the core region, $r > r_c$, the Rydberg electron sees the +1 Coulombic potential of the core like the hydrogenic case. The radial wavefunction of the Rydberg electron at distances $r > r_c$ in many electron systems, and at all distances for hydrogen, can then be described as a superposition of the regular and irregular Coulomb waves,

$$\Psi(v,r) = af(v,r) + bg(v,r) \tag{1.4}$$

where a and b are the weightings of the two Coulomb waves. The wavefunction must be normalised so that $|a|^2 + |b|^2 = 1$, where a and b are often given the form,

$$\begin{aligned} a &= +\cos\pi\mu \\ b &= -\sin\pi\mu \end{aligned} \tag{1.5}$$

Equation 1.5 shows how the weighting of the two functions depends only on μ, the quantum defect. If $\mu = 0$ only the regular function contributes, while if $\mu = \frac{1}{2}$ then only the irregular function contributes. In hydrogen the radial wavefunction must be valid for all r values, including $r = 0$. Therefore only the regular Coulomb wave can contribute to the wavefunction, resulting in the quantum defect for hydrogen being zero. This simplification does not hold for larger systems, we must therefore continue building the wavefunction for many electron systems. So far we have only considered the radial part of the wavefunction at distances of $r > r_c$; however it does have an angular component,

as well as continuing into the core region. The total wavefunction of the Rydberg electron must therefore contain these factors and the total wavefunction can now be written as,

$$\Psi(v,r) = |\varphi\rangle[\cos(\pi\mu)f(v,r) - \sin(\pi\mu)g(v,r)] \tag{1.6}$$

where $|\phi\rangle$ is the wavefunction of the electronic angular and core components. By applying boundary conditions and considering the behaviour of the two Coulomb functions as $r \to \infty$, the appropriate wavefunction can be derived. For the classically allowed region, $E < 0$, as $r \to \infty$, the asymptotic forms of the regular and irregular Coulomb functions are,

$$f(v,r \to \infty) \to C(r)\sin\pi(v-\ell)e^{r/v}$$
$$g(v,r \to \infty) \to -C(r)\cos\pi(v-\ell)e^{r/v} \tag{1.7}$$

where $C(r)$ is a function which tends to zero slower than the exponential term blows up, and ℓ is the orbital angular momentum. The total wavefunction is now,

$$\Psi(v,r \to \infty) = 0 = [\cos(\pi\mu)\sin\pi(v-\ell) + \sin(\pi\mu)\cos\pi(v-\ell)]C(r)e^{r/v}|\phi\rangle. \tag{1.8}$$

For bound states as $r \to \infty$, $\Psi \to 0$. For equation 1.8 to be zero the term in square brackets must be zero. As ℓ is an integer this leads to,

$$[\tan\pi v + \tan\pi\mu] = 0 \tag{1.9}$$

which in turn leads to

$$\sin \pi(v + \mu) = 0 \qquad (1.10)$$

and equation 1.10 has solutions,

$$v + \mu = n \quad \Rightarrow \quad n = 0, \pm 1, \pm 2, \pm \ldots\ldots \qquad (1.11)$$

however the only physically meaningful answers are when,

$$n = \ell + 1, \ell + 2, \ldots\ldots \quad \text{and} \quad v = n - \mu \qquad (1.12)$$

We now have the values of the effective principle quantum number, v, for the bound states of a system and have derived the Rydberg equation (equation 1.1). As the wavefunction is energy independent, the energy is not imposed on the system until the final step, the wavefunction describes a complete series and associated ionisation continua, and this is termed a channel. As we saw earlier, hydrogen has no quantum defect; the quantum defect is therefore the phase shift of the Rydberg wavefunctions, $\pi\mu$, and the energy shift, see equation 1.1, of the Rydberg states when compared with the hydrogenic series. By looking at the effective potential the electron feels at different radial distances we can get a physical understanding of where the phase shift comes from. Consider a square well potential with an infinite barrier at $r = 0$ and a finite barrier at $r = r_c$. When the electron is at a distance $r > r_c$ the electron only feels a small attractive potential and therefore has a relatively high energy and short deBroglie wavelength. At distances $r < r_c$ the electron feels the larger potential of the core,

lowering its energy and therefore increasing the deBroglie wavelength. Depending on the depth of the square well, the outer wave must be shifted from the hydrogenic wave in order to form a continuous wavefunction. This Coulomb wave approach is the basis of quantum defect theory (QDT) [50,51] and has been applied to a wide number of problems in atomic physics. The reason for its wide applicability is the fact the quantum defect is nearly energy independent, therefore an entire Rydberg series can be described using only a few parameters. This basis can also be extended to describe the Rydberg states of molecular systems [52-55], including the competing ionisation and dissociation processes [56-58] and wave packet motion [59], and will be discussed in more detail in chapter 5.

1.2.2. Radial Rydberg wave packets

From equation 1.1, it is clear that the energy levels converge as n increases. This convergence allows several high n states to be excited simultaneously using the broad bandwidth output of a picosecond or femtosecond laser, allowing you to tune the time scale of the system to your equipment. Exciting several states differing only in n, creates a wave packet localised in the radial coordinate which is described mathematically as,

$$\Psi(r,t) = \sum_n a_n \psi_n(r) \exp(-i\omega_n t) \tag{1.13}$$

In equation 1.13 the sum is over all the Rydberg states within the wave packet, a_n is the population coefficient and depends on the transition dipole moments and laser pulse

profile; ω_n is the angular frequency of the Rydberg state, t is time and $\psi_n(r)$ is the time-independent radial wavefunction. The wave packet oscillates between the inner and outer turning points of the Coulomb potential, with a period of $t_{cl} = 2\pi n^3$, and this oscillation is analogous to the classical dynamics of a Bohr electron in a classical atom. The classical picture eventually breaks down due to the anharmonicity of the Coulomb potential. The anharmonicty causes the wave packet to spread, until it covers the entire radial co-ordinate. At this point interference effects cause well localised portions of the wave packet to be formed around the radial co-ordinate. These are known as fractional revivals, as part of the wave packet is seen at the core region at fractions of the original frequency. Eventually the wave packet revives to form something resembling the original wave packet and this is called a full revival.
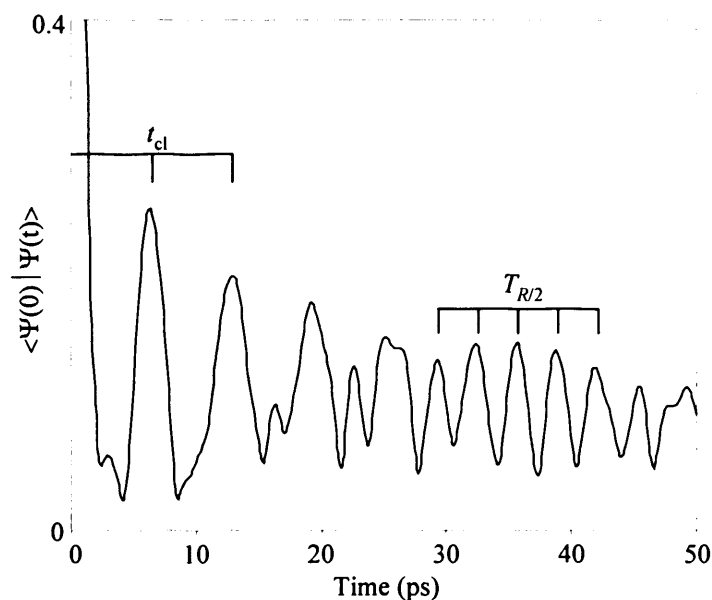
Figure. 1.3.Calculated wave packet spectrum of NO at an energy n = 37, calculated using the experimental intensities and energies obtained in a frequency resolved experiment. The recurrence spectrum shows clear recurrences with a classical period of 6.4 ps with a second order partial revival around 35 ps

11

In figure 1.3 a theoretical recurrence spectrum is presented, the spectrum was calculated using $\langle \Psi(0)|\Psi(t)\rangle = \sum_n a_n \exp^{-i\omega_n t}$. Peaks appear when the wave packet is at the core, while dips appear when the wave packet is away from the core. These fundamental motions have been thoroughly studied in many atomic systems [60-70] and are now well understood. The motion can be explained as follows: we start by defining the period of a quantum beat,

$$t_{cl} = \frac{2\pi}{\Delta E}$$ (1.14)

where ΔE is the energy spacing. The energy spacing between Rydberg states scales as n^{-3}, the classical period of a Rydberg wave packet according to equation 1.14 is therefore,

$$t_{cl} = 2\pi \bar{n}^3 .$$ (1.15)

where $\bar{n}$ is the average principal quantum number of the wave packet. The spacing between each pair of states will be slightly different, and each energy spacing has its own fundamental period, and this causes the wave packet to disperse. The subsequent evolution of the wave packet can be explained by taking a Taylor's expansion of the energy [71]:

$$\omega_n = -\frac{1}{2\bar{n}^2}\left[1 + 2\left(\frac{\delta n}{\bar{n}}\right) - 3\left(\frac{\delta n}{\bar{n}}\right)^2 + ...\right]$$ (1.16)

The first term in square brackets gives the average energy of the wave packet; the term linear in n is the harmonic term giving equal energy spacing between all the states and this defines the classical orbit period (equation 1.15). The quadratic term adds the anharmonicity of the potential and accounts for dispersion effects including the eventual re-phasing of the wave packet at the full revival time,

$$T_R = \frac{3}{2}\bar{n}t_{cl}$$
(1.17)

Fractional revivals are seen at fractions of the full revival time. An nth order partial revival, where n is an integer, is seen at times T_R/n. At these times n fractions of the wave packet are seen to pass the core region at regular intervals, all with a well known phase difference, as derived analytically by Averbukh and Perelman [72]. Higher order terms in the Taylor's expansion account for higher orders of anharmonicity leading to such phenomena as super-revivals [73].

1.3. Coherent control of Rydberg electron wave packets

In this section, some coherent control schemes specific to Rydberg wave packets will be introduced and in each area, a few highlighted cases will be explained in more depth. These cases are often the most interesting examples and are based on intuitive ideas, where the control mechanism can be explained from the outset.

1.3.1. Interfering wave packets

The dynamics of interfering wave packets has been at the heart of some of the more interesting coherent control schemes in electronic [1-3,5,65,68-70,74] and molecular (vibrational and rotational) [75-80] wave packets. Interfering Rydberg wave packets have been used to create exotic Schrödinger cat states [3,70], reproduce Young's double slit experiment in an atom [2] and to control the orbital angular momentum character of a wave packet with mixed angular momentum character [5]. In this section we aim to highlight some of these and other important examples of interfering wave packets.

Although technically not a coherent control experiment, the Optical Ramsey Method [74] (ORM) of detection is possibly the most important example of interfering wave packets. By monitoring the interference fringes produced when two identical but time delayed wave packets are excited, it is possible to measure the evolution of the first wave packet. Consider a wave packet created at the core region; it begins its orbit by leaving the core region and moving to the outer turning point before returning to the core periodically. If a second wave packet is excited before the first wave packet has left the core, it can either be in phase with the initial wave packet enhancing the Rydberg population (this gives a Rydberg population of $4A^2$, where A is the amplitude of a single wave packet), or out of phase with the initial wave packet pumping the initial population back down to the ground state (leaving a total Rydberg population of zero). As the phase difference between the two wave packets is scanned, interference fringes are seen in the total Rydberg population when the initial wave packet is in the core region. If the first wave packet is away from the core region at the time the second wave packet is excited, there is no interference between the two wave packets. The Rydberg population is therefore independent of the relative phase between the two wave packets,

the Rydberg population remains constant (a Rydberg population of $2A^2$, the incoherent sum of the two individual wave packets) regardless of the phase difference. At the first recurrence a similar picture to that of $t = 0$ is correct, however, the total population will not oscillate between $4A^2$ and zero due the effects of dispersion which will reduce the overlap of the two wave packets and thus their interference. The amplitude of the fringes gives a measure of how much of the wave packet is at the core. This detection method provided a marked improvement on the signal to noise ratio available when studying Rydberg wave packets compared to earlier pump-probe experiments which, due to the low ionisation probabilities of Rydberg states, provided very low signal levels.
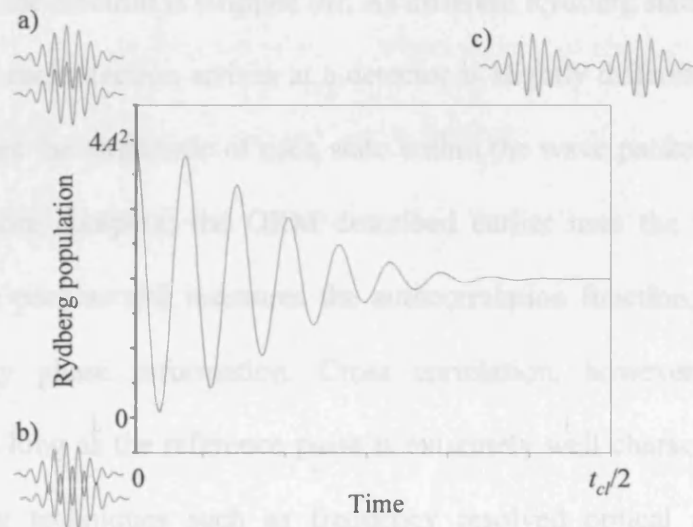
Figure 1.4. Ramsey fringes seen in the Rydberg population, around t = 0, as the phase difference between two light pulses is changed. Cartoon a) shows constructive interference between the two wave packets giving an enhanced Rydberg population of 4A². As the phase of the second wave packet is scanned, the total Rydberg population is altered. When the two wave packets are out of phase (cartoon b)) destructive interference removes all of the Rydberg population. If the delay between the two wave packets is increased so that there is no overlap between them (cartoon c)), no interference can take place and the Rydberg population remains at a constant level regardless of phase.

The problem with the ORM and other detection methods is that they do not allow the measurement of the complete wavefunction of the wave packet. An experiment by Weinacht *et al* [7,8] has used the interference of wave packets in order to fully characterize an unknown shaped wave packet. By measuring the phase and amplitude of all the states within the wave packet, the complete wavefunction may be determined. This is achieved using a cross correlation technique, with a well-characterized reference pulse, combined with state selective field ionisation (SSFI) [49]. SSFI allows direct measurement of the amplitudes of the Rydberg states within the wave packet. By applying a slowly rising DC electric field, the saddle point of the Coulomb potential is lowered, and as the saddle point passes the energy of each Rydberg state, the electron is stripped off. As different Rydberg states ionise at different fields the time each electron arrives at a detector is slightly different. This allows us to directly measure the amplitude of each state within the wave packet. The measurement of phase is more complex; the ORM described earlier uses the interference of two identical wave packets and measures the autocorrelation function, and it is therefore devoid of any phase information. Cross correlation, however, can yield phase information as long as the reference pulse is extremely well characterised. This can be achieved using techniques such as frequency resolved optical grating (FROG) or spectral phase interferometry for direct electric field reconstruction (SPIDER). The interference between the arbitrary wave packet and the reference wave packet modifies the population of each of the states within the wave packet. By analysing this change over time, the relative phase of each state can be obtained. Complete characterisation of the wave packet is therefore achieved; this methodology has also been suggested as a possible route to using Rydberg wave packets for quantum computing [6].

So far we have only considered wave packets made up of one Rydberg series. Wave packets excited in Xe contain both $nd[3/2]_1$ and $ns[3/2]_1$ Rydberg series. The states are labelled using the jl coupling nomenclature $nl[K]_J$, with $K = j^+ + l$ and $J = K + s$, where j^+ is the total angular momentum of the ion core, l is the orbital angular momentum of the Rydberg electron and s is the spin of the Rydberg electron. By interrogating the phase evolution of the two series, it was possible to selectively populate one or other Rydberg series [5]. Consider a wave packet composed of a superposition of two non-interacting Rydberg series, with different orbital angular momenta l and quantum defects μ_l, converging to the same ionisation limit. Such a wave packet may be considered as being composed of two separate components and is written $\Psi(r,t) = \Sigma_{nl} a_{nl} \psi_{nl}(r) \exp(-i\omega_{nl}t)$, where $\psi_{nl}(r)$ is the radial wavefunction of the eigenstate $|nl\rangle$, $\omega_{nl} = -1/2(n - \mu_l)^2$ is its frequency and a_{nl} is its amplitude in the superposition. After an integer number of orbit periods k, each wave packet, corresponding to a channel l, accumulates a phase $2\pi k\mu_l$, resulting in an accumulated phase-difference between the two wave packets, $\phi_l = 2\pi k\Delta\mu_l$. In the case of the Xe wave packet $\Delta\mu_l = 0.22$. Thus when $k = 2$, i.e. after two orbit periods, $\phi_l \approx \pi$ and the phases of the paths coupling the two angular momentum components to the initial state are mismatched. If a second wave packet is launched at this time, it can be created so that it interferes constructively with the s component of the evolved wave packet and destructively with the d component, or *vice versa*. In this way, the orbital angular momentum character of the electron wave packet and hence the shape is controlled.

1.3.2. Half cycle pulses

Wave packets can only be manipulated by light when they are at the core, limiting what control experiments can achieve using optical fields. Half Cycle Pulses (HCPs) are essentially unipolar electric fields that can impart momentum onto the wave packet, irrespective of its radial position, and can therefore be extremely useful in determining and modifying wave packet motion away from the core [81]. HCP's are produced by illuminating, with femtosecond light, a biased semiconductor wafer. The illumination rapidly accelerates electrons from the insulating band to the conduction band; this acceleration produces a unipolar field that propagates away from the wafer. After the femtosecond pulse, the electrons slowly relax down to the insulating band, producing an opposite unipolar field. The initial rapid acceleration produces a field in the direction of the applied bias with a duration of approximately 1 ps. The subsequent slow relaxation creates a tail of opposite polarity, which is many times smaller than the initial field (typically 5-10 times smaller) and has a duration of hundreds of picoseconds. The final pulse therefore resembles an optical pulse that has only undergone half an oscillation [82]. A typical HCP profile is depicted in figure 1.5.
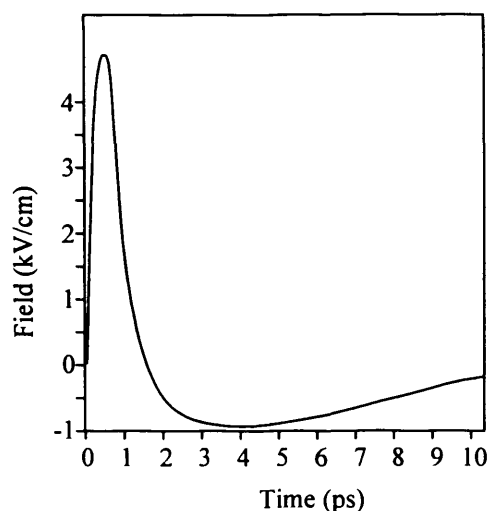
Figure 1.5. Typical shape of a HCP with a large, narrow, typically 1 ps, unipolar electric field, followed

by a small, wide (typically 100 ps) tail of opposite polarity.

HCP's have been used to create three dimensionally localized wave packets [83,84], to recombine ions with recently ionised electrons [85] and to measure the quantum state [86] and momentum distribution of a Rydberg wave packet [87]. Possibly the most interesting of these experiments is the three dimensionally localized wave packet. Early experiments on Rydberg wave packets were often interested in studying the correspondence principle. By creating an electron wave packet localised in all three dimension a true analogue to the classical electron can be produced. The method of production was initially put forward by Gaeta, Noel and Stroud in 1994 [84], and was first demonstrated by Bromage and Stroud in 1999 [83]. The method involves exciting a stationary state localised around an elliptical orbit. A HCP polarised along the direction of the orbit then further localises the state in the radial coordinate. A classical explanation of this is as follows; the stationary state can be thought of as an ensemble of classical particles distributed around the orbit. The HCP gives a momentum kick to all of the classical particles in the direction of polarisation, and each particle will therefore receive a different push causing all the particles to eventually overlap (figure 1.6).

19
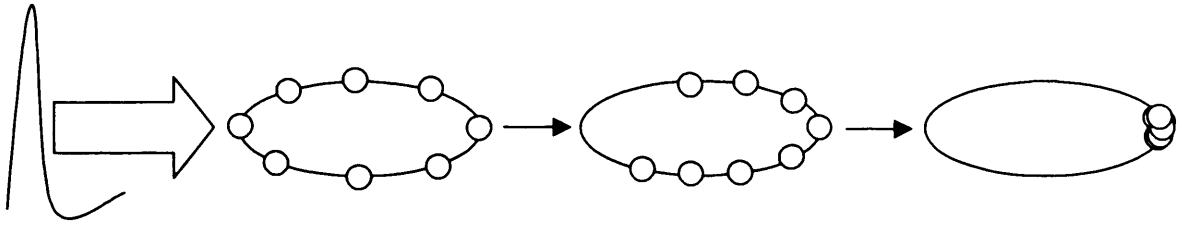
Figure 1.6. Schematic representation of the methodology of producing a three dimensionally localised electron wave packet. An initial state localised in the angular coordinate is prepared. This is then exposed to a HCP polarised along the direction of the orbit. Different components within the wave packet will be given different amounts of momentum from the HCP causing the wave packet to localise in the radial coordinate as well.

In the experiment of Bromage and Stroud, an initial state localised on an elliptical orbit of maximum eccentricity was excited. This was achieved by first applying a DC electric field across a pair of capacitor plates; to lift the ℓ degeneracy of an n manifold causing the angular momentum states to split up. The electric field will cause some states to rise in energy, and some to lower in energy. The highest energy state is called the blue state while the lowest energy state is called the red state. The blue and red states are localised on orbits of maximum eccentricity i.e. a line, in opposite directions, the $+z$ and $-z$ directions respectively. By selectively exciting the red state, then illuminating with an HCP polarised along the $-z$ direction, the population is redistributed to the red states of neighbouring n manifolds. This creates a wave packet localised in the radial coordinate moving on an elliptical orbit of maximum eccentricity.

1.3.3. Isolated core excitation.

In two electron systems, excitation of a Rydberg wave packet can leave an optically active core electron. Because excitation with an optical field is only possible at the core region, when the Rydberg wave packet is at the outer turning point the optically active

20

electron is now a core electron. Excitation of the inner electron can produce some exotic and interesting new wave packets as well as opening new avenues of control. Isolated core excitation (ICE) has been used to create non-dispersing wave packets in Ca [88,89], as a method of detecting the radial distribution of a Rydberg wave packet [90], to study the two electron dynamics in Ba [91] and as a logical control tool to push a Rydberg electron wave packet into a particular decay channel [4,92].

The work concerning two electron dynamics involved the excitation of two Rydberg wave packets. By controlling the energy difference and time delay between them, it was possible to control the radial position and kinetic energy of the first collision between the two electrons. As any interaction between the two electrons changes the ensuing motion, only the first collision could be controlled in this way. If this collision occurred near the nucleus, the large kinetic energies of the two electrons allowed large energy transfers between them. Conversely, if the interaction happened near the outer turning point, the electrons were essentially stationary and very little energy transfer could take place. For ionisation to occur, a certain amount of energy transfer between the electrons is required, and there is therefore a critical distance from the nucleus below which ionisation becomes possible and above which insufficient energy is transferred to ionise the Ba atom. By changing the energy difference between the two electron wave packets, the critical radius can be changed. Oscillations were seen in the ionisation signal as the time delay/collision distance between the two wave packets was changed. The oscillations proved that ionisation occurred as a consequence of a high-energy collision between the two electrons and not as a gradual energy transfer. The ionisation process in these high energy states can therefore be described by classical mechanics and are reasonably modelled by a classical Monte Carlo simulation.

1.4. Molecular Rydberg wave packets

The first observation of a molecular Rydberg electron wave packet came some 10 years after the initial atomic experiments [93,94]. In 1999 Fielding and coworkers presented work on Rydberg electron wave packets in NO [95-97], and the work showed some startling differences from the previous atomic work. At a first glance the recurrence spectra look similar to their atomic counterparts with clear recurrences, and the observation of full and partial revivals. On closer inspection, deviations in the position of the recurrences from those expected, were observed at specific energies. The deviations manifest themselves as plateaus in plots of the recurrence time against average principal quantum number, at times called the stroboscopic period. The first explanation put forward was a break down of the Born-Oppenheimer approximation, as the deviations only appeared when the motion of the Rydberg electron came into resonance with the classical rotational motion of the ionic core. This simplistic explanation however did not explain the observations quantitatively. A semiclassical model put forward by Altunata, Cao and Field [98], used a sum over classical trajectories approach to the problem in order to include some phase effects. For this semi-classical approach to be reasonable, extremely high rotational quantum numbers were used, and therefore allowed the use of average classical periods for the rotational motion. Although this method produced similar deviations to the experimental work of the Fielding group, these semi-classical arguments could not be used for the low rotational quantum numbers of the experiment. Subsequent work by Smith *et al* [99,100], rationalising the effects in terms of the line positions and phase evolution of the various components within the wave packet, gave the most satisfying explanation. The wave packets excited in the experiments of the Fielding group contain two Rydberg

series with different orbital angular momentum belonging to different rotational states of the ionic core. Both time and frequency domain pictures can be used to explain the deviations from atomic cases: in the frequency domain the wave packet contains states belonging to a lower series a and an upper series b, the states in each series will overlap when,

$$
\begin{aligned}
\Delta E_{rot} &= \frac{1}{2n_b^2} - \frac{1}{2n_a^2} = \frac{(n_a + n_b)(n_a - n_b)}{2n_a^2 n_b^2} \\
&\approx \frac{(n_a - n_b)}{n_s^3}
\end{aligned}
$$

(1.18)

where ΔE_{rot} is the rotational energy spacing between series a and series b, n_x is the principal quantum number in series x and $n_s = \sqrt{n_a n_b} \approx (n_a + n_b)/2$ is the stroboscopic effective principle quantum number. The approximation is valid for $2n_a^2 \Delta E_{rot} \ll 1$. Including the quantum defect in equation 1.18 and noting $n_a - n_b = k$, where k is an integer,

$$
\Delta E_{rot} = \frac{(n_a - \mu_a) - (n_b - \mu_b)}{n_s^3} = \frac{k + \Delta\mu}{n_s^3},
$$

(1.19)

where $\Delta\mu = \mu_b - \mu_a$. Equation 1.19 can now be rearranged to give the stroboscopic period, $T_s = 2\pi n_s^3$, in terms of the rotational energy spacing and quantum defects,

$$
T_s = T_{rot}(k + \Delta\mu)
$$

(1.20)

where $T_{rot} = 2\pi/\Delta E_{rot}$ is the rotational beat period. Equation 1.20 was the main result of the work carried out by Smith *et al.* The fundamental motions of molecular Rydberg wave packets are now almost as well understood as their atomic counterparts, allowing for the extension of atomic intuitive coherent control schemes to more complex molecular systems. The work presented in this thesis extends the study of molecular Rydberg systems from observation to control. With knowledge of how the various components contained within the wave packets behave, it is possible to control the composition of the wave packet, and also which bond within the molecule is broken.

In chapter two the experimental tools and techniques used in our experiments are introduced. Special emphasis is placed on the Michaelson interferometers and the phase control of the pulse trains used in the coherent control experiments. In chapter 3 the experiment to control the rotational angular momentum of a Rydberg electron wave packet is described. The control is then explained in terms of the phase evolution of the two series contained within the wave packet. In Chapter 4 experimental observations of a dissociating Rydberg electron wave packet are presented. The results are then compared with the results of earlier autoionising experiments carried out within the group. With knowledge of how the wave packet behaves in these two decay channels, the ionisation:dissociation ratio can be manipulated, and these results are also presented in chapter 4. A comprehensive MQDT representation of the NO molecule is then presented in chapter 5. An electronic reaction matrix of 46 parameters is derived using a non-linear least squares fit, and is used to calculate the full vibronic matrix and energy levels of the NO molecule. Finally chapter 6 provides some concluding remarks and suggests possible extensions to these experiments to further elucidate the control mechanisms of more complex pulse shapes.

1.5 References

1   J. Ahn, T. C. Weinacht, and P. H. Bucksbaum, Science **287** (5452), 463 (2000).

2   M. W. Noel and C. R. Stroud, Phys. Rev. Lett. **75** (7), 1252 (1995).

3   M. W. Noel and C. R. Stroud, Phys. Rev. Lett. **77** (10), 1913 (1996).

4   R. van Leeuwen, K. Vijayalakshmi, and R. R. Jones, Phys. Rev. A **6303** (3), 033403 (2001).

5   J. R. R. Verlet, V. G. Stavros, R. S. Minns, and H. H. Fielding, Phys. Rev. Lett. **89** (26), 263004 (2002).

6   T. C. Weinacht, J. Ahn, and P. H. Bucksbaum, Nature **397** (6716), 233 (1999).

7   T. C. Weinacht, J. Ahn, and P. H. Bucksbaum, Phys. Rev. Lett. **80** (25), 5508 (1998).

8   T. C. Weinacht, J. Ahn, and P. H. Bucksbaum, Phys. Rev. Lett. **81** (14), 3050 (1998).

9   J. L. Herek, W. Wohlleben, R. J. Cogdell, D. Zeidler, and M. Motzkus, Nature **417** (6888), 533 (2002).

10   P. Brumer and M. Shapiro, Chem. Phys. Lett. **126** (6), 541 (1986).

11   M. Shapiro and P. Brumer, J. Chem. Phys. **84** (7), 4103 (1986).

12   K. Bergmann, H. Theuer, and B. W. Shore, Rev. Mod. Phys. **70** (3), 1003 (1998).

13   X. B. Wang, R. Bersohn, K. Takahashi, M. Kawasaki, and H. L. Kim, J. Chem. Phys. **105** (8), 2992 (1996).

14   C. Chen and D. S. Elliott, Phys. Rev. Lett. **65** (14), 1737 (1990).

15   C. Chen, Y. Y. Yin, and D. S. Elliott, Phys. Rev. Lett. **64** (5), 507 (1990).

16   J. A. Fiss, L. C. Zhu, K. Suto, G. Z. He, and R. J. Gordon, Chem. Phys. **233** (2-3), 335 (1998).

17   L. Zhu, K. Suto, J. A. Fiss, R. Wada, T. Seideman, and R. J. Gordon, Phys. Rev. Lett. **79** (21), 4108 (1997).

18   V. D. Kleiman, L. C. Zhu, J. Allen, and R. J. Gordon, J. Chem. Phys. **103** (24), 10800 (1995).

19   L. C. Zhu, V. Kleiman, X. N. Li, S. P. Lu, K. Trentelman, and R. J. Gordon, Science **270** (5233), 77 (1995).

20   R. J. Gordon, L. C. Zhu, and T. Seideman, J. Phys. Chem. A **105** (18), 4387 (2001).

21   J. A. Fiss, A. Khachatrian, L. C. Zhu, R. J. Gordon, and T. Seideman, Faraday Discuss. (113), 61 (1999).

22   J. A. Fiss, L. C. Zhu, R. J. Gordon, and T. Seideman, Phys. Rev. Lett. **82** (1), 65 (1999).

23   J. Martin, B. W. Shore, and K. Bergmann, Phys. Rev. A **54** (2), 1556 (1996).

24   R. B. Vrijen, D. I. Duncan, and L. D. Noordam, Phys. Rev. A **56** (3), 2205 (1997).

25   U. Gaubatz, P. Rudecki, M. Becker, S. Schiemann, M. Kulz, and K. Bergmann, Chem. Phys. Lett. **149** (5-6), 463 (1988).

26   U. Gaubatz, P. Rudecki, S. Schiemann, and K. Bergmann, J. Chem. Phys. **92** (9), 5363 (1990).

27   R. Sussmann, R. Neuhauser, and H. J. Neusser, J. Chem. Phys. **100** (7), 4784 (1994).

28   R. Sussmann, R. Neuhauser, and H. J. Neusser, J. Chem. Phys. **103** (9), 3315 (1995).

29   B. K. Clark, J. M. Standard, and T. S. Boostrom, Opt. Commun. **164** (1-3), 145 (1999).

30   M. Keil, T. Kolling, K. Bergmann, and W. Meyer, Eur. Phys. J. D **7** (1), 55 (1999).

31   D. J. Tannor and S. A. Rice, J. Chem. Phys. **83** (10), 5013 (1985).

32   D. J. Tannor, R. Kosloff, and S. A. Rice, J. Chem. Phys. **85** (10), 5805 (1986).

33   D. J. Tannor and S. A. Rice, Adv. Chem. Phys. **70**, 441 (1988).

34   T. Baumert, B. Buhler, R. Thalweiser, and G. Gerber, Phys. Rev. Lett. **64** (7), 733 (1990).

35   T. Baumert, M. Grosser, R. Thalweiser, and G. Gerber, Phys. Rev. Lett. **67** (27), 3753 (1991).

36   T. Baumert, B. Buhler, M. Grosser, R. Thalweiser, V. Weiss, E. Wiedenmann, and G. Gerber, J. Phys. Chem. **95** (21), 8103 (1991).

37   R. S. Judson and H. Rabitz, Phys. Rev. Lett. **68** (10), 1500 (1992).

38   T. Brixner and G. Gerber, ChemPhysChem **4** (5), 418 (2003).

39   N. H. Damrauer, C. Dietl, G. Krampert, S. H. Lee, K. H. Jung, and G. Gerber, Eur. Phys. J. D **20** (1), 71 (2002).

40   T. Brixner, N. H. Damrauer, P. Niklaus, and G. Gerber, Nature **414** (6859), 57 (2001).

41   M. Bergt, T. Brixner, B. Kiefer, M. Strehle, and G. Gerber, J. Phys. Chem. A **103** (49), 10381 (1999).

42   C. Daniel, J. Full, L. Gonzalez, C. Lupulescu, J. Manz, A. Merli, S. Vajda, and L. Woste, Science **299** (5606), 536 (2003).

43   R. J. Levis and H. A. Rabitz, J. Phys. Chem. A **106** (27), 6427 (2002).

44   C. Daniel, J. Full, L. Gonzalez, C. Kaposta, M. Krenz, C. Lupulescu, J. Manz, S. Minemoto, M. Oppel, P. Rosendo-Francisco, S. Vajda, and L. Woste, Chem. Phys. **267** (1-3), 247 (2001).

45   R. J. Levis, G. M. Menkir, and H. Rabitz, Science **292** (5517), 709 (2001).

46   A. Assion, T. Baumert, M. Bergt, T. Brixner, B. Kiefer, V. Seyfried, M. Strehle, and G. Gerber, Science **282** (5390), 919 (1998).

47   R. A. Bartels, T. C. Weinacht, S. R. Leone, H. C. Kapteyn, and M. M. Murnane, Phys. Rev. Lett. **8803** (3), 033001 (2002).

48   J. B. Ballard, H. U. Stauffer, Z. Amitay, and S. R. Leone, J. Chem. Phys. **116** (4), 1350 (2002).

49   T. F. Gallagher, *Rydberg Atoms*. (Cambridge, 1994).

50   M. J. Seaton, Rep. Prog. Phys. **46** (2), 167 (1983).

51   M. J. Seaton, Mon. Not. R. Astron. Soc. **118**, 504 (1958).

52   C. H. Greene and C. Jungen, Advances in Atomic and Molecular Physics **21**, 51 (1985).

53   C. Jungen, *Molecular applications of quantum defect theory*. (Institute of Physics, 1996).

54   M. Hiyama and M. S. Child, J. Phys. B-At. Mol. Opt. Phys. **35** (5), 1337 (2002).

55   C. Jungen, S. T. Pratt, and S. C. Ross, J. Phys. Chem. **99** (6), 1700 (1995).

56   M. Hiyama and M. S. Child, J. Phys. B-At. Mol. Opt. Phys. **36** (22), 4547 (2003).

57   A. Matzkin, C. Jungen, and S. C. Ross, Phys. Rev. A **6206** (6), 062511 (2000).

58   C. Jungen and S. C. Ross, Phys. Rev. A **55** (4), R2503 (1997).

59   F. Texier, C. Jungen, and S. C. Ross, Faraday Discuss. (115), 71 (2000).

60   J. Parker and C. R. Stroud, J. Opt. Soc. Am. A-Opt. Image Sci. Vis. **2** (13), P93 (1985).

61   J. Parker and C. R. Stroud, Phys. Rev. Lett. **56** (7), 716 (1986).

62   J. Parker and C. R. Stroud, Phys. Scr. **T12**, 70 (1986).

63   J. A. Yeazell, M. Mallalieu, J. Parker, and C. R. Stroud, Phys. Rev. A **40** (9), 5040 (1989).

64   B. Broers, J. F. Christian, J. H. Hoogenraad, W. J. Vanderzande, H. B. Vanlindenvandenheuvell, and L. D. Noordam, Phys. Rev. Lett. **71** (3), 344 (1993).

65   B. Broers, J. F. Christian, and H. B. V. Vandenheuvell, Phys. Rev. A **49** (4), 2498 (1994).

66   G. Alber, H. Ritsch, and P. Zoller, Phys. Rev. A **34** (2), 1058 (1986).

67   G. Alber and P. Zoller, Phys. Rep.-Rev. Sec. Phys. Lett. **199** (5), 232 (1991).

68   J. F. Christian, B. Broers, J. H. Hoogenraad, W. J. Vanderzande, and L. D. Noordam, Opt. Commun. **103** (1-2), 79 (1993).

69   J. F. Christian and B. Broers, Phys. Rev. A **52** (5), 3655 (1995).

70   J. R. R. Verlet, V. G. Stavros, R. S. Minns, and H. H. Fielding, J. Phys. B-At. Mol. Opt. Phys. **36** (17), 3683 (2003).

71   J. Wals, H. H. Fielding, and H. B. V. Vandenheuvell, Phys. Scr. **T58**, 62 (1995).

72   I. S. Averbukh and N. F. Perelman, Phys. Lett. A **139** (9), 449 (1989).

73   J. Wals, University of Amsterdam FOM-AMOLF, 1996.

74   L. D. Noordam, D. I. Duncan, and T. F. Gallagher, Phys. Rev. A **45** (7), 4734 (1992).

75   E. D. Boleat and H. H. Fielding, Molec. Phys., In Press (2004).

76   C. Z. Bisgaard, M. D. Poulsen, E. Peronne, S. S. Viftrup, and H. Stapelfeldt, Phys. Rev. Lett. **92** (17), 173004 (2004).

77   J. Degert, C. Meier, B. Chatel, and B. Girard, Phys. Rev. A **67** (4), 041402 (2003).

78   N. F. Scherer, R. J. Carlson, A. Matro, M. Du, A. J. Ruggiero, V. Romerorochin, J. A. Cina, G. R. Fleming, and S. A. Rice, J. Chem. Phys. **95** (3), 1487 (1991).

79   N. F. Scherer, A. J. Ruggiero, M. Du, and G. R. Fleming, J. Chem. Phys. **93** (1), 856 (1990).

80   C. Petersen, E. Peronne, J. Thorgersen, and H. Stapelfeldt, Phys. Rev. A **70**, 033404 (2004).

81   R. R. Jones, Phys. Rev. Lett. **76** (21), 3927 (1996).

82   J. G. Zeibel, University of Virginia, 1997.

83   J. Bromage and C. R. Stroud, Phys. Rev. Lett. **83** (24), 4963 (1999).

84   Z. D. Gaeta, M. W. Noel, and C. R. Stroud, Phys. Rev. Lett. **73** (5), 636 (1994).

85   T. J. Bensky, M. B. Campbell, and R. R. Jones, Phys. Rev. Lett. **81** (15), 3112 (1998).

86   R. R. Jones and M. B. Campbell, Phys. Rev. A **6001** (1), 013403 (2000).

87   M. B. Campbell, T. J. Bensky, and R. R. Jones, Phys. Rev. A **58** (1), 514 (1998).

88   X. Chen and J. A. Yeazell, Phys. Rev. Lett. **81** (26), 5772 (1998).

89   L. G. Hanson and P. Lambropoulos, Phys. Rev. Lett. **74** (25), 5009 (1995).

90   R. R. Jones, Phys. Rev. A **57** (1), 446 (1998).

91   S. N. Pisharody and R. R. Jones, Science **303** (5659), 813 (2004).

92   R. van Leeuwen, M. L. Bajema, and R. R. Jones, Phys. Rev. Lett. **82** (14), 2852 (1999).

93   J. A. Yeazell and C. R. Stroud, Phys. Rev. Lett. **60** (15), 1494 (1988).

94   A. Tenwolde, L. D. Noordam, A. Lagendijk, and H. B. V. Vandenheuvell, Phys. Rev. Lett. **61** (18), 2099 (1988).

95   V. G. Stavros, J. A. Ramswell, R. A. L. Smith, J. R. R. Verlet, J. Lei, and H. H. Fielding, Phys. Rev. Lett. **83** (13), 2552 (1999).

96   V. G. Stavros, J. A. Ramswell, R. A. L. Smith, J. R. R. Verlet, J. Lei, and H. H. Fielding, Phys. Rev. Lett. **84** (8), 1847 (2000).

97   R. A. L. Smith, J. R. R. Verlet, E. D. Boleat, V. G. Stavros, and H. H. Fielding, Faraday Discuss. (115), 63 (2000).

98   S. N. Altunata, J. Cao, and R. W. Field, Phys. Rev. A **65** (5), 053415 (2002).

99   R. A. L. Smith, V. G. Stavros, J. R. R. Verlet, H. H. Fielding, D. Townsend, and T. P. Softley, J. Chem. Phys. **119** (6), 3085 (2003).

100   R. A. L. Smith, J. R. R. Verlet, and H. H. Fielding, Phys. Chem. Chem. Phys. **5** (17), 3567 (2003).

Chapter 2. Experiment for the production, detection and control of Rydberg electron wave packets.

2.1. Detection of Rydberg electron wave packets.

Creation of a wave packet requires short laser pulses, to detect the motion of the wave packet we require a technique that is not only time sensitive but also only detects the wave packet at a certain position on its orbit. The early experiments on Rydberg electron wave packets used a pump probe detection technique [1,2], which utilised the fact the wave packet would only adsorb the extra photon needed to ionise the system when it was at the core region. This technique gave very low signal levels due to the low ionisation probabilities of Rydberg states. The detection technique used in all the time resolved experiments presented in this thesis is the optical Ramsey method (ORM) [3], which provided a marked improvement in the signal to noise ratio of experiments in Rydberg electron wave packets, when compared with the pump probe experiments. The ORM uses two light pulses, generated in a stabilised interferometer, to monitor the return of an electron wave packet to the core, and is an extension to electronic wave packets of the ideas first used to measure vibrational wave packets [4-6]. The first light pulse creates a wave

32

packet in the weak field limit, i.e. the ground state population is not depleted by the interaction with the light pulse. The second light pulse then excites a reference wave packet, identical to the first, which acts as a probe to detect how much of the first wave packet has returned to its original state, i.e. its autocorrelation $\langle \Psi(t) | \Psi(0) \rangle$, where $\Psi(t)$ is the wavefunction of the initial wave packet which has evolved for a time t, and $\Psi(0)$ is the wavefunction of the reference wave packet which has just been launched. If the initial wave packet is launched, allowed to evolve, and then return to the core when the second wave packet is launched, the relative phases of the two wave packets becomes important. The second wave packet can be launched in phase with the initial wave packet, so that the population amplitude of the Rydberg states will be doubled. The total population is the square of the population amplitude which is therefore $4A^2$, where A is the population amplitude of a single wave packet. If the second wave packet is launched out of phase with the first, destructive interference will bring all the population back down to the launch state, leaving a total population of zero. If the second wave packet is launched when the first wave packet is away from the core, there is no interference and the total population is the incoherent sum of the two wave packets, $2A^2$. As the Rydberg population directly maps onto the various decay processes under investigation, the fringes can be seen in the ion signal collected. By scanning the phase of the second pulse, it is possible to differentiate when the wave packet is at the core, and when it is not. The oscillations can also be understood in the frequency domain. Fourier transforming a pulse pair separated by the recurrence time leads to a gaussian distribution of peaks, the spacing of the peaks in the frequency domain being the same as the spacing of the Rydberg states. Changing the phase of the second pulse shifts the position of the peaks in the gaussian, so by scanning the phase

of the second pulse the peaks will move from being over the Rydberg states leading to excitation, to being between the states where no population can be transferred.

2.2. Optical bench arrangement.

2.2.1. Time spectra

In figure 2.1, a schematic diagram of the laser layout used in the time-resolved experiments is presented. All the time-resolved experiments described in this thesis, involve a two-step excitation to access superpositions of Rydberg states. The first step, involves excitation of a launch state with well-defined quantum numbers, from which the wave packet is excited. This allows some control over the wave packet composition. A 20 Hz Q-switched Nd:YAG laser (Continuum Powerlite 8020), produces 8 ns long pulses of light at 1064 nm, this light is doubled to generate 532 nm light with energies of approximately 500 mJ/pulse. 40% of the second harmonic (200 mJ/pulse) is used to pump a tuneable dye laser (Continuum ND-6000) operating with a suitable dye. For the work described in this thesis the dye laser produces pulses of 8 ns duration with an average power of 10 − 15 mJ/pulse and a bandwidth of approximately 0.01 cm^{-1}. Using a series of non-linear crystals, potassium di-phosphate (KDP) and beta-barium borate (BBO), and appropriate optics, it is possible to produce pulses in the UV region around 210–230 nm, equivalent to the frequency tripled output of the dye laser fundamental. These pulses are used to excite the well-defined launch state from which a Rydberg electron wave packet is subsequently excited. From the launch

state, a broad bandwidth picosecond pulse coherently excites a number of Rydberg states.

A modelocked picosecond Nd:YAG laser (Coherent Antares) operating at 76 MHz

Coherent Antares

Continuum
Powerlite 8020

Coherent 701
dye laser

Continuum
ND-6000

300 mJ

30 mJ

1 mm Bethune
cell

200 mJ

100 mJ

4 mm Bethune
cell

170 mJ

8 mm Bethune
cell

15 mJ

KDP

300 µJ

½ wave plate

KDP

BBO

30 µJ

Interferometer
set-up

To vacuum
chamber
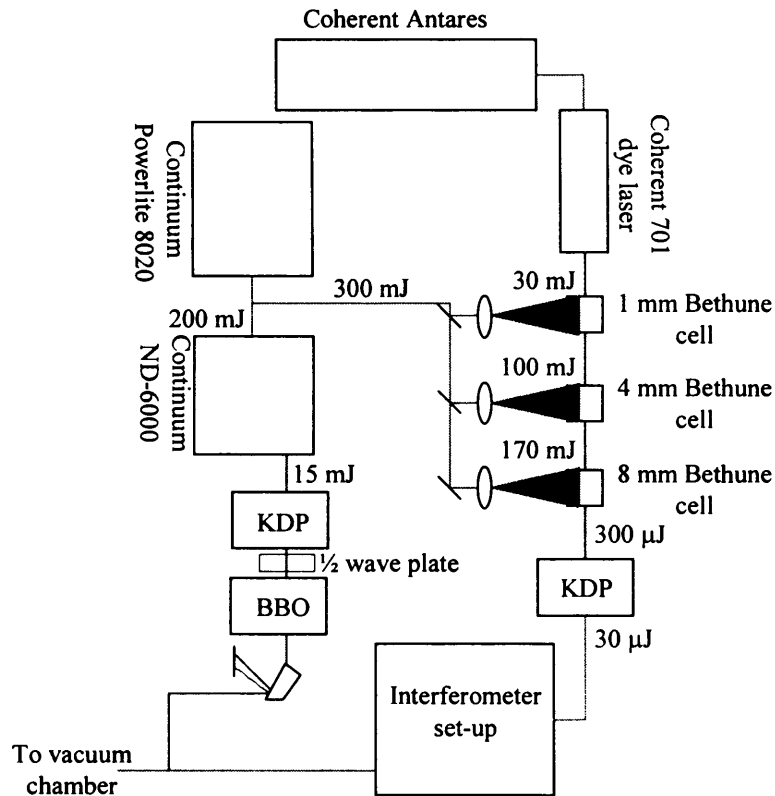
Figure 2.1 Schematic diagram of the optical bench layout used for the wave packet experiments in the

autoionising states of NO. A nanosecond Nd:YAG laser is used to pump a nanosecond dye laser

and amplifier cells for the picosecond pulses. The picosecond pulses are produced by pumping a

picosecond dye laser with a picosecond Nd:YAG. The light from both dye lasers pass through

non-linear crystals to obtain the appropriate wavelengths. The typical pulse energies for light

pulses at 20 Hz are indicated.

generates pulses of 50 ps duration at a fundamental wavelength of 1064 nm. The

fundamental light is then frequency doubled to give light at 532 nm with a power of

approximately 2 W. The 532 nm light is used to pump a picosecond dye laser (Coherent

701), operating with a suitable dye. The dye laser produces light of approximately 250 mW in power, with a pulse duration of either 1 or 3 ps, depending on the choice of birefringent filter used as the wavelength tuning element. A Coherent FR-103 autocorrelator is used to measure the autocorrelation of the picosecond light, by assuming the pulse shape is Gaussian the pulse duration can then be calculated. The pulses are amplified at 20 Hz using a series of three Bethune cells [7] containing the same dye as the dye laser. The set of Bethune cells are pumped with 60% (300 mJ/pulse) of the power from the nanosecond Nd:YAG laser. Bethune cells are 45°, right-angled, fused silica triangular prisms, of 4 or 5 cm in length. A spherical tube, through which dye is pumped, is drilled off centre. The nanosecond pump beam is expanded to four times the dye tube diameter to give uniform pumping according to figure 2.2.
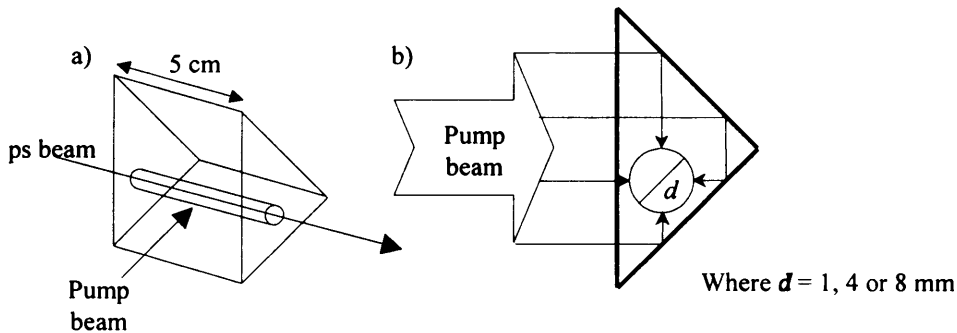
Figure 2.2. Schematic diagram a) and cross section b) of a Bethune cell showing the uniform excitation achieved when the pump beam is four time the dye tube diameter, d.

In our set-up we use a series of three cells of 1, 4 and 8 mm in diameter. The concentration of dye required in each cell is proportional to the reciprocal of the diameter. For example, the third cell is 8 mm in diameter, and has a dye concentration which is one eighth of that of the 1 mm cell. A stock solution of dye is made at a concentration of 50

mg/L, this is approximately that required by the 1 mm cell. Part of the stock solution is diluted to give the concentration required for the 4 mm and 8 mm cells, 12.5 mg/L and 6.25 mg/L respectively. From this starting point, more solvent or more concentrated dye solution can be added to achieve maximum amplification, while keeping amplified spontaneous emission (ASE) to a minimum (<15%). The addition of spatial filters between each amplification cell can also reduce ASE if required. The 1, 4 and 8 mm diameter Bethune cells are pumped with approximately 30, 100 and 170 mJ/pulse of the 532 nm radiation from the nanosecond Nd:YAG laser. The dye in the cells is refreshed at the rate of the pump laser; each laser shot therefore pumps fresh dye and avoids any heating effects. Between each cell, a telescope is used to magnify the beam to the diameter of the dye tube in the next cell. For example between the 1 mm and 4 mm cells a 1:4 telescope is used ($f =$ 25 mm and $f = 100$ mm in our arrangement). The amplification factors attainable for each cell are approximately 20,000, 200 and 20 times for the 1, 4 and 8 mm cells respectively. The larger diameter cells are used, despite their lower amplification factors due to the greater power attainable. For example, the maximum power attainable from the 1 mm cell is approximately 3 μJ/pulse, while the 8 mm cell has a maximum power of approximately 1 mJ/pulse. In practice when the alignment and dye concentrations have been optimised, the first cell amplifies from ~3 nJ/pulse to ~2 μJ/pulse; the 4 mm cell gives powers up to about 60 μJ/pulse and the 8 mm up to about 300 μJ/pulse. Once sufficient amplification has been achieved, the pulse can be frequency doubled at a suitable crystal (KDP). The doubling efficiency is in the region of 10%, yielding approximately 30 μJ/pulse of the frequency doubled light.

2.2.2. Michelson Interferometer.

The detection method employed in all the time resolved experiments, requires a pulse pair with a controllable time and phase separation. For this, a feedback stabilised Michelson interferometer is used (figure 2.3.). The incoming picosecond pulse is split into two at a 50% beam splitter (BS), one half is transmitted to a fixed mirror (FM), while the other half is reflected to a mirror mounted on a piezo electric actuator (Physik Instrumente P753.31C) which in turn is mounted on a motorised mechanical translation stage (Physik Instrumente P510.12). The light pulses are then reflected back to the beam splitter. The two pulses continue out of the interferometer with a controllable time and phase difference between them. The different path lengths travelled in the two arms of the interferometer, determine the time and phase difference between the two out going pulses.
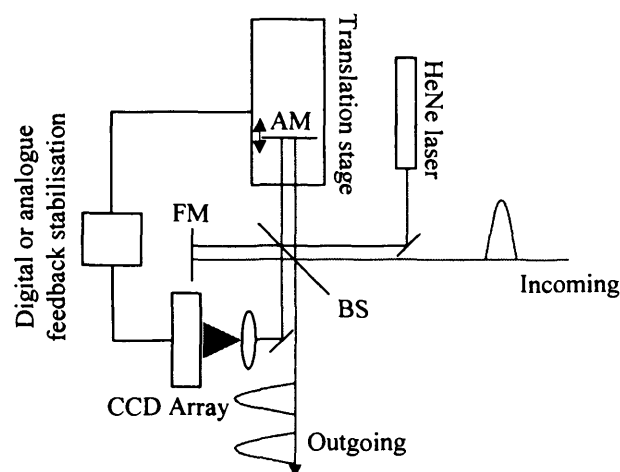
Figure 2.3. Schematic diagram of the interferometer showing the 50% beamsplitter (BS), the fixed mirror (FM) and the actuator mirror (AM) mounted on the translation stage. The incoming and outgoing pulses are shown schematically. The stabilisation circuit incorporating the CW HeNe laser and CCD array is also shown.

Low frequency vibrations slightly alter the path lengths travelled by the two pulses altering the phase relationship between them. The interferometer is therefore continuously stabilised to counteract these vibrations and maintain a constant phase relationship between the pulses. Active stabilisation is achieved using a continuous wave (CW) HeNe laser, a Charge Coupled Device (CCD) and a PID feedback circuit. The output of a CW HeNe laser (Carl Zeiss Jena LGK7628) is directed into the interferometer parallel to the picosecond light, following the same path and recombining at the beam splitter. The interference fringes generated by the HeNe light are expanded onto a CCD array (Basler L101-K). Typically 4-5 fringes are monitored over 1024 pixels and the light intensity on each pixel is converted to a voltage. External vibrations cause the fringe pattern to move, changing the voltage detected on each pixel. Stabilisation is achieved by first interrogating the interference pattern to find the point of largest gradient, because it is the most sensitive (as even small vibrations will cause large voltage changes). The PID control detects the voltage change caused by any vibrations, and feeds back to the piezo crystal a suitable voltage waveform to counteract the vibration [8]. PID stands for proportional, integral and differential, and the voltage feedback has the form,

$$V(t) = Pe(t) + I \int e(t)dt + D\frac{de(t)}{dt} \qquad (2.1)$$

where P, I and D are the proportional integral and differential constants respectively, and $e(t) = PV(t) - SP$ where SP is the set point voltage and PV(T) is the principal variable, in this case the actual voltage . These are set empirically to stabilise the vibrations in the lab.

When carrying out the experiments, the relative phase of the second pulse must be controllable down to about $\lambda/20$ (for 330 nm this is about 8 nm), where λ is the wavelength of light. In practice the feedback system stabilises vibrations down to approximately 4 nm allowing us extremely fine control over the relative phases of the pulses used.

For the coherent control experiments described in chapter 3, a series of three phase locked pulses with variable time delays between them are needed. This requires an extra piezo electric actuator mounted mirror on a translation stage, making a nested or double interferometer (figure 2.4). In the double interferometer both movable arms are feedback stabilised relative to the fixed arm. This is done in the same way as with the single interferometer, so for each arm there is a separate CW HeNe laser, CCD array and PID feedback circuit. Developed within the group, there are two stabilisation circuits; one older analogue system and one more recent digital system. The digital system is used to stabilise the single interferometer and to stabilise the detection pulse in the three pulse experiments. The analogue system is used to stabilise the control pulse in the three armed interferometer. This choice is made due to the superior long term stability of the analogue system when compared with the digital system. All three pulses emerging from the double interferometer must have similar powers. For this reason both beam splitters used are 50% reflecting and a 25% reflecting mirror is mounted in movable arm 2. This ensures that all pulses are $1/16^{th}$ the power of the incoming beam. The phase difference each piezo step induces, is calibrated against the ion signal fringes collected at $t = 0$. As the piezo is stepped, Ramsey fringes are seen in the ion signal. The distance between each peak in the interference pattern corresponds to an optical cycle, 2π, therefore if there are 10 piezo steps from peak

to peak, each piezo step correspond to a phase step of $\pi/5$. In practice a series of 10 - 15 fringes are collected and a sine wave can then be fitted to the fringes and an average number of steps can be taken. The step size can be controlled by changing the magnitude of the voltage applied to the piezo for each step. The typical step size used for the detection arm is approximately $\pi/5$, while for the control arm it is approximately $\pi/8$ and the step size is calibrated before each new experimental run. The reason the step size has to be calibrated is that the absolute phase difference at the start of a run cannot be measured; we therefore have to make sure we step over every possible phase difference between the pulses. Control of all the translation stages and piezos used in the experiment is via a PC running a labview program developed within the Fielding group [9].
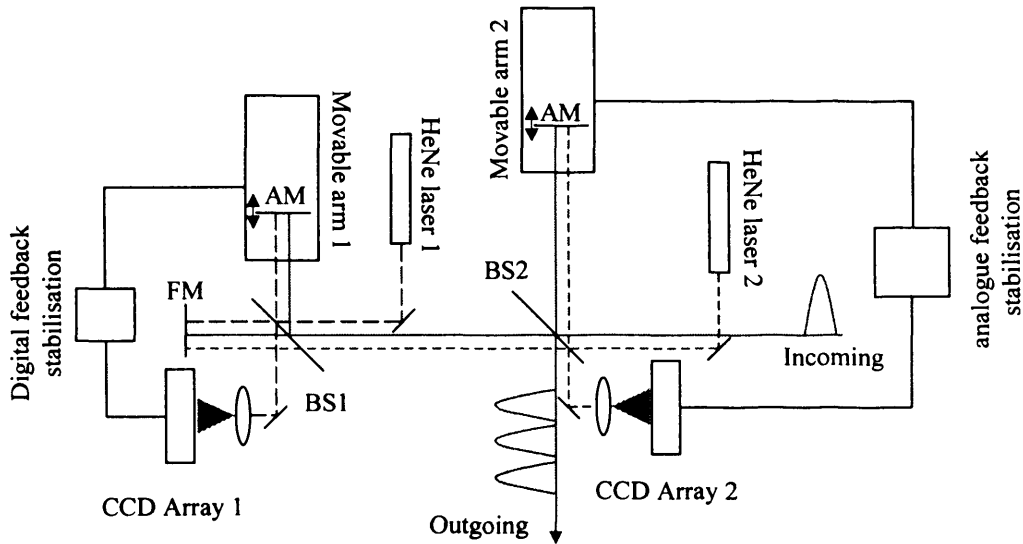

Figure 2.4. Schematic diagram of the double interferometer, showing the 50% beamsplitters (BS), the fixed mirror (FM) and the actuated mirrors (AM) mounted on the translation stages. The incoming and outgoing pulses are shown schematically.

2.2.3. Frequency spectra

Detailed knowledge of the composition of a wave packet is required before any predictions or coherent control experiments can be designed. For this reason, frequency resolved spectra are usually recorded when starting to design coherent control schemes. Figure 2.5. shows a schematic representation of the optical-table layout used for all the frequency resolved experiments. Like the time resolved experiments, a two step excitation process is employed. Typically, 40% (200 mJ/pulse) of the frequency doubled output from a 10 Hz Q-switched nanosecond Nd:YAG laser (Continuum Powerlite 8010), producing 6 ns pulses, pumps a nanosecond dye laser (Continuum ND-6000) containing a suitable dye. Pulses of around 13 mJ are produced with a bandwidth of approximately 0.01 cm^{-1}. Using a series of nonlinear crystals (KDP and BBO) and appropriate optics, it is possible to produce pulses in the UV range from 210-230 nm. The narrow bandwidth light is used to excite a specific intermediate state from which the Rydberg states can be accessed. The remaining 60% (300 mJ/pulse) of the output of the nanosecond Nd:YAG laser pumps a second nanosecond dye laser (Sirah Precisionscan). The output is frequency doubled in a KDP crystal, producing pulses with a typical energy of 2 mJ/pulse and a bandwidth of 0.001 cm^{-1}. The wavelength of the second pulse can then be scanned over a 3-4 nm range to cover principal quantum numbers from around $n = 20$ to the ionisation limit
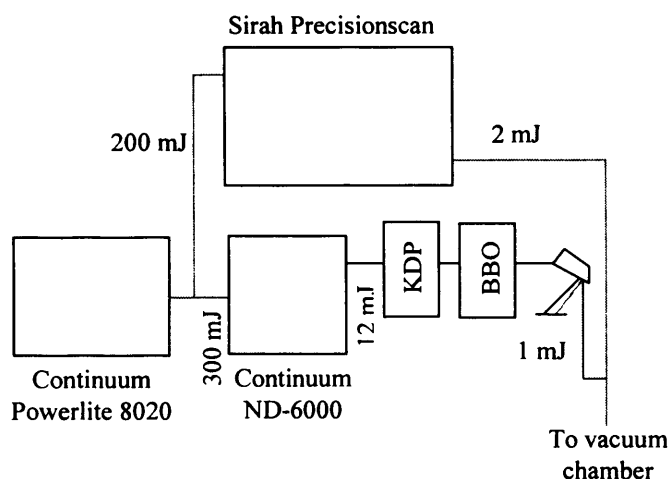
Figure 2.5 Schematic diagram of the optical layout used for the frequency resolved experiments in NO. A nanosecond Nd:YAG laser to pump two nanosecond dye lasers. The light from both dye lasers passes through non-linear crystals to obtain the appropriate wavelengths. All energies are given per pulse.

All frequency resolved spectra are calibrated using a wavemeter (Angstrom WS-7). Part of the Sirah beam is split from the main beam and directed into a fibre optic which couples the light into the wavemeter. As the Sirah wavelength is scanned, each wavemeter reading and its corresponding ion signal are recorded.

2.3. Vacuum chamber

The entire experiment is conducted inside a differentially pumped time of flight apparatus. The vacuum system comprises two chambers connected by a time of flight (TOF) tube. A schematic cross section of the vacuum chamber is presented in figure 2.6. The interaction chamber is held at a pressure of around 10^{-5} mbar by an oil diffusion pump (Edwards 160-

700) and NO gas is pulsed into the chamber at 20 Hz using a solenoid valve (general vales series 1250 ps1A). The position of the valve can be adjusted using a commercial XYZ translation stage mounted on top of the interaction chamber. The light pulses cross the gas jet at right angles between a pair of capacitor plates separated by 1.5 cm and surrounded by a mu-metal shield to stop any stray magnetic fields. Approximately 100 ns after the final light pulse crosses the gas jet, a high voltage is pulsed on to one capacitor plate providing a large electric field (2000 V/cm) with a rise time of approximately 20 ns. The electric field ionises the Rydberg states and accelerates the ions through the field free TOF tube. The zero field plate and the entrance and exit of the TOF tube are covered with an earthed wire mesh with a transmittance of 95%. The time of flight tube is 20 cm long, and spatially separates the various mass products produced in the experiments, e.g. N^+ and NO^+ produced in the predissociation experiment (chapter 4). The products are then detected at different times on a microchannel plate (MCP) (Hamamatsu F4655-12). The MCP is mounted in the detection chamber which is held at a pressure of 10^{-7} mbar by a turbomolecular pump (Edwards EXT250). Both the diffusion and turbomolecular pumps are held at a backing pressure of 10^{-3} mbar by a two stage rotary pump (Edwards 2-stage E2M18). The signal from the MCP is amplified by either one or two fast pre-amplifiers (Ortec EG&G VT120) and monitored on a digital oscilloscope (LeCroy 9350A). The pressure in the interaction chamber is approximately 10^{-5} mbar, this gives a gas density of 2.50×10^{12} molecules/cm^3 and an average spacing between molecules of 0.7 µm. for $n = 40$ (larger than any states used in the experiments described in this thesis) the Bohr radius is approximately 0.1 µm, interactions between neighbouring Rydberg states can therefore be neglected, but could become important at higher gas pressures.
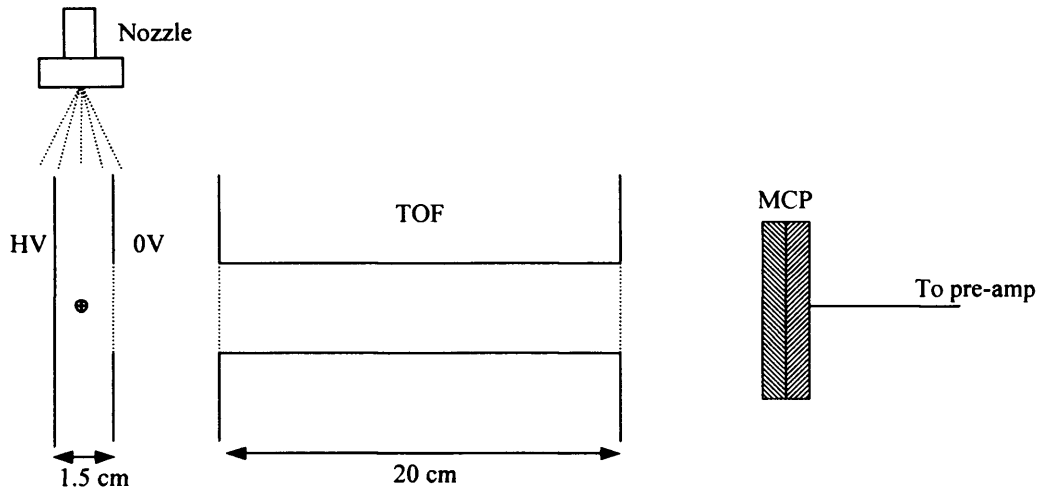
Figure 2.6. Schematic diagram of the inside of the vacuum chamber, showing all voltage plates, detection equipment and nozzle. The entrance to the TOF and the earthed voltage plate are covered with a wire mesh with a transmittance of 95%. The ⊕ shows the position the laser light crosses the gas jet going into the page.

2.4. Timing control

The amplification of the picosecond light requires the Bethune cells to be pumped by the nanosecond laser pulse at the same time as the picosecond pulse passes through it. As little as a 5 ns jitter between the two pulses can cause a complete loss of amplification. The nozzle is also pulsed, and thus needs to be synchronised to leave maximum pressure in the interaction region at the instant the light pulses arrive. To achieve this synchronisation the entire experiment is triggered externally by a pulse generator (Thandar), which controls the repetition rate of the entire experiment.

Thandor
pulse generator

Pulsed nozzle

20/10 Hz

5 ms
delay

Modelocker

DG535-1

38 MHz — LF   IF   RF

T_0

A   A⎍B C⎍D

A = T + 110 μs
B = A + 10 μs
C = A + 266.67 μs
D = C + 10 μs

mixer

DG535-2

A = T + 268.94 μs
C = T + 266.46 μs
D = C + 300.31 μs

T_0

A   C⎍D

Flash Q-switch
lamps

ns laser control unit

Oscilloscope   Electric field pulse
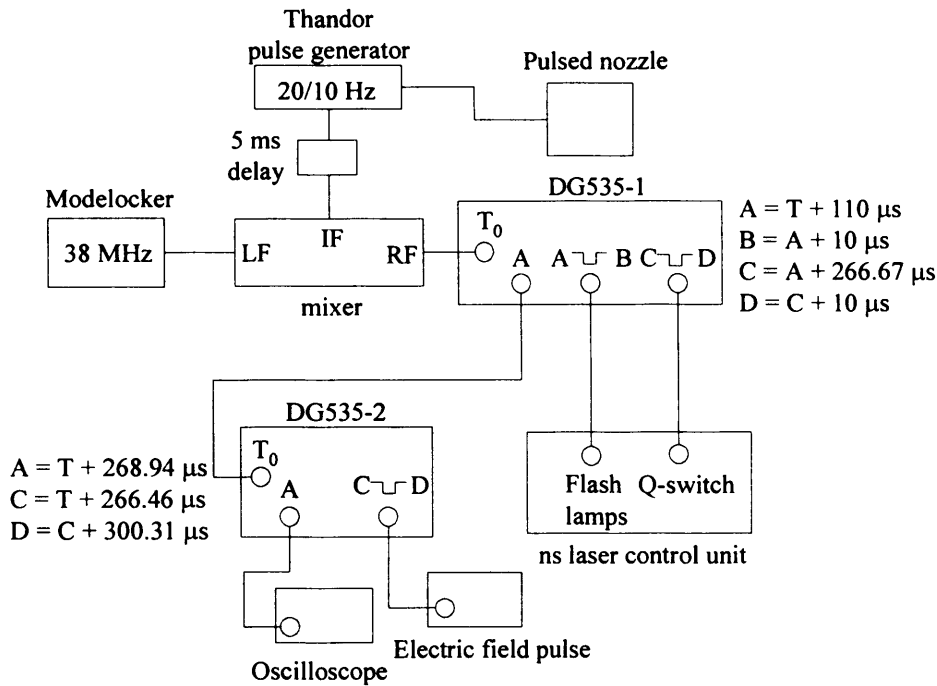
Figure 2.7. Block diagram showing various connections, timings and components used to control the relative timing of the equipment used in the experiments.

The Thandar pulse generator generates a TTL signal at 20 or 10 Hz, depending on the Nd:YAG laser used. Two outputs are taken; one goes directly to the nozzle controller, the other to a home built electronic delay generator with a coarse delay of about 5 ms, allowing the nozzle time to discharge and pressurise the chamber before the light pulses arrive. The delayed signal is combined at a double balanced mixer (Hatfield 1750) with the 38 MHz signal from the modelocker of the picosecond Nd:YAG laser. The signal from the mixer is now a 20 or 10 Hz signal locked to the output of the picosecond laser. This output from the mixer is then used to externally trigger a digital delay generator (Stanford Reasearch Systems DG535), which triggers the flash lamps and Q-switch of the nanosecond Nd:YAG laser, as well as providing a trigger for a second DG535 delay generator. The second DG535 is used to trigger the oscilloscope for data collection and the pulsed electric field.

46

Figure 2.7. shows a block diagram of all the relevant timing equipment and connections used in the experiment.

2.5. Experimental implementation of the Optical Ramsey method.
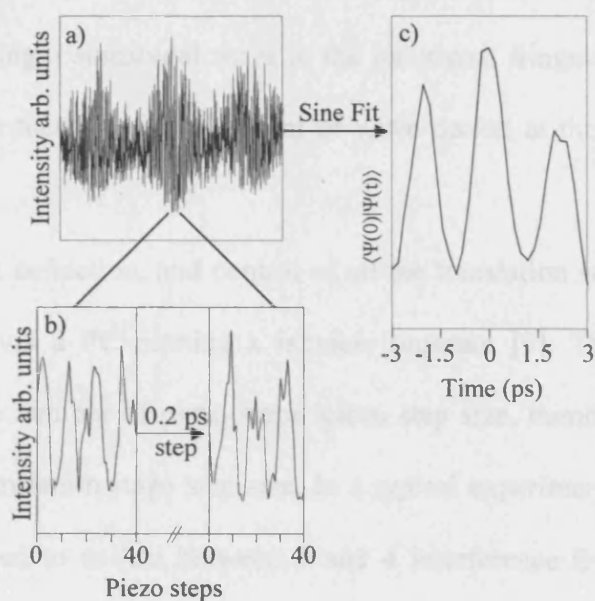
Figure.2.8. a) Raw data obtained for an ORM experiment on the autoionising states of NO. Fringes can be seen around 0 and ~2 ps with region of constant intensity at ~1 ps. b) An expanded region of the raw data at two coarse delays around t = 0 showing the interference fringes in the ion signal. At each coarse delay 40 piezo steps are taken to covers approximately 3-4 interference fringes. A sine wave can then be fitted to the raw data to filter out the optical frequency leaving us with a time spectrum c) where peaks represent a large electron density near the core.

For the ORM the phase difference between a pulse pair must be scanned. In order to do this experimentally the piezo positioner mounted in one arm of the interferometer is moved a few optical cycles in steps of fractions of the wavelength (typically $\lambda/10$). To cover an entire time spectrum of typical length 100 ps, scanning the phase all the way

would require a huge amount of raw data. A way around this is to scan the piezo over 3 or 4 interference fringes and then move a coarse delay of approximately 0.2 ps, and then collect another set of interference fringes at this position, and so on (figure 2.8.a) and b)). At each coarse delay we can tell how much of the wave packet is at the core, by the amplitude of the fringes at that position. The optical frequency can then be filtered out by least square fitting a sinusoidal wave to the ion signal fringes; the RMS amplitude of the sinusoidal wave then gives the amount of wave packet at the core for each coarse delay (figure 2.8.c)).

The data collection, and control of all the translation stages and piezos used in the experiment, is via a PC running a labview program [9]. The labview program allows control over the number of piezo steps, piezo step size, number of laser shots to average over and the translation stage step size. In a typical experiment, 40 piezo steps per coarse delay are scanned to collect between 3 and 4 interference fringes. Each coarse delay is approximately 0.2 picoseconds and each run lasts for about 100 ps, this leaves us with roughly 20,000 data points, each data point being the average of around 10 laser shots. Each spectrum can therefore take several hours to run, and requires all equipment to be extremely stable for long periods of time.

As mentioned above the detection method can only work in the weak field limit, so we must therefore consider the power of the picosecond pulses used in the experiments. After the interferometer, the typical power used for excitation of the Rydberg states is 5 μJ for a 3 ps pulse. The picosecond pulse is combined with the nanosecond pulses at a dichroic mirror. All beams are then focussed with a 300 mm lens with gives a diffraction limit beam waist for the picosecond pulses of approximately 12 μm, the length of the waist

region is then 7.6 µm which corresponds to twice the Rayleigh range. The diffraction limit intensity at the focus is therefore approximately 1.3×10^{12} W cm^{-2}, giving a peak electric field of $E_0 = 2.2 \times 10^9$ Vm^{-1}. For the weak field approximation to hold, the laser interaction time must be much smaller than the reciprocal of the Rabi coupling i.e. $t >> \Omega^{-1}$, where $\Omega = \mu E_0 / \hbar$ and μ is the transition dipole. For the transition from the A-state to the $21p$ Rydberg state in NO, $\mu = 1.5 \times 10^{-4}$ [10]. This gives a Rabi coupling of $\Omega = 2.7 \times 10^{10}$ rads^{-1}, the maximum interaction time is therefore $\Omega^{-1} = 38$ ps, which is much longer than the pulse duration. The weak field approximation therefore holds. The actual intensity is likely to be less than this, because reaching the diffraction limit is experimentally difficult. The actual beam waist is likely to be more than double that reported here, giving extra credibility to the weak field approximation.

2.6. Population calculations

The efficiency of a particular control scheme can be determined from the Rydberg state population distribution following a particular pulse sequence. Experimentally this can be achieved using state selective field ionisation (SSFI) [11], but in regions where this is not possible, e.g. autoionising states, they can be calculated using energies and intensities obtained from frequency resolved spectra. In order to calculate the population distribution of a wave packet following the interaction with a light pulse or sequence of light pulses, first consider the time dependent Schrödinger equation,

$$H\Psi = i\hbar\frac{d\Psi}{dt} \tag{2.3}$$

and the wavefunction of a two level atom,

$$\Psi(r,t) = a_g\Psi_g(r)e^{-i\omega_g t} + a_n\Psi_n(r)e^{-i\omega_n t} \tag{2.4}$$

where a is the population coefficient of the ground (g) or excited state (n), ω is the angular frequency of the state and Ψ is the wavefunction. When the atom interacts with a photon of angular frequency $\omega = \omega_n - \omega_g$ the total Hamiltonian can be described using perturbation theory as,

$$H = H_0 + H_1 = H_0 + eE(t)z \tag{2.5}$$

where H_0 is the atomic Hamiltonian and $eE(t)z$ is the perturbation due to the light field. Substituting equations 2.4 and 2.5 into equation 2.3 and evaluating the expression gives expressions for the derivatives of the population coefficients within the rotating wave approximation,

$$\dot{a}_n = -\frac{i}{2}\Omega_n a_g f(t)e^{i\Delta t} \tag{2.6}$$

where $\Omega_n = eE_0\langle n|z|g\rangle/\hbar$ is the Rabi frequency, $\Delta = \omega_n - \omega_g - \omega$ (where ω is the photon angular frequency) is the detuning and $f(t)$ is the envelope function of the laser pulse. Integrating equation 2.6 gives the amplitude in state n,

$$a_n = -\frac{i}{2}\Omega_n g(\omega) \qquad (2.7)$$

where $g(\omega)$ is the Fourier transform of $f(t)e^{i\Delta t}$. This can be extended to multiple pulses by making $f(t)$ in equation 2.6 a multipulse envelope function of the form,

$$f(t) = g(t) + \sum_i g(t - \tau_i)\exp(i\omega\tau_i) \qquad (2.8)$$

where the sum is over i pulses and τ_i is the delay between them. The probability amplitude in state n after i pulses is then,

$$a_n = -\frac{i}{2}\Omega_n g(\omega)\left[1 + \sum_i \exp(i(\omega_n - \omega_g - \omega)\tau_i)\right] \qquad (2.9)$$

This population expression is employed in all the coherent control schemes presented in this thesis as a means of determining the efficiency of the scheme.

2.7. Summary

In this chapter we have described the experimental tools and techniques available for the study of molecular Rydberg electron wave packets. The multiphoton excitation process used in all our experiments allows some control over the composition of the wave packet when compared with single photon excitation. This is particularly important in molecular systems where a high density of ro-vibrational level would otherwise be accessible.

The production of three phase locked pulses used in the production, detection and control of Rydberg wave packets has also been described. Particular emphasis has been placed on the phase stabilisation of the interferometer and the implementation of this in the coherent control experiments described in this thesis. Finally the origin of the population calculations used in subsequent chapters to determine the control efficiency of a particular scheme has been described.

2.8. References

1   J. A. Yeazell and C. R. Stroud, Physical Review Letters **60** (15), 1494 (1988).

2   A. Tenwolde, L. D. Noordam, A. Lagendijk, and H. B. V. Vandenheuvell, Physical Review Letters **61** (18), 2099 (1988).

3   L. D. Noordam, D. I. Duncan, and T. F. Gallagher, Physical Review A **45** (7), 4734 (1992).

4   N. F. Scherer, A. Matro, L. D. Ziegler, M. Du, R. J. Carlson, J. A. Cina, and G. R. Fleming, Journal of Chemical Physics **96** (6), 4180 (1992).

5   N. F. Scherer, R. J. Carlson, A. Matro, M. Du, A. J. Ruggiero, V. Romerorochin, J. A. Cina, G. R. Fleming, and S. A. Rice, Journal of Chemical Physics **95** (3), 1487 (1991).

6   N. F. Scherer, A. J. Ruggiero, M. Du, and G. R. Fleming, Journal of Chemical Physics **93** (1), 856 (1990).

7   D. S. Bethune, App. Opt. **20** (11), 1897 (1981).

8   Q. Hong, J. A. Ramswell, V. G. Stavros, C. J. Barnett, and H. H. Fielding, Measurement Science & Technology **9** (3), 378 (1998).

9   J. R. R. Verlet, Kings College London, 2003.

10   J. H. Geng, T. Kobayashi, and M. Takami, Chemical Physics Letters **291** (3-4), 277 (1998).

11   T. F. Gallagher, *Rydberg Atoms*. (Cambridge University Press, 1994).

Chapter 3: Controlling the rotational angular momentum composition of a molecular Rydberg wave packet.

3.1 General

Previous optical control experiments with Rydberg systems have concentrated on atomic problems [1-18], many of which rely on feedback loops combined with pulse shaping techniques [19] to find the optimal control pulse required. In these experiments, the control mechanism is often difficult, and sometimes impossible, to unravel from the complex pulse shapes produced. More relevant to this chapter are the logical control schemes used, for example, to control the orbital angular momentum of a Rydberg electron wave packet [11], or to manipulate the autionisation channel in a doubly excited atom [10]. In these logical control schemes, the control mechanism is input from the start and is therefore well understood. Although the level of control in the logical experiments is sometimes less than perfect, these experiments are extremely instructive and can give an insight into some of the more complex waveforms derived from feedback loops.

After atomic systems, the next obvious step is the study of diatomic molecules. By adding a core that can rotate and vibrate we can begin to build a picture of how control mechanisms in a more complex system work. NO is an ideal molecule for such studies

because excitation of the outer electron leaves a closed shell core, which greatly simplifies the angular momentum coupling. In addition the low ionisation potential of the molecule allows relatively easy access to the Rydberg states in a one or two photon process.

3.2. Spectroscopy.

3.2.1. Spectroscopy of NO

The relative simplicity of diatomic molecules has led to them being widely studied and characterised using spectroscopy. The NO molecule has been a particular favourite, due to its low ionisation potential and lone outer electron. Many groups have contributed to the study of NO with many experiments leading to extremely accurate and instructive measurements of ground and excited state spectroscopic constants [20-22]. Early work on the Rydberg states of NO by Miescher and co-workers [23-29], and subsequent work by others [30-38], has also given accurate measurements of ionisation limits and quantum defects. These studies have shown that however simple diatomic molecules may appear to be, many complications still appear in their Rydberg spectra. In NO the s and d states are known to be strongly mixed [36,39], as well as Rydberg state interactions with valence states producing large perturbations in their line positions [40], and also leading to dissociation [31-35,41,42] (see chapter 4).

The excitation of Rydberg wave packets in our experiment is achieved in a two-step process. The region of the spectrum we are interested in is extremely dense with many states accessible from the ground state. An intermediate electronic state is therefore

employed as selection and propensity rules from the intermediate limit the number of final states that are accessible. In order to discuss the excitation and control scheme described in this chapter, and in Chapter 4, it is necessary to understand the angular momentum coupling in all the states involved. Hund's cases are often used to describe the angular momentum coupling of diatomic systems. The ground state of NO, X $^2\Pi_J$, is usually described using a Hund's case (a) coupling scheme. The first excited state, A $^2\Sigma^+$, is described using Hund's case (b), and the Rydberg states are usually described using Hund's case (d). Cases (c) and (e) will not be discussed in this chapter as they do not accurately describe any of the states involved in these experiments.

In Hund's case (a), the total orbital angular momentum, L, and the total electron spin, S, couple to the internuclear axis and are no longer good quantum numbers themselves. The projections of L and S along the internuclear axis are Λ and Σ respectively. In turn, Λ and Σ couple to give $\Omega = \Lambda + \Sigma$, and Ω is the total angular momentum projection along the internuclear axis. The rotation of a diatomic, N, is perpendicular to the internuclear axis. N couples to Ω to give the total angular momentum, $J = N + \Omega$ (figure 3.1 i)).

In Hund's case (b), S is no longer coupled to the internuclear axis, although L remains coupled to the internuclear axis with projection Λ along the bond axis. N then couples to Λ to give N'. N' in turn couples to S to give $J = N' + S$ (figure 3.1 ii)).

In Hund's case (d), the orbital angular momentum of the Rydberg electron is denoted ℓ. The Rydberg electron spin, s, is uncoupled from the internuclear axis and remains a good quantum number. The Rydberg electron spends most of its time a long way from the core and so the core rotation can be treated independently of it. The rotation is

therefore that of an ion core and is perpendicular to the internuclear axis and is labeled N^+.

N^+ couples with ℓ to give $N' = N^+ + \ell$. N' then couples to s to give $J = N' + s$ (figure 3.1 iii)).
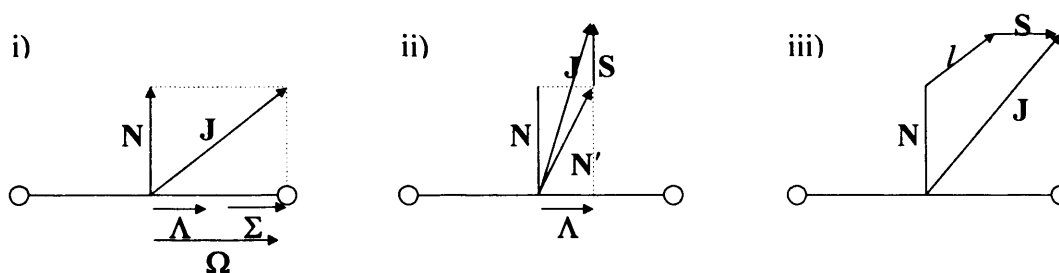
Figure.3.1. Schematic vector diagrams of Hund's coupling case a i), b ii) and d iii).

3.2.2 A-state Assignment

In the experiments described in this chapter, autoionising Rydberg states converging to the $v^+ = 1$ vibrational level of the molecular ion, are excited above the lowest vibrational level of the electronic ground state of the ion. The A-state is used as an intermediate; a frequency resolved spectrum of the A-state and assignment of the A-state spectrum is therefore required. In all subsequent equations X'' denotes ground state quantum numbers, X' denotes intermediate state quantum numbers and X^+ denotes the quantum numbers of the Rydberg states.

The ground state, $^2\Pi_{J''}$, consists of two spin-orbit states, $J'' = 1/2$, $3/2$, both of which are thermally populated due to the small energy splitting of approximately 120 cm^{-1}. The energy of the ground ro-vibrational levels can be calculated using [21],

$$E_{v,l} = G_v'' - D_v'' + \frac{a_v''}{2} + B_{vJ}'' (J'' + \frac{1}{2})^2 - D_{vJ}'' (J'' + \frac{1}{2})^4 . \tag{3.1}$$

Equation 3.1 calculates the energy levels for the two spin-orbit states and takes the energy zero as the mid point between them. a_v'' is the spacing between the two spin orbit states, D_v'' is the true rotational constant, B_{vJ}'' and D_{vJ}'' are the effective rotational constants of the particular spin orbit state, J is given the value 1 for F2 states and 2 for F1 states, where F2 and F1 label the lower and upper spin-orbit states respectively. G_v'' is the vibrational energy which can in turn be calculated from,

$$G_v'' = (v'' + \frac{1}{2})\omega_e'' - (v'' + \frac{1}{2})^2 \omega_e x_e'' + (v'' + \frac{1}{2})^3 \omega_e x_e'' - \dots \tag{3.2}$$

where ω_e'' is the harmonic vibrational wavenumber, $\omega_e x_e''$ and $\omega_e y_e''$ are the first and second order anharmonicity constants respectively.

The A-state energies can be calculated using,

$$E_{N,v} = T_e' + G_v' - D_v' N'^2 (N' + 1)^2 + B_v' N'(N' + 1) . \tag{3.3}$$

All the symbols have the same definitions as before. In order to calculate the transition energies, the ground state energy is subtracted from the A-state energy. The energy to the bottom of the A-state well from the bottom of the ground state well is given the symbol T_e. The P_{12} branch of the A-state has been chosen, because many rotational levels are easily accessible as no other branches cross this region. In this nomenclature P means the

transition has $\Delta J = -1$, while the subscripts mean the transition is from an initial F1 state ending up in an F2 state. The A-state spectrum is obtained in a 1+1 Resonance Enhanced Multiphoton Ionisation (REMPI) process; a single photon of around 215 nm is used to excite a specific quantum state $|v', N', J'\rangle$ of the A-state. A second photon of the same energy then ionizes the molecule forming NO^+. The spectral assignment is carried out using the above formulae and the molecular constants in reference [21] for the ground state and reference [20] for the A-state. These values are listed in table 3.1. A portion of a typical frequency spectrum is shown in figure 3.2. In all subsequent experiments described in this chapter the $|v' = 1, N' = 0, J' = 1/2\rangle$ level is used as the intermediate from which we launch the wavepacket.
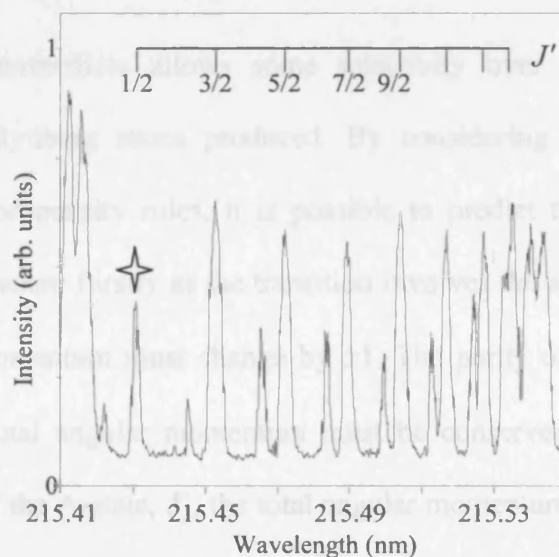
Figure.3.2. *REMPI spectrum of the P_{12} branch of the A-state. J' values are labeled with a comb. All subsequent frequency and time resolved experiments in this chapter are excited via the $|v' = 1, N' = 0, J' = 1/2\rangle$ which is labeled with a star.*

	$X^2\Pi_{3/2}$	$A^2\Sigma^+$
α	119.770	——
D_0	5.5×10^{-6}	——
B_{02}	1.72002	——
D_{02}	9.8×10^{-6}	——
B_1	——	1.9678
D_1	——	5.4×10^{-6}
ω_e	1903.68	2374.31
$\omega_e x_e$	13.97	16.106
$\omega_e y_e$	-0.0012	-0.0465

Table 3.1. Spectroscopic constants used in the assignment of the A state spectrum shown in figure 3.2. All values given are given in cm^{-1} and are taken from [21] and [20].

3.2.3 Rydberg state excitation

Excitation via an intermediate allows some selectivity over the angular momentum composition of the Rydberg states produced. By considering the angular momentum selection as well as propensity rules, it is possible to predict the states that should be excited in the wave packet. Firstly as the transition involves the absorption of one photon, the orbital angular momentum must change by ±1. The parity of the states must also be different, while the total angular momentum must be conserved. If we define the total angular momentum of the A-state, $\mathbf{J'}$, the total angular momentum of the Rydberg state, $\mathbf{J}$, and the photon angular momentum, $\gamma = 1$,

$$\mathbf{J} = \mathbf{J'} + \gamma, \tag{3.4}$$

substituting $\gamma = 1$ gives,

$$\mathbf{J} = \mathbf{J}' + 1. \tag{3.5}$$

The total angular momentum of the intermediate state is the sum of its rotational angular momentum, $\mathbf{N}'$, electron spin, $\mathbf{S}'$, and orbital angular momentum, $\mathbf{L}'$. The total angular momentum of the A-state in NO, using Hund's case b) nomenclature is,

$$\mathbf{J}' = \mathbf{N}' + \mathbf{S}', \tag{3.6}$$

while the total angular momentum of the Rydberg state using Hund's case d) nomenclature is,

$$\mathbf{J} = \mathbf{N}^+ + \mathbf{s} + \ell. \tag{3.7}$$

Substituting back into equation 3.4 gives,

$$\mathbf{N}' + \mathbf{S}' + \gamma = \mathbf{N}^+ + \mathbf{s} + \ell, \tag{3.8}$$

as the electron spin cannot change in the transition, $\mathbf{S}' = \mathbf{s}$, and recognising that $\ell = \ell' + 1$, the rotational quantum number of the Rydberg state is determined using,

$$\mathbf{N}' = \mathbf{N}^+ + \ell'. \tag{3.9}$$

Rydberg states are generally described as pure ℓ states; however the non-spherical and non-Coulombic core complicates their angular momentum character, the core causes the angular momentum part of the Rydberg wavefunction to be a superposition of different spherical harmonics. The A-state is a Rydberg state itself and is best described as being a superposition of 94% s, 5% d and smaller contributions from other angular momentum states [43]. This makes things slightly more complicated than the above selection rules suggest. Excitation from the A-state leads to predominantly $p(N')$ states being excited. However, $p(N'+2)$ and $f(N'+2)$ also appear with appreciable intensity in the frequency spectra obtained by a number of groups [25,27-30,32-35,44], using the labeling $\ell(N^+)$ where ℓ is the orbital angular momentum of the Rydberg electron and N^+ is the rotational quantum number of the ion core. In addition very weak series attributed to the s and d states have been detected. The mixed angular momentum character also complicates the molecular angular momentum states excited. For example if we excite from the $N'=1$ intermediate, the $p(1)$ series dominates the spectrum, but the $p(3)$, $f(1)$, $f(3)$, $s(2)$ and $s(0)$ series are also visible but with lower intensity. Vibrational transitions are governed by the Franck-Condon factors. As the A-state is the first in the $^2\Sigma^+$ Rydberg series, the vibrational quantum number does not change due to the similarity in Rydberg state potentials, i.e. the $\Delta v = 0$ propensity rule holds.

3.3. Frequency resolved spectroscopy

In order to design and implement an intelligent coherent control scheme an intimate knowledge of the system you are controlling is required. Although the above selection rules give an idea of the states that can be excited, in most cases a high-resolution frequency spectrum is required in order to really characterize the wave packet. For this reason frequency resolved Rydberg spectra have been recorded via various intermediate states in order to find a suitable region for the control experiments. Figure. 3.3. shows a section of a Rydberg spectrum excited via the $|v' = 1, N' = 0, J' = 1/2\rangle$ level of the A-state. Two distinct series can quite clearly be identified in the frequency spectrum, they are the $p(0)$ and the $f(2)$ series. The highlighted sections in figure 3.3 show parts of the spectrum where the two series are interleaved, while the blank parts show where the two series overlap making the Rydberg spectrum appear simpler. This is an example of the stroboscopic effect in the frequency domain as first seen in the sodium dimer [45]. In the sodium dimer one s and two d series, belonging to different rotational states, were excited via the A $^1\Sigma_u^+$, state. When the two d series lay close in energy, a strong interaction leads to a mixing of the eigenfunctions, large perturbations are then seen in the line positions and transition dipoles of the two series. The perturbations in the transition dipole moments causes all the excitation probability to be transferred to one series and has the effect of removing the other series from the Rydberg spectrum simplifying its appearance. The fringe pattern is seen for homonuclear diatomics when the electronic period is equal to integer multiples of half the rotational period. The Rydberg electron only sees the core at its classical orbit period, generally this is very different from the rotational period of the core so the electron
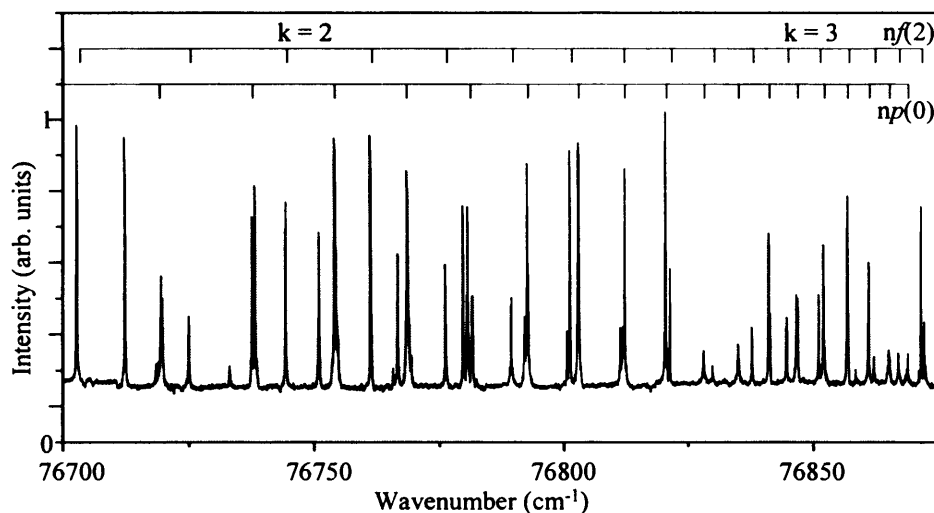
Figure.3.3. *High-resolution frequency spectrum of the autoionising states of NO, excited via the* $\left| v' = 1, N' = 0, J' = 1/2 \right\rangle$ *level of the A-state. Highlighted sections show where the two dominant series are interleaved leading to a complex looking spectrum. Blank sections show regions where the two series overlap making the spectrum appear much simpler. Each stroboscopic region is labeled with its k value.*

therefore sees a scrambled core. Its projection along the internuclear axis is no longer a good quantum number and is therefore best described using a Hund's case (d) coupling scheme. However, in the stroboscopic regions the electron effectively sees a core which has not moved, its projection along the internuclear axis therefore remains a good quantum number and is best described using a Hund's case (a) coupling scheme [46]. This transition from Hund's case (d) to Hund's case (a) causes the change in appearance of the Rydberg spectrum. This transition occurs when the electronic and rotational periods are in resonance, and can be calculated using,

$$v^3 = \frac{k}{4B_v^+(J+1/2)},$$ (3.10)

where k is an integer, $v^3 = 1/\bar{n}^3$ is the average electronic period and $1/4B_v^+(J+1/2)$ is half

the rotational period of the molecular ion, where B_v^+ is the rotational constant of the

molecular ion. Unlike the case in sodium, in NO there is no interaction between the two

series, therefore both remain intense across the entire Rydberg spectrum. With an assigned

frequency spectrum it is now possible to predict the wave packet motion and phase

evolution of the various components excited.

3.4. Design of a coherent control scheme

From the frequency resolved spectrum presented in figure 3.3 it is clear that a wave packet

excited in this system will be composed predominantly of two different rotational states. Is

it possible to design and implement a control scheme using a series of phase locked pulses

to selectively populate one or other of the two rotational series? Can we take the control

scheme described in section 1.3.1 used to control the orbital angular momentum of an

atomic Rydberg electron wave packet [11], and extend it to control molecular systems

where the extra degree of freedom of rotation is introduced? Consider a wave packet

composed of a superposition of two non-interacting molecular Rydberg series, which

converge to different ionization limits corresponding to different rotational states of the

molecular ion, separated by ΔE_{Rot}. This wave packet may be considered as consisting of

two separate components, each of which has its own electronic orbital angular momentum

and is associated with a different rotational state of the molecular ion core. The wave packet can be described mathematically as,

$$\Psi(r,t) = \sum_{n\ell} a_{n\ell} \psi_{n\ell}(r) \exp(-i\omega_{n\ell} t) ,$$

(3.11)

where $a_{n\ell}$ is the amplitude factor of a particular n and ℓ state, $\psi_{n\ell}(r)$ is the radial wavefunction, $\omega_{n\ell}$ is the angular frequency and t is time. Expanding the energy term as a Taylor series gives,

$$
\begin{aligned}
\omega_{n\ell} &= -\frac{1}{2\nu_{n\ell}^2} \\
&= -\frac{1}{2\bar{\nu}^2}\left[1 - 2\left(\frac{\delta\nu}{\bar{\nu}}\right) + \ldots\ldots\right] \\
&= -\frac{1}{2\bar{\nu}^2} + \frac{(\nu_j - \bar{\nu})}{\bar{\nu}^3} - \ldots
\end{aligned}
$$

(3.12)

where $\bar{\nu}$ is the effective principal quantum number defined $\bar{\nu} = n - \mu$, n is the principal quantum number and μ is the quantum defect. The first term in the expansion give the central energy of the wave packet, the second term is the harmonic spacing and gives the classical orbit period of the system, subsequent terms add anharmonicity to the energy spacings adding dispersion effects to the wave packet, and are not required for this analysis. Replacing the expansion back into the exponential in equation 3.11, with the substitution $\bar{\nu} = n - \mu$ gives,

$$\exp\left[-\frac{i(n_t - \bar{n})t}{\bar{n}^3} + \frac{i\mu t}{\bar{n}^3}\right] = \exp\left[-2\pi i(n_t - \bar{n})\frac{t}{t_{cl}}\right]\exp\left[2\pi i\mu\frac{t}{t_{cl}}\right].$$

(3.13)

As the two series are non-interacting, we treat each series as a separate expansion. Labelling the series converging to the lower ionisation limit a, and the series converging to the upper ionisation limit b,

$$\exp(i\omega_a t) = \exp\left[-2\pi i(n_a - \bar{n})\frac{t}{t_{cl}^a}\right]\exp\left[2\pi i\mu_a\frac{t}{t_{cl}^a}\right],$$

(3.14)

$$\exp(i\omega_b t) = \exp\left[-2\pi i(n_b - \bar{n})\frac{t}{t_{cl}^b}\right]\exp\left[2\pi i\mu_b\frac{t}{t_{cl}^b}\right]\exp\left[-2\pi i\frac{t}{T_{Rot}}\right],$$

(3.15)

The final term in the series b expansion takes into account the difference in core rotational state, $T_{Rot} = 2\pi / \Delta E_{Rot}$, where ΔE_{Rot} is the energy difference between the two rotational ionisation limits. The phase difference between the series is therefore the difference in the exponents. Assuming $n_a \approx n_b$ both wave packets return to the core and overlap spatially (i.e. $t \approx t_{cl}^a \approx t_{cl}^b$, which is true for $2v_a^2 \Delta E_{Rot} \ll 1$) the first term in square brackets cancels, leaving at time t,

$$\phi = 2\pi\left(\frac{\mu_a}{t_{cl}^a} - \frac{\mu_b}{t_{cl}^b} + \frac{1}{T_{Rot}}\right)t.$$

(3.16)

The accumulated phase for a given system clearly depends on excitation energy as well as time. When both wave packets return to the core they overlap spatially and interfere with one another. Equation 3.16 can be rearranged to give the stroboscopic periods, $T_s = T_{Rot}(k + \Delta\mu)$ for $\phi = 2\pi k$ [47]. These interference effects have been observed in time-resolved spectra of molecular Rydberg wave packets in NO, manifesting themselves as plateaus in plots of the observed recurrence time as a function of the average principal quantum number in the superposition [48-50]. If a second wave packet is launched at a time when the accumulated phase difference, $\phi = \pi$, it can be engineered so that it interferes constructively with the Rydberg series associated with one rotational quantum state and destructively with the other. Removing one Rydberg series from the superposition has the effect of filtering out the rotational beat, leaving pure electronic motion in the radial coordinate and the core in a well-defined rotational quantum state.

An alternative way to look at the control mechanism is in the frequency domain. Figure 3.4 shows the Fourier transform of a single 1 ps Gaussian laser pulse (equivalent to our experimental pulse) centred at an average energy equivalent to $n_0 = 33$ (figure 3.4 a)), where n_0 is a measure of the energy below the $v^+ = 1, N^+ = 0$ ionisation limit. The Fourier transform of two 1 ps pulses with an average energy equivalent to $n_0 = 33$, separated by the average orbit period of the wave packet is plotted (figure 3.4 b)). Both Fourier transforms are superimposed on a portion of the frequency spectrum presented in figure 3.3, and are centered at $n_0 = 33$. The Fourier transform of a Gaussian, is a Gaussian around the central frequency of the light pulse, while the Fourier transform of non-overlapping Gaussians separated by T_d gives a Gaussian envelope again around the central frequency of the light

pulse, superimposed with a modulation whose angular frequency is $2\pi/T_d$. If $T_d = T_{cl} + t_\phi$, where T_{cl} is the classical orbit period of the wave packet and t_ϕ is the phase difference between the two light pulses, the modulation in the Gaussian will be of angular frequency $2\pi/T_{cl}$ while t_ϕ will control the peak positions within the Gaussian. By careful tuning of the time delay and phase difference between the two pulses, it is possible to overlap the peaks in the modulation with one series and the dips with the other series, leaving only one series in the wave packet (figure 3.4 b)).
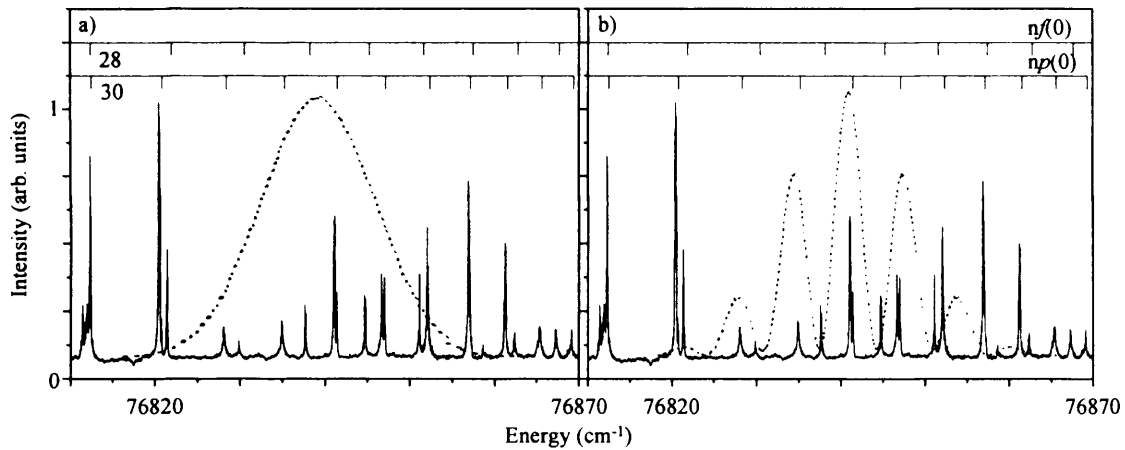
Figure.3.4.   Fourier transforms of a 1 ps pulse a) and two 1 ps pulses separated by the average recurrence time of the p(0) and f(2) series b). The average excitation energies correspond to $n_0 = 33$. The single pulse shows a smooth Gaussian distribution, while the sequence of pulses shows a modulated intensity distribution of energies. By tuning the phase difference between the two pulses the modulation peaks have been tuned to be on top of the p(0) series and the dips above the f(2) series.

3.5. Experimental details

We employ a resonantly enhanced two-photon process to record frequency resolved Rydberg spectra, and wave packet spectra. Approximately 40% of the 532 nm output of a nanosecond Nd:YAG laser (continuum 8020) pumps a nanosecond dye laser (Continuum ND-6000) containing 0.18 g/l of DCM (4-dicyanomethal-2-methyl 1-6-p-diethylaminostyryl 1-4-H-pyran) in DMSO (dimethylsulfoxide). This produces a 6 ns pulse of light at around 646 nm and with a pulse energy of approximately 15 mJ. The fundamental output is frequency doubled and mixed in KDP and BBO crystals to give approximately 1 mJ pulses at around 215 nm. For the frequency-resolved Rydberg spectra, the remaining 60% of the nanosecond Nd:YAG laser is used to pump a second nanosecond dye laser (Sirah Precisionscan) containing 0.30g/l of DCM in DMSO. This produces pulses of light around 660 nm with pulse energies of approximately 8 µJ. The fundamental frequency is then doubled in an auto-tracked KDP crystal to give light at around 330 nm with a pulse energy of approximately 1 µJ. The wavelength can then be scanned over a wide range to obtain a frequency resolved spectrum of Rydberg states with $n = 22 - \infty$. For the wave packet experiments, the second nanosecond laser is replaced by a picosecond laser system. A modelocked picosecond Nd:YAG laser (Coherent Antares) synchronously pumps a picosecond dye laser (Coherent 700 series) containing 2 g/l DCM in benzyl alcohol and ethylene glycol in a 4:6 ratio. This produces a 76 MHz pulse train at around 660 nm, with an average power of 200 mW. The pulse train is then amplified at 20 Hz using a series of Bethune cells pumped with the remaining 60 % of the output from the nanosecond Nd:YAG laser. After the chain of Bethune cells, the average pulse energy is

approximately 300 μJ/pulse. The pulses have a spectral Full Width Half Maximum (FWHM) of 15 cm^{-1}, which assuming a Gaussian pulse profile, corresponds to a pulse of 1 ps in duration. The amplified pulses are then frequency doubled to give light at around 330 nm with pulses of approximately 40 μJ at a repetition rate of 20 Hz. The amplified picosecond light is then used to excite a wave packet from the A-state. The wave packet is composed predominantly of two Rydberg series converging to the $X^1\Sigma^+$, $\upsilon^+ = 1$ state of NO$^+$. For the experiments described here, a sequence of three identical phase-locked picosecond light pulses is required. The first two pulses are the excitation and control pulses whilst the third is the detection pulse. The sequence of phase-locked pulses is generated in a three-armed Michaelson interferometer which is feedback-stabilised to within 0.01 fs for periods of >10 hours. The dynamics of the wave packet following just the excitation pulse, or the excitation plus control pulse sequence, are monitored using the optical Ramsey method. This measures the autocorrelation function of the wave packet by allowing it to interact with another detection wave packet and observing interference fringes in the final Rydberg state population. The autocorrelation function is determined by calculating the root-mean-square of the amplitude of the fringes, which is measured by applying a delayed (100 ns) pulsed electric field (1.7 kVcm^{-1}) to ionise the Rydberg state population and accelerate the NO$^+$ ions along a 20 cm field-free flight tube towards a microchannel plate detector.

3.6 Results

3.6.1 Frequency resolved spectrum and phase evolution

In figure. 3.5.a) we present a high-resolution frequency spectrum of autoionising Rydberg states in the range $27 < n_0 < 40$, where $\bar{n}_0$ is a measure of the average energy below the N^+ = 0 ionisation limit, converging to the $v^+ = 1$ ionisation limit of the $X^1\Sigma^+$ state of NO^+.
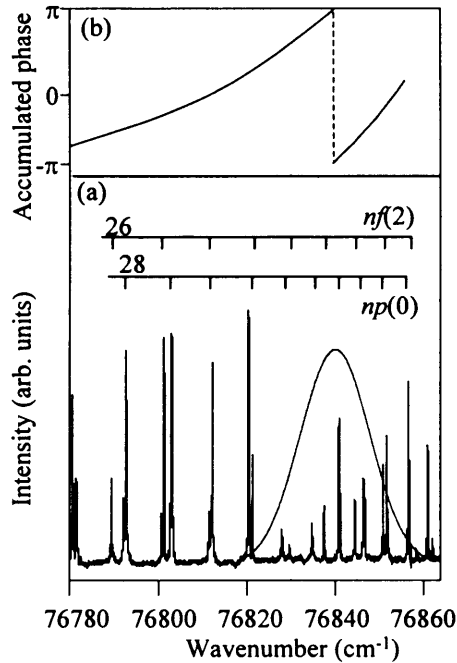
Figure.3.5. (a) Part of the $1 + 1'$ double resonance frequency spectrum of Rydberg states in NO excited via the $v' = 1, N' = 0$ level of the $A^2\Sigma^+$ state. Combs mark the positions of the dominant np(0) and nf(2) series. A Gaussian centered at $\bar{n}_0 = 33$ (FWHM = 14 cm^{-1}) is superimposed on the spectrum, representing the optical pulse employed in our control experiments. (b) A plot of the accumulated phase-difference ϕ at time t_{ave}, calculated using equation 3.18.

The spectrum presented in figure 3.5 was recorded following excitation via the $A^2\Sigma^+|v' = 1, N' = 0, J' = 1/2\rangle$ level of NO and it is clear that the p(0) and f(2) series

dominate the autoionisation spectrum. The accumulated phase-difference, ϕ, between these

two series at the average time of the first recurrence, is calculated using equation 3.16 for

the same region of the Rydberg spectrum, and is plotted in modulo 2π in figure. 3.5.b).

From this plot, it is apparent that ϕ is an odd multiple of π at around 76,840 cm^{-1}, which

corresponds to $\bar{n}_0 = (-2\varepsilon_0)^{-1/2} = 33$.

The effect of ϕ on the optically induced interference fringes in a wave packet

spectrum can be determined by separating out the $p(0)$ and $f(2)$ series and using the

experimental frequencies ω and intensities $a_{N^+}^2(\omega)$. The subscript N^+ is used to label the

rotational quantum state of the molecular ion core. The spectrum is convoluted with a

Gaussian of FWHM = 14 cm^{-1}, which is equivalent to our experimental laser pulse,

centered around $\bar{n}_0 = 33$. The time-dependent interference term of the Rydberg population,

$A_{N^+}^2(t)$ for each rotational state of the molecular ion core is calculated around the average

time of the first recurrence, $t = t_{cl}$, using,

$$A_{N^+}^2(t) = \mathrm{Re}\sum_{\omega} a_{N^+}^2(\omega)e^{-4\ln 2(\omega-\omega_L)^2/\sigma^2}e^{-i\omega t}, \tag{3.17}$$

where ω_L is the average excitation frequency of the laser pulse. The interference terms

$A_0^2(t)$ and $A_2^2(t)$, are plotted in figure. 3.6 as solid (larger amplitude) and dashed (smaller

amplitude) lines respectively, around the time of the average classical orbit period $t_{ave} =$

5.04 ps. The interference terms are out of phase with one another. It is clear that adding the

second wave packet at $t_2 = 5.041$ ps would result in constructive interference with the

$N^+ = 0$ series and destructive interference with the $N^+ = 2$ series. This would leave a

molecular electron wave packet in a well-defined rotational quantum state with $N^+ = 0$.

Flipping the optical phase of the second laser pulse by π will reverse the situation and leave

the molecular electron wave packet in a well-defined rotational quantum state with

$N^+ = 2$.
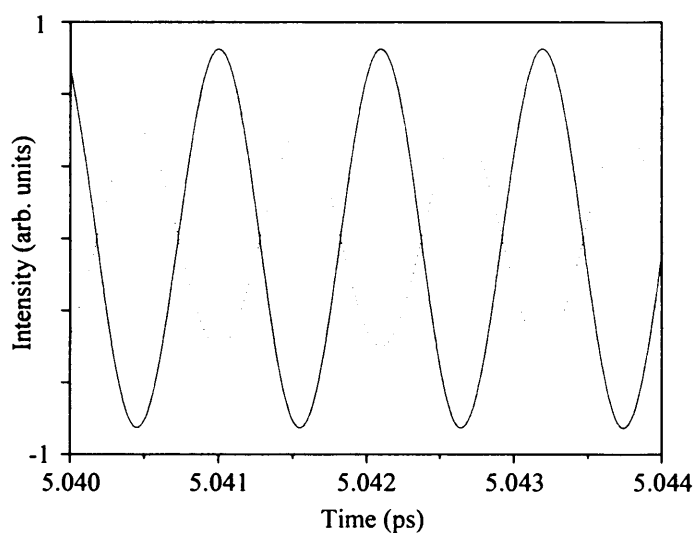
Figure.3.6. *The time-dependent interference term of the Rydberg population at time t_{ave}, calculated using equation 3.17 for excitation around $\bar{n}_0 = 33$ contribution from both the p(0) series ( ) (larger amplitude) and that from the f(2) series (⋯) (smaller amplitude)are shown. It can be seen that the two components are phase mismatched around the time of the first recurrence.*

3.6.2. Wave packet Control

This control scheme is illustrated in figure. 3.7 where (a) are experimental spectra and (b) are the corresponding calculated spectra. The bottom trace in figure 3.7(a) shows the experimental recurrence spectrum following excitation of a single wave packet. The first

recurrence exhibits the double peak structure that has been observed in previous experiments [48-50]. The dip corresponds to destructive interference between the two wave packets when they return to the core with an accumulated phase-difference of π, and is observed at time t_{ave}. Adding the second control wave packet to the system at this time allows us to manipulate the final state Rydberg population. Experimental recurrence spectra are recorded following excitation of two pulses separated by t_{ave} with a suitable phase added to leave the $N^+ = 0$ series only (middle trace) or the $N^+ = 2$ series only (top trace). For a given excitation energy the period of motion of a wave packet in a system with the core in the lower rotational state will be longer and this is illustrated well by these spectra. The position of the first recurrence in the middle plot is 5.6 ps, which agrees well with the calculated orbit period of a wave packet with $\bar{n}_0 = 33$, $t_{cl} = 2\pi\bar{n}^3 = 5.5$ ps. The first recurrence in the upper plot appears at 4.3 ps which is close to the calculated orbit period for $\bar{n}_2 = 31.2$, $t_{cl} = 4.6$ ps. Effectively, the double peak feature has been deconvoluted into its two contributing components.

The equivalent calculated recurrence spectra are obtained using the modified autocorrelation function,

$$\langle\Psi(0)|\Psi(t)\rangle = \sum_{N^+,\omega} a_{N^+}^2(\omega) e^{-4\ln 2(\omega-\omega_L)^2/\sigma^2}\left[e^{-i\omega t} + e^{-i\omega(t+t_2)}\right]. \tag{3.18}$$

The first term in square brackets describes the temporal evolution of the excitation wave packet created at $t = 0$, the second term describes the evolution of the control wave packet

launched at $t_2 = t_{ave} + t_\phi$, where t_ϕ is the delay which corresponds to an optical phase ϕ.

All spectra are normalized on the $t = 0$ peak and plotted on the same vertical scale and, in the experiments involving a sequence of pulses, time zero corresponds to the launch of the control wave packet.
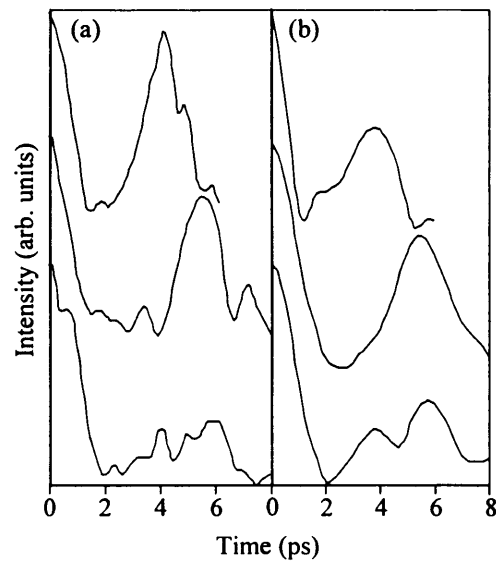
Figure.3.7. Experimental (a) and calculated (b) recurrence spectra of a wave packet with $\bar{n}_0 = 33$. The bottom spectrum is that of a single wave packet. The middle spectrum is that of a sequence of pulses separated by t_{ave} with a suitable phase-difference to leave the $N' = 0$ series only. The top spectrum is that of a sequence of pulses separated by t_{ave} with a suitable phase-difference to leave the $N' = 2$ series only. Note that all spectra, experimental and calculated, are plotted on the same vertical scale, normalized on the peak at $t = 0$.

We can investigate the effectiveness of the control scheme in more detail by calculating the population distribution after a sequence of two pulses $A^2(\omega)$, assuming the

intensity of the laser pulses is sufficiently weak that the population of the intermediate A-state remains virtually unchanged. The method is the same as that employed to determine the population distribution in Schrodinger cat states [51] as derived in section 2.6,

$$A^2(\omega) \propto \left[\sum_{N^+} a_{N^+}(\omega) e^{-2\ln 2(\omega-\omega_L)^2/\sigma^2} [1 + e^{i\Delta t_2} e^{i(\omega-\omega_L)t_2}] \right]^2 .$$

(3.19)

$\Delta = \omega_L - \omega_0$ where ω_0 is the frequency of the intermediate. After launching the control pulse at t_2 = 5.041 ps (corresponding to the middle trace in figure. 3.7) the population distribution is calculated using equation (3.19) and plotted as the positive trace in figure 3.8. The peaks in the positive trace in figure 3.8 correspond to the line positions of the $np(0)$ Rydberg series and it is clear that there is very little contamination from other states in the wave packet, thus verifying that the molecular ion core is in a well-defined quantum state with $N^+ = 0$. Flipping the phase of the optical pulse by π, generates the population distribution plotted as the negative trace in figure 3.8. The peaks in this plot correspond to the line positions of the $nf(2)$ Rydberg series, and again there is very little contamination from other states. In this case the molecular ion core has a well-defined quantum state with $N^+ = 2$. It is clear from these two plots that the level of control is excellent.
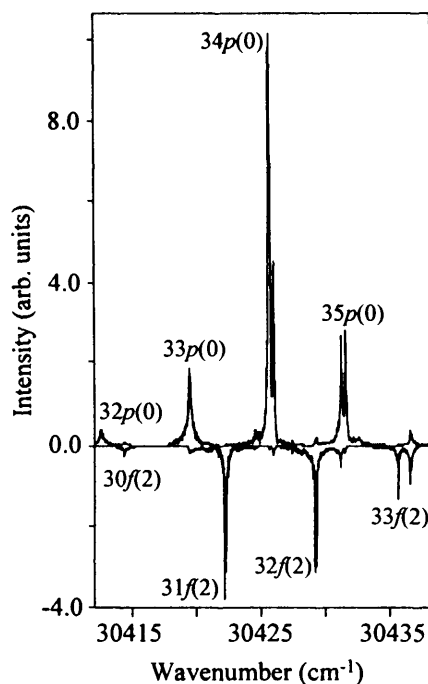
Figure.3.8. Population distributions determined using equation 3.19. Positive peaks represent the final state distribution obtained when the second pulse is added at $t_2 = 5.041$ ps (corresponding to the middle trace in figure. 3.7). Flipping the phase of the second wave packet yields the population distribution that is plotted on a negative scale (corresponding to the top trace in figure. 3.7).

3.7 Summary

Using a train of phase-locked pulses we have been able to select the rotational quantum state of the molecular ion core. The control scheme is not specific to the quantum numbers demonstrated here but can be extended to any rotational state of the core by simply exciting via a different intermediate. The degree of control has been fully characterised by determining the population distribution after a particular pulse sequence and it is extremely effective. The additional phase parameters inherent in a molecular system aid the control mechanism in some respects, as one can search for a phase-mismatch specifically at the

first recurrence, where dispersion is less of a problem. By looking at the control pulses in both the time and frequency domain, it is possible to gain a greater understanding of how the control mechanism works. In general terms, if the accumulated phase-difference can be determined, a logical pulse sequence can be designed to control the final state quantum distribution.

3.8. References.

1   J. Bromage and C. R. Stroud, Physical Review Letters **83** (24), 4963 (1999).

2   J. Degert, W. Wohlleben, B. Chatel, M. Motzkus, and B. Girard, Physical Review Letters **89** (20), 203003 (2002).

3   N. V. Vitanov and B. Girard, Physical Review A **69** (3), 033409 (2004).

4   M. Wollenhaupt, A. Assion, D. Liese, C. Sarpe-Tudoran, T. Baumert, S. Zamith, M. A. Bouchene, B. Girard, A. Flettner, U. Weichmann, and G. Gerber, Physical Review Letters **89** (17), 173001 (2002).

5   J. Ahn, D. N. Hutchinson, C. Rangan, and P. H. Bucksbaum, Physical Review Letters **86** (7), 1179 (2001).

6   J. Ahn, T. C. Weinacht, and P. H. Bucksbaum, Science **287** (5452), 463 (2000).

7   R. R. Jones and M. B. Campbell, Physical Review A **6001** (1), 013403 (2000).

8   M. W. Noel and C. R. Stroud, Physical Review Letters **77** (10), 1913 (1996).

9   R. van Leeuwen, M. L. Bajema, and R. R. Jones, Physical Review Letters **82** (14), 2852 (1999).

10   R. van Leeuwen, K. Vijayalakshmi, and R. R. Jones, Physical Review A **6303** (3),

033403 (2001).

11   J. R. R. Verlet, V. G. Stavros, R. S. Minns, and H. H. Fielding, Physical Review

Letters **89** (26), 263004 (2002).

12   J. R. R. Verlet, V. G. Stavros, R. S. Minns, and H. H. Fielding, Journal of Physics

B-Atomic Molecular and Optical Physics **36** (17), 3683 (2003).

13   T. C. Weinacht, J. Ahn, and P. H. Bucksbaum, Physical Review Letters **81** (14),

3050 (1998).

14   T. C. Weinacht, J. Ahn, and P. H. Bucksbaum, Physical Review Letters **80** (25),

5508 (1998).

15   T. C. Weinacht, J. Ahn, and P. H. Bucksbaum, Nature **397** (6716), 233 (1999).

16   M. W. Noel and C. R. Stroud, Physical Review Letters **75** (7), 1252 (1995).

17   C. Rangan and P. H. Bucksbaum, Physical Review A **6403** (3), 033417 (2001).

18   H. Wen, C. Rangan, and P. H. Bucksbaum, Physical Review A **68** (5), 053405

(2003).

19   R. S. Judson and H. Rabitz, Physical Review Letters **68** (10), 1500 (1992).

20   D. B. Keck and C. D. Hause, Journal of Molecular Spectroscopy **26** (2), 163 (1968).

21   G. Herzberg, *Spectra of diatomic molecules*. (Cornell university press, 1971).

22   K.P. Huber and G. Herzburg, *Constants of diatomic molecules*. (Van Nostrand,

New York, 1979).

23   K. P. Huber, M. Huber, and E. Miescher, Physics Letters **3** (7), 315 (1963).

24   C. Jungen and E. Miescher, Canadian Journal of Physics **47** (17), 1769 (1969).

25   E. Miescher, Journal of Molecular Spectroscopy **20** (2), 130 (1966).

26   E. Miescher, Journal of Molecular Spectroscopy **53** (2), 302 (1974).

27   E. Miescher, Canadian Journal of Physics **49** (18), 2350 (1971).

28   E. Miescher, Canadian Journal of Physics **54** (20), 2074 (1976).

29   E. Miescher, Y. T. Lee, and P. Gurtler, Journal of Chemical Physics **68** (6), 2753
(1978).

30   E. F. McCormack, F. Di Teodoro, J. M. Grochocinski, and S. T. Pratt, Journal of
Chemical Physics **109** (1), 63 (1998).

31   A. Fujii and N. Morita, Journal of Chemical Physics **103** (14), 6029 (1995).

32   A. Fujii and N. Morita, Laser Chemistry **13** (3-4), 259 (1994).

33   A. Fujii and N. Morita, Journal of Chemical Physics **98** (6), 4581 (1993).

34   A. Fujii and N. Morita, Journal of Chemical Physics **97** (1), 327 (1992).

35   A. Fujii and N. Morita, Chemical Physics Letters **182** (3-4), 304 (1991).

36   S. Fredin, D. Gauyacq, M. Horani, C. Jungen, G. Lefevre, and F. Masnouseeuws,
Molecular Physics **60** (4), 825 (1987).

37   S. T. Pratt, J. L. Dehmer, and P. M. Dehmer, Journal of Chemical Physics **90** (4),
2201 (1989).

38   S. T. Pratt, C. Jungen, and E. Miescher, Journal of Chemical Physics **90** (11), 5971
(1989).

39   C. Jungen, Journal of Chemical Physics **53** (11), 4168 (1970).

40   M. Raoult, Journal of Chemical Physics **87** (8), 4736 (1987).

41   A. Giustisuzor and C. Jungen, Journal of Chemical Physics **80** (3), 986 (1984).

42   I. Rabadan and J. Tennyson, Journal of Physics B-Atomic Molecular and Optical
Physics **30** (8), 1975 (1997).

43   K. Kaufmann, C. Nager, and M. Jungen, Chemical Physics **95** (3), 385 (1985).

44   Y. Ono, S. H. Linn, H. F. Prest, C. Y. Ng, and E. Miescher, Journal of Chemical Physics **73** (10), 4855 (1980).

45   S. Martin, J. Chevaleyre, M. C. Bordas, S. Valignat, M. Broyer, B. Cabaud, and A. Hoareau, Journal of Chemical Physics **79** (9), 4132 (1983).

46   P. Labastie, M. C. Bordas, B. Tribollet, and M. Broyer, Physical Review Letters **52** (19), 1681 (1984).

47   R. A. L. Smith, V. G. Stavros, J. R. R. Verlet, H. H. Fielding, D. Townsend, and T. P. Softley, Journal of Chemical Physics **119** (6), 3085 (2003).

48   R. A. L. Smith, J. R. R. Verlet, E. D. Boleat, V. G. Stavros, and H. H. Fielding, Faraday Discussions (115), 63 (2000).

49   V. G. Stavros, J. A. Ramswell, R. A. L. Smith, J. R. R. Verlet, J. Lei, and H. H. Fielding, Physical Review Letters **83** (13), 2552 (1999).

50   V. G. Stavros, J. A. Ramswell, R. A. L. Smith, J. R. R. Verlet, J. Lei, and H. H. Fielding, Physical Review Letters **84** (8), 1847 (2000).

51   X. Chen and J. A. Yeazell, Physical Review A **55** (4), 3264 (1997).

Chapter 4. Observation of a dissociating Rydberg electron wave packet and control of the autoionisation:predissociation ratio in NO.

4.1. General

The added complexities that molecular systems bring to autoionising Rydberg wave packet dynamics were introduced in chapter 3, namely that the additional rotational and vibrational degrees of freedom and associated ionisation and dissociation continua complicate things quite considerably. Interference effects in the wave packet system manifest themselves as deviations in the recurrence times of autoionsing Rydberg wave packets [1-4]. These effects can be explained in terms of the phase evolution of the various series excited within the wave packet. In NO, two Rydberg series are excited, a $p(N^+)$ series and an $f(N^++2)$ series, using the nomenclature $l(N^+)$ where l is the orbital angular momentum of the Rydberg electron and N^+ is the rotational angular momentum of the ion core. A wave packet composed of two series can be thought of as consisting of two separate wave packets, one for each series. These will interfere with one another when they overlap spatially. If both wave packets return to the core out of phase with one another they interfere destructively and no Rydberg population will be left; however, if they return to the core in phase with one another, they interfere constructively and the total Rydberg

population is amplified. With knowledge of the phase evolution of the various components in the wave packet, it is possible to predict and control the motion of the wave packet (chapter 3). Having studied and analysed the ionisation channel in some detail, the next step is to study the competing dissociation process, and to see whether this competition can be controlled using a simple pulse sequence.

Control of competing ionisation and dissociation processes has so far not been demonstrated using Rydberg wave packets; it has, however, been the subject of a great deal of interest in the frequency domain [5-11]. In the Gordon group [5-7] competing one- and three-photon pathways to ionisation and dissociation continua have been used to alter the ionisation:dissociation ratio in DI. Three photons of frequency ω_1, and one photon of its third harmonic frequency, $\omega_3 = 3\omega_1$, provide excitation pathways to degenerate ionisation and dissociation continua. The total population in either continuum is the square of the sum of the two excitation pathways, including a cross term containing the relative phase of the two pathways. By tuning the phase difference between ω_3 and ω_1, the population in either channel can be modified. The difference between the phases required to maximize the population in each of the ionisation and dissociation channels is termed the phase lag. If the phase lag is π (as the phase is scanned the ionisation and dissociation signals show completely opposite maxima and minima), as is the case for DI, maximum contrast is attainable.

4.2. Decay processes

On the whole, Rydberg states are extremely long lived. Their radial distribution functions peak at large distances from the core giving very little overlap with lower lying states. Consequently the probability of radiative decay is greatly reduced. However, excitation of a Rydberg state above the lowest ionisation or dissociation limit of the system, allows for an exchange of energy between the Rydberg electron and the ionic core. For example, consider a Rydberg state excited above the lowest ionisation limit of the system; as the electron collides with the core it can gain enough energy to escape the Coulomb potential and ionise. In molecular systems, if the Rydberg state is above the lowest vibrational or rotational ionisation limit, as the electron collides with the core, the extra energy due to the molecular motion can be imparted to the electron. The electron gains enough energy to ionise and by conservation of energy, the core relaxes back down to a lower quantum state. This process is known as autoionisation and is not only limited to molecular systems; for example, atoms can also spin-orbit autoionise. Quantum mechanically, autoionisation can be explained as follows. The Rydberg states are embedded in the ionisation continua associated with a lower energy quantum state of the ionic core. The Rydberg state is coupled to the continuum making the wavefunction only quasibound.
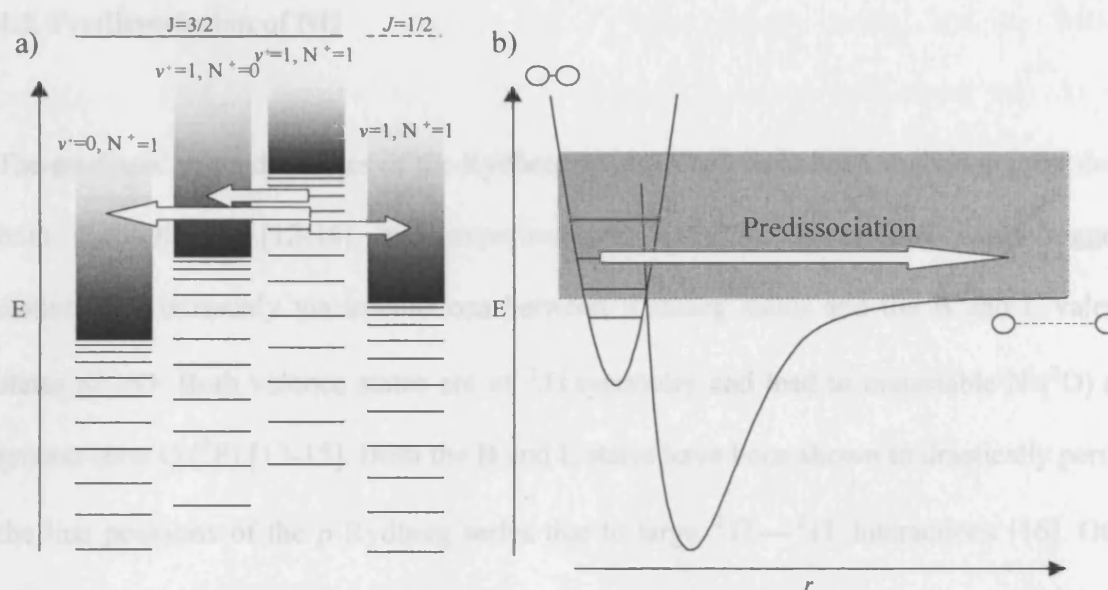
Figure.4.1. Schematic representations of a) autoionisation and b) predissociation. Autoionisation can proceed when the core relaxes to a lower spin orbit, vibrational or rotational state with the excess energy going to the outgoing electron. Predissociation occurs when the excited state lies above the dissociation limit of an electronic state of the neutral molecule which crosses it.

There is another relaxation pathways which is peculiar to molecular systems. Predissociation occurs when a Rydberg state crosses another electronic state of the neutral molecule above its dissociation limit. Classically when the electron collides with the core, its energy is imparted into molecular vibration leading to dissociation of the molecule. Or speaking more quantum mechanically, the Rydberg state is now degenerate with the dissociation continuum and is coupled to the dissociating continuum. The wavefunction is again only quasibound and has some probability of leaking onto the dissociating surface giving atomic products. Schematic representations of autoionisation and predissociation are given in figure 4.1.

4.3. Predissociation of NO

The predissociation dynamics of the Rydberg states of NO have been studied in great detail both theoretically [12-16] and experimentally [17-23]. Theoretical work suggests dissociation is mainly via interactions between Rydberg states and the B and L valence states of NO. Both valence states are of $^2\Pi$ symmetry and lead to metastable N (^{2}D) and ground state O (^{3}P) [13-15]. Both the B and L states have been shown to drastically perturb the line positions of the p Rydberg series due to large $^2\Pi$—$^2\Pi$ interactions [16]. Other dissociation channels are available, most importantly to ground state nitrogen (^{4}S) and oxygen (^{3}P) via the A $^2\Sigma^+$ valence state [13-15], and the I $^2\Sigma^+$ state leading to N(^{2}D) and O(^{3}P). The A, B and I valence states cross the molecular ions ground state around its $v^+ = 0$ vibrational level, while the L state does not cross until above the $v^+ = 2$ vibrational level of the molecular ions electronic ground state.

Predissociation of NO was first seen experimentally in the frequency domain as line broadening of the p states due to their reduced lifetimes, firstly in the absorption spectroscopy of Miescher [24] and subsequently in the double resonance spectroscopy of others [25-27]. Fuji and Morita [17-21] and others [22,23], then carried out major studies of predissociation in NO, by detecting the dissociation products following excitation of the Rydberg states of NO. This work confirmed the earlier predictions that the line broadening seen in the absorption spectra was due to predissociation and also the theoretical predictions that the p states predominantly predissociate (up to 90%) [13]. The higher angular momentum of the f states means that they do not penetrate the core to the same extent as p states, and so the probability of predissociation is reduced. The lack of core

penetration however also enhances the f states autoionisation lifetime, making predissociation a possible but less likely decay route. The f states therefore, show no line broadening [24-26] but are detected in the product yield spectra of Fuji and Morita [17,18,20]. s states predominantly autoionise, however they have been detected as extremely weak peaks in the studies of Fuji and Morita as both the metastable products via the I state and ground state products via the A state [17]. In all predissociation experiments the p states have been shown to dominate the spectra.

4.4 Experimental Details

In our work we observe both the autoionisation and predissociation pathways following excitation of Rydberg wave packets above both the lowest ionisation and predissociation limits. The excitation scheme is illustrated in figure. 4.2. NO is excited from its ground, X $^2\Pi_{3/2}$, state to a specific ro-vibrational level of the first excited state, A $^2\Sigma^+$, using the output of a narrow bandwidth nanosecond laser (not shown in figure 4.2.). From this launch state, the output of a broad bandwidth picosecond laser, coherently excites a number of Rydberg states lying above the lowest ionisation and dissociation limits. The selection rules concerning the excitation of Rydberg states are the same as described in chapter 3. To monitor the products of the autoionisation and predissociation decay processes, we either collect the NO^+ ions generated by autoionisation, or the N^+ ions produced by REMPI of the Metastable N $^2D_{5/2}$ atoms generated by predissociation. The Optical Ramsey Method (ORM) [28] is exploited to measure the autocorrelation function of either autoionising or predissociating Rydberg wave packets.
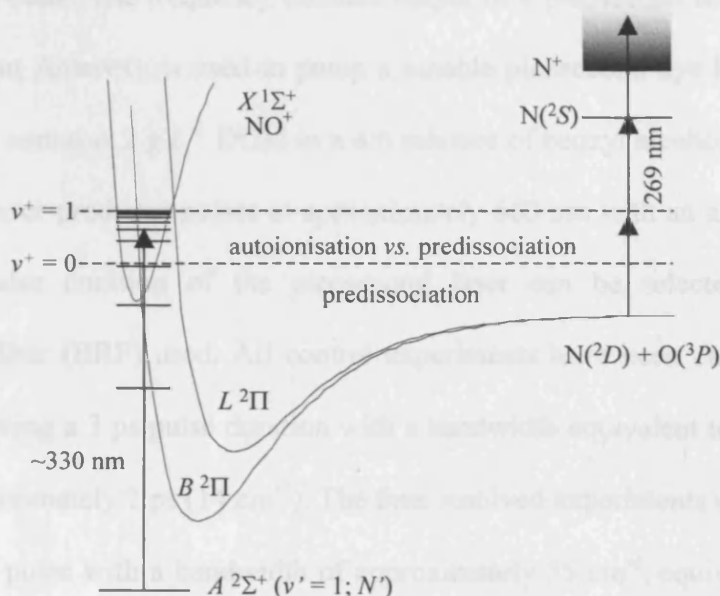
Figure.4.2.   Potential energy diagram, illustrating the excitation process (not to scale). A nanosecond laser is employed to excite a specific ro-vibrational level of the A-state. A picosecond laser operating at around 330 nm is then used to create a Rydberg wave packet above the lowest ionisation limit. The wave packet may dissociate upon its return to the core, this process goes predominantly via the B state. The N ^2D dissociation product can then be detected using $(2 + 1)$ REMPI via the ^2S state using nanosecond light at 269 nm.

Experimentally, we use approximately 80 mJ/pulse of the frequency doubled output of a 10 Hz Q-switched nanosecond Nd:YAG (Continuum 8010) laser, to pump a nanosecond dye laser (Continuum ND6000). The dye laser contains 0.18 gL^{-1} DCM dissolved in DMSO producing light at around 645 nm with a power of approximately 12 mJ/pulse. The output is then frequency doubled in KDP then the doubled light is mixed with the fundamental in BBO to generate the third harmonic of the fundamenmtal, at around 215 nm, and this wavelength of light is used to excite a particular ro-vibrational

level of the A-state. The frequency doubled output of a picosecond mode-locked Nd:YAG laser (Coherent Antares), is used to pump a tunable picosecond dye laser (Coherent 700). The dye laser contains 2 g L^{-1} DCM in a 4:6 mixture of benzyl alcohol and ethylene glycol and the dye laser produces pulses at approximately 660 nm with an average power of 250 mW. The pulse duration of the picosecond laser can be selected by changing the birefringent filter (BRF) used. All control experiments have been carried out with a two plate BRF, giving a 3 ps pulse duration with a bandwidth equivalent to a transform limited pulse of approximately 1 ps (14 cm^{-1}). The time resolved experiments used a one plate BRF giving a 1 ps pulse with a bandwidth of approximately 35 cm^{-1}, equivalent to a bandwdth limited 0.7 ps pulse. The picosecond pulses are then amplified in a series of three Bethune cells containing DCM in methanol. The cells are pumped with the remaining frequency doubled output from the nanosecond Nd:YAG (approximately 160 mJ/pulse). Amplification gives pulses up to 350 μJ/pulse, which are then frequency doubled to give light at around 330 nm with approximately 50 μJ/pulse. The picosecond light is then guided into a stabilised Michaelson interferometer (section 2.2.2.), where each pulse is split into two identical pulses with a controllable time and phase difference between them. The resulting pulses are subsequently combined with the 215 nm nanosecond radiation, and are used to excite and detect the Rydberg wave packet. To detect the predissociation products by REMPI, a final light pulse around 269 nm is required. The frequency tripled output of the nanosecond Nd:YAG laser (Continuum 8010) (355 nm with approximately 120 mJ/pulse) pumps a second nanosecond dye laser (Sirah Precisionscan) containing 1.08 g L^{-1} Coumarin 540A in methanol. The output is frequency doubled to give light at 269 nm at a power of 0.8 mJ/pulse, and the 269 nm light pulse is then delayed by approximately 10 ns

before being combined with the 215 nm nansosecond and 330 nm picosecond light. A schematic diagram of the optical bench arrangement is given in figure 4.3.
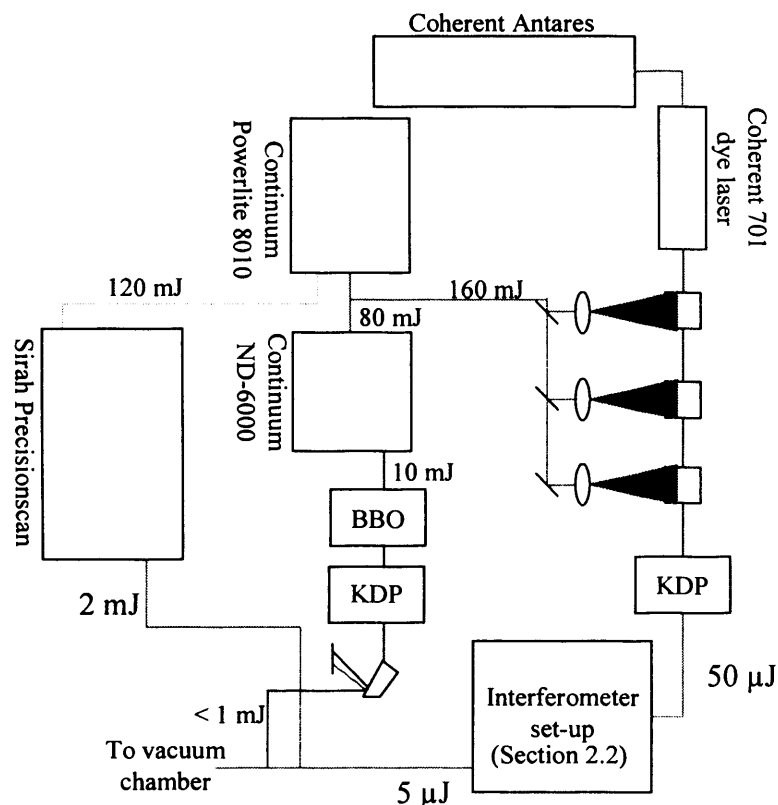
Figure. 4.3. Schematic diagram of the optical set-up used for the wave packet experiments in the predissociating states of NO. A nanosecond Nd:YAG laser is used to pump two nanosecond dye laser and amplifier cells for the picosecond pulses. The picosecond pulses are produced by pumping a picosecond dye laser with a picosecond Nd:YAG. The light from both dye lasers pass through non-linear crystals to obtain the appropriate wavelengths and all powers are given per pulse

Calibration of the REMPI laser can be achieved by blocking all other laser beams and focusing it into the chamber, an accidental resonance with the $9p$ $v = 1$ state in NO [17], at the wavelengths required to ionize the two spin orbit states of $N(^2D)$, allows one to

tune the nanosecond laser to one or other product (figure 4.4). In all the wave packet experiments, spin orbit effects are neglected and we only detect the $J = 5/2$ product due to its higher multiplicity, as in the experiments of Fuji and Moritta.
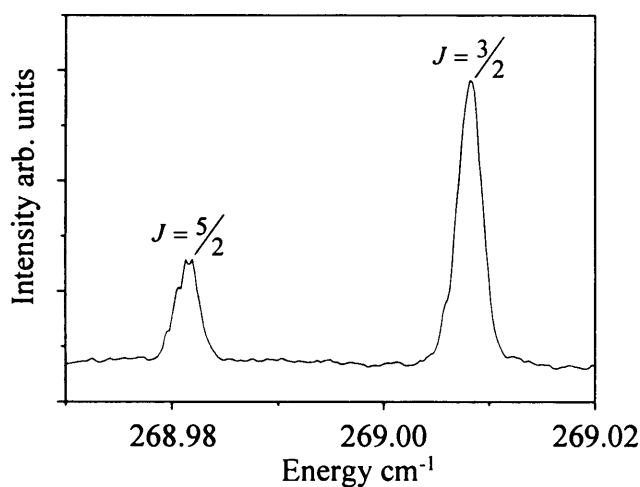
Figure.4.4.REMPI spectrum of the two spin orbit states of N (^2D_J) obtained via an accidental resonance in NO. The two spin orbit states are labeled with their J values.

The lifetime of the N $^2D_{5/2}$ product we detect is approximately 10^5 s [29], and therefore the timing of the REMPI pulse is not crucial, this allows us to temporally separate the REMPI pulse from all other pulses, reducing the probability of other competing excitation pathways. N^+ and NO^+ ions are separated in a time of flight (TOF) apparatus. A pulsed electric field is applied around 100 ns after the last light pulse and accelerates the NO^+ and N^+ ions through a 20 cm field free TOF tube towards a microchannel plate (MCP) detector. Here we can gate on either of the two ion signals, which are amplified using a series of two fast pre-amplifiers (Ortec EG&G VT120) and monitored on a digital oscilloscope (LeCroy 9350A)

Alignment of the three beams is achieved by first maximizing the NO^+ signal by overlapping the initial nanosecond and picosecond beams in the vacuum chamber. The time delayed REMPI pulse is then combined with the other pulses and the N^+ signal is maximized. As the excitation of our wave packet is perturbative, the population in the A-state remains at 1 until the REMPI laser pulse arrives. The REMPI laser causes the NO^+ signal to grow several orders of magnitude due to ionisation of the population remaining in the first excited state of NO. The most sensitive parameter in these experiments is therefore the power of the nanosecond laser that excites the intermediate in NO. The large NO^+ signal and the use of high MCP voltages and two pre-amps causes high experimental noise (signal to noise ratio of approximately 3:1, compared with the autoionising work which had a ratio of 10:1) when compared with the autoionising work. The experiments are therefore more time consuming due to the added need for averaging.

4.5 Results

4.5.1 Predissociating wave packet dynamics

The dynamics of predissociating Rydberg wave packets have been studied over a range of energies $(25 < n < 35)$ via two intermediates, the $N' = 0$ and $N' = 1$ rotational levels of the $v' = 1$ vibrational level of the A-state, and some typical spectra are presented in figure 4.5. In figure 4.5 a) we show a wave packet excited via the $\left| v' = 1, N' = 1, J' = 1/2 \right\rangle$ level of the A-state at around $n_1 = 28.2$ (where n_{N^+} is the average principal quantum number measured in the series $l(N^+)$). The recurrence time is 3.5 ps and a full revival can be seen after

around 31 ps. A second order partial revival is also observed around 15.5 ps. The hydrogenic periods are in agreement with the measured times: t_{cl} = 3.4 ps, T_R = 31.8 ps and $T_R / 2$ = 15.9 ps.
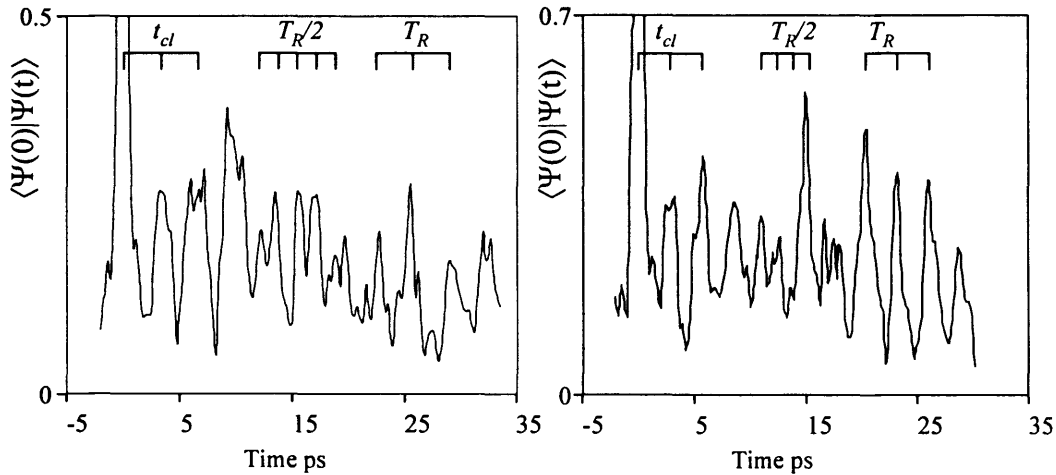
Figure.4.5.   a) and b) are representative time spectra collected via $\left| v' = 1, N' = 1, J' = 1/2 \right\rangle$ at an average excitation energy of n = 28.0 and n = 26.6 respectively. Both recurrence spectra show classical orbit periods in good agreement with hydrogenic models. Clear full and second order partial revivals can be seen and these also agree with hydrogenic models.

The recurrence spectrum shown in figure 4.5.b) is for a wave packet excited via the same intermediate but at a slightly lower energy (n_1= 26.9). In this case the recurrence time is 2.9 ps, with a second order partial revival at 13.2 ps and a full revival at 25.7 ps. These again agree very well with hydrogenic periods (t_{cl} = 2.9 ps, T_R = 25.4 ps and $T_R / 2$ = 12.7 ps). From these and a series of other similar long-time spectra and with knowledge of the frequency domain spectroscopy previously carried out, we can deduce that the predissociating Rydberg wave packet is composed predominantly of a single p Rydberg series converging to the $N^+ = N'$ ionisation limit.

94

In chapter 3 we discussed how having a mixture of different series in a wave packet showed up in plots of the classical orbit period against energy, as plateaus at the stroboscopic period. In the autoionising channel, the wave packet was composed of a p series, and an f series belonging to a higher rotational state of the core, in a ratio of approximately 1:1. The system could be viewed as one in which there are two independent electron wave packets with p and f character, converging to the $N^+ = N'$ and $N^+ = N' + 2$ rotational states of the molecular ion, respectively. These two wave packets return to the core periodically and, when they overlap spatially, they interfere with one another. The interference pattern depends on the molecular phase (from the rotational wave functions) and the electronic phase (whose origin lies in the quantum defects of the two Rydberg series). Peaks in the time-resolved spectrum are observed when the two wave packets return in phase with one another, which occurs at times, referred to as the stroboscopic period [1-4]. By plotting similar graphs for the predissociating wave packet we should be able to determine if any other series do contribute to the system. The strength of the plateaus, i.e. how well defined they appear, depends on the relative populations of the two series excited. If the two series have very similar intensities (the $p(N')$ and $f(N'+2)$ series have almost equal intensities in the autoionising spectra of NO for $N' = 0$ and 1) the plateaus will be quite pronounced; however, if one series is much weaker than the other then the effect will be much less obvious. The position of the plateaus can be calculated using

$$T_s = T_{rot}(k + \Delta\mu),$$
(4.1)

where $T_{rot} = 2\pi/\Delta E_{rot}$, is the rotational beat period with ΔE_{rot} being the energy difference

between the two ionisation limits of the two angular momentum series, k is an integer and

$\Delta\mu = \mu_f - \mu_p$, is the quantum defect difference between the two series. If we now plot the

time of the first experimentally observed peak in the dissociating wave packet spectrum as

a function of the average principal quantum number, we can determine whether the

predissociating wave packet is composed entirely of one Rydberg series or whether other

series are contributing to it. Figure 4.6. represents such a plot obtained using spectra

recorded following excitation of a predissociating wave packet via the $|v'=1$, $N'=0$, $J'=$

½⟩ level of the intermediate.
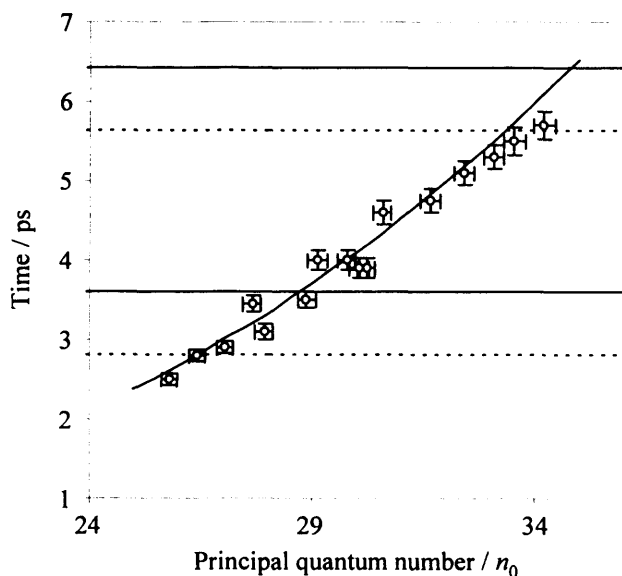
Figure.4.6. A plot of the time of the first experimentally observed peak in the dissociating wave packet
spectrum as a function of the average principal quantum number n_0, obtained using spectra
recorded following excitation via the $|v'=1, N'=0, J'=$ ½⟩ level of the intermediate. The curve
represents the classically expected orbit period for single series excitation of p(0) states,
$t_{cl} = 2\pi n_0^3$. The horizontal lines represent the stroboscopic periods for interference between
p(0) and f(2) series (solid) and for the p(0) and p(2) series (dashed) calculated using equation
4.1.

Overall, the points follow the classically expected orbit periods for single series excitation of $p(0)$ states, which is plotted on the graph as a solid line according to the equation
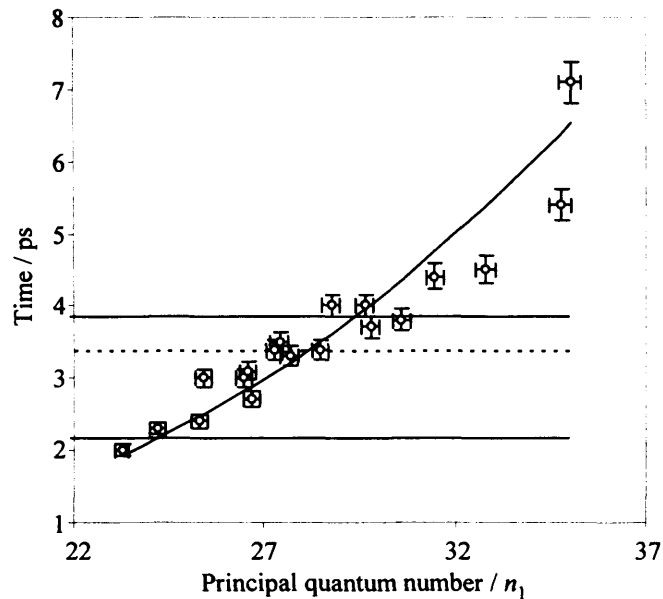
Figure.4.7. A plot of the time of the first experimentally observed peak in the dissociating wave packet spectrum as a function of the average principal quantum number n_1, obtained using spectra recorded following excitation via the $|v' = 1, N' = 1, J' = 1/2\rangle$ level of the intermediate. The curve represents the classically expected orbit period for single series excitation of $p(1)$ states, $t_{cl} = 2\pi n_1^2$. The horizontal lines represent the stroboscopic periods for interference between $p(1)$ and $f(3)$ series (solid) and for the $p(1)$ and $p(3)$ series (dashed) calculated using equation 4.1.

$t_{cl} = 2\pi n_0^3$. The horizontal lines represent the stroboscopic periods for interference between $p(0)$ and $f(2)$ series (solid) and for the $p(0)$ and $p(2)$ series (dashed) calculated using equation 4.1. We do not consider the effect of interference between the $p(2)$ and $f(2)$ series, as the $p(0)$ series is by far the most intense series. There is some scatter of the measured recurrence times and evidence of very weak plateaus at the stroboscopic periods, indicating that there may be a very weak contribution to the wave packet dynamics from

the $f(2)$ series. Figure. 4.7. represents a similar plot of the time of the first experimentally observed peak in the recurrence spectrum as a function of the average principal quantum number following excitation via the $|N' = 1, v' = 1, J' = 1/2\rangle$ level of the A-state. Again the recurrences generally follow the hydrogenic line, this time for excitation of a single $p(1)$ Rydberg series with $t_{cl} = 2\pi n_1^3$. As before, the horizontal lines represent the stroboscopic periods: for interference between $p(1)$ and $f(3)$ series (solid) and for the $p(1)$ and $p(3)$ series (dashed) calculated using equation 4.1. In this case there are more distinct clusters around the stroboscopic periods associated with the $p(1)$ and $f(3)$ with $k = 1$ and 2 (at 2.3 ps and 3.8 ps respectively) and with the $p(1)$ and $p(3)$ series with $k = 1$ (at 3.4 ps). These are similar, but considerably less distinct than the plateaus seen in the autoionising work of the Fielding group [1-4], due to the relatively weak population of the $p(3)$ and $f(3)$ series in the predissociation spectrum when compared with the $p(0)$ series. From these plots it is estimated that the predisssociating wave packet contains $>90\%$ $p(N')$ character irrespective of the excitation intermediate.

4.5.2 Controlling the dissociation/ionisation ratio

The origin of the plateaus seen in the autoionising wave packet spectra is the phase evolution that is inherent in the Rydberg molecule. The optical Ramsey method employed to observe the wave packet dynamics, is based on interferences between oscillations in the Rydberg population induced by the optical field. In this section we show how it is possible to exploit the internal phase of the Rydberg molecule together with the optical phase inherent in the optical Ramsey method to control the composition of the wave packet,

therefore controlling the relative ionisation:dissociation ratio. A frequency spectrum of the autoionising Rydberg states of NO is recorded following excitation via the $\left|v' = 1, N' = 0, J' = 1/2\right\rangle$ level of the A-state. A portion of the spectrum is plotted over the range $23 < n_0 < 36$ and the dominant $p(0)$ and $f(2)$ series are labeled in figure. 4.8.
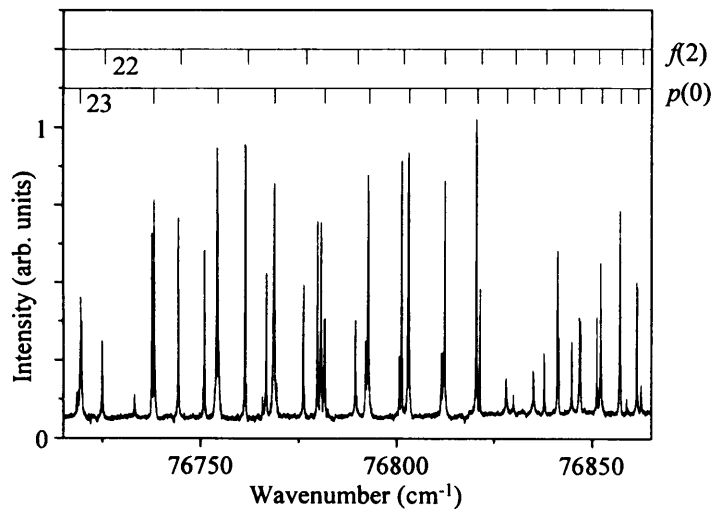
Figure.4.8. *Part of the Rydberg spectrum excited via* $\left|v' = 1, N' = 0, J' = 1/2\right\rangle$ *level of the A-state. The two main series excited are labeled with combs. The wavenumber gives the energy of the Rydberg state from the ground* $^2\Pi_{1/2}$ *state.*

The $p(0)$ and $f(2)$ series can be separated from the whole frequency spectrum and then treated separately in all subsequent discussions and calculations. The experimental excitation energies, ω, and intensities, $a_i^2(\omega)$, can be used to calculate the optically induced interference fringes in the two separate Rydberg series, i, and to determine their relative phase. To do this the spectrum is convoluted with a Gaussian of full width half maximum (FWHM) 14 cm^{-1} equivalent to the laser pulse used in the experiments. The

time-dependent interference term in the Rydberg population, $A_i^2(t)$, of each Rydberg

series, i, is calculated around the average time of the first recurrence, $t = (t_{cl}^p + t_{cl}^f)/2 = t_{cl}^{Av}$,

using

$$A_i^2(t) = \text{Re}\left[\sum_\omega a_i^2 \exp(-2\ln 2(\omega - \omega_L)^2 / \sigma^2) \exp(-i\omega t) \right].$$ (4.2)

where σ is the FWHM of the laser pulse and ω_L is the average excitation energy of the

laser pulse.
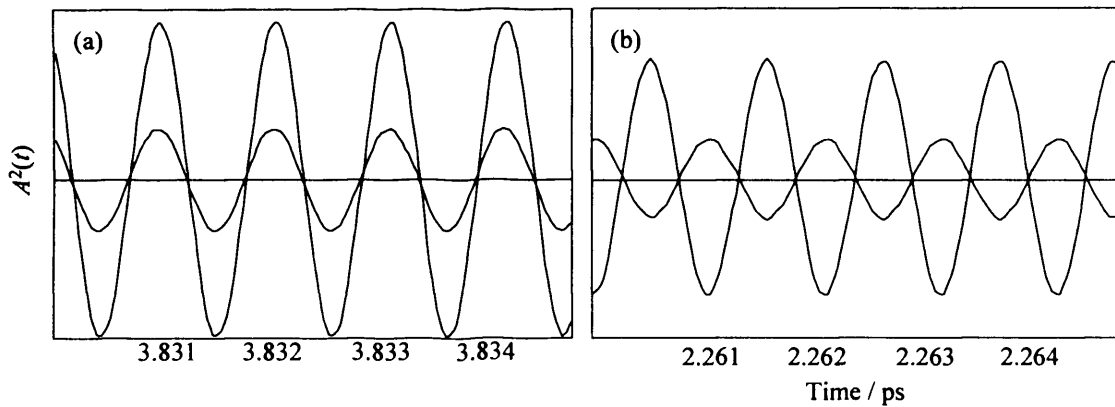
Figure.4.9. *Time dependent interference terms of the Rydberg populations calculated using equation (4.2). Calculated around the time of the average first recurrence for the two series at a) $n_0 = 30$ and b) $n_0 = 25$. In both plots the larger amplitude fringes represent the p series while the lower amplitude series represent the f series.*

The phase-dependent interference terms, $A_i^2(t)$, for a wave packet excited around $n_0 = 30$

(a) and 25 (b) are plotted in figure 4.9. In each of these plots, the larger amplitude

oscillation represents the interference fringes of the p Rydberg population, whilst the lower

amplitude oscillation, represents the interference fringes of the f population. For excitation

around $n_0 = 30$, the interference fringes of the two angular momentum components after one orbit period, $t = t_{cl}$, are in phase with one another. This is understood by noting that $n_0 = 30$ lies in the middle of the $k = 2$ stroboscopic plateau, observed in earlier work [1-4]. In contrast, for excitation around $n_0 = 25$, the Ramsey fringes of the two angular momentum components are out of phase with one another after one orbit period. This is also readily understood from earlier work [1-4]: $n_0 = 25$ lies midway between the $k = 1$ and $k = 2$ stroboscopic plateaus.

The evolution of the phase difference with excitation energy, manifests itself in the amplitude of the Ramsey fringes in the *total* Rydberg population. The first wave packet is excited and allowed to evolve for one classical period t_{cl}. During this time, it acquires a phase difference between the two angular momentum components, ϕ_M. At $t = t_{cl}$, the second wave packet is launched and allowed to interfere with the first. The angular momentum components within the second wave packet are in phase with one another at the moment of its creation. If $\phi_M = 0$, the amplitude of the Ramsey fringes in the total Rydberg population will obviously be larger than if $\phi_M = \pi$. This effect is illustrated in the inset of figure. 4.10. Ramsey fringes recorded around the time of the first recurrence in the autoionising wave packet spectrum are plotted for excitation around (a) $n_0 = 25.1$ ($\phi_M \approx \pi$) and (b) $n_0 = 29.6$ ($\phi_M \approx 0$) under identical experimental conditions. The amplitude of the fringes in (b) is significantly larger than those in (a). In contrast, the amplitude of equivalent sets of fringes recorded around the time of the first recurrence in the predissociating wave packet spectrum changes less dramatically with phase.

It is now possible to exploit this phase evolution to control the ratio of autoionisation to predissociation in an intuitive way. At $n = 25$, where $\phi_M = \pi$, the p and f components are out of phase with each other after one orbit period. The amplitude of the autoionising Ramsey fringes is therefore $\left(\pm\{A_p - A_f\}+\{A_p + A_f\}\right)^2 = 4A_p^2$ or $4A_f^2$, where A_l is the fringe amplitude for an individual l component of the wave packet. The first set of curly brackets refers to the first wave packet, which has evolved for one classical orbit period, and the second set refers to the second wave packet, which is created at $t = t_{cl}$. The $\pm$ depends on whether the interference induced by the second laser pulse is in phase with the p component of the initial wave packet (+) or with the f component of the initial wavepacktet (-). The predissociating Ramsey fringes have an amplitude of $\left(\{A_p\}+\{A_p\}\right)^2 = 4A_p^2$, assuming the f Rydberg states have negligible contribution. At $n = 30$, where $\phi_M = 0$, the p and f components are in phase with each other and the amplitude of the autoionising fringes is now $\left(\{A_p + A_f\}+\{A_p + A_f\}\right)^2 = 4A_p^2 + 4A_f^2$ (assuming no cross terms) whilst the amplitude of the predissociating fringes remains $4A_p^2$. Thus, the ratio of the amplitudes of the observed Ramsey fringes in the predissociating and autoionising wave packet spectra, at the time of the first recurrence, varies as a function of the phase-difference between the dominant angular momentum components at this time. This is illustrated in figure. 4.10. The phase difference between the $p(0)$ and $f(2)$ series at $t = t_{cl}$, is plotted as a function of the average principal quantum number n_0 (filled circles). It is determined directly from the experimental frequency spectrum, using equation 4.2 to calculate the Ramsey fringes of the separate angular momentum components. The phase

difference oscillates between 0 and π, passing through a minimum around $n_0 = 30$. On the same graph, we plot the ratio of the experimentally recorded Ramsey fringes in the dissociating and autoionising Rydberg spectra, at the time of the first recurrence (hollow circles). The actual value on this scale (right hand vertical axis) is arbitrary since the NO^+ ion signal recorded for an autoionising wave packet spectrum is orders of magnitude larger than the N^+ ion signal recorded for a dissociating wave packet spectrum. However, all the data contributing to figure. 4.10. were recorded using consistent experimental conditions. What is important is the variation in the ratio of the dissociating and ionising fringe amplitudes with excitation energy.
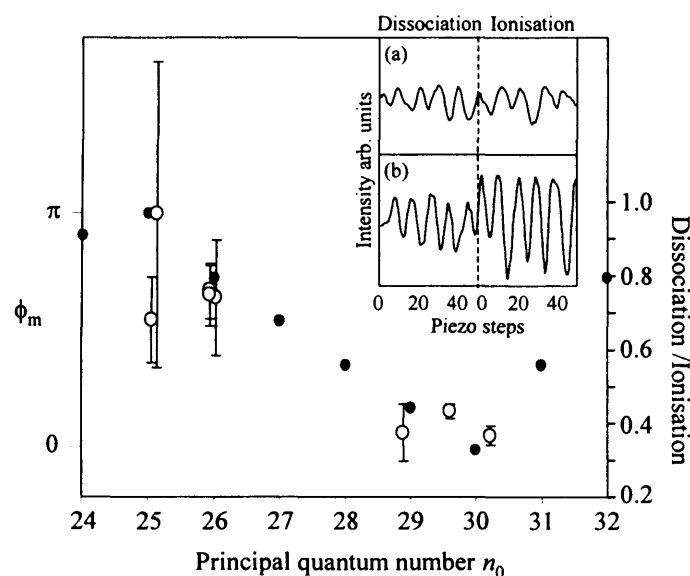
Figure.4.10. A plot of the phase difference between the $p(0)$ and $f(2)$ series at $t = t_{cl}$, as a function of average principal quantum number n_0 (filled circles). Together with a plot of the ratio of the experimentally recorded Ramsey fringes in the dissociating and autoionising Rydberg spectra, at the time of the first recurrence (hollow circles). The inset compares representative sets of Ramsey fringes from dissociating and autoionising spectra recorded at $n_0 = 25.1$ (a) and 29.6 (b). Ramsey fringes were collected over 50 piezo steps, each corresponding to 0.15 fs. The error bars for the calculated phase differences are smaller than the spot size.

Representative pairs of Ramsey fringes are plotted in the inset. The dissociation/ionisation ratios were measured at excitation energies around $n_0 = 25$, where $\phi_M = \pi$ and around $n_0 = 30$ where $\phi_M = 0$. Although there is scatter in the data, it is quite clear that there is a correlation between the phase, ϕ_M, and the dissociation/ionisation ratio. It is difficult to give an explicit form for the relationship without quantitative knowledge of all the other decay routes available to the wave packet, e.g. NO may also dissociate to form ground state nitrogen and oxygen. Thus, although we are building up a picture of the total wave packet other pathways still need investigating.

4.6. Summary

The work presented represents the first observation of a dissociating Rydberg electron wave packet in a molecule. To detect the dynamics we employed a three-colour REMPI technique combined with the optical Ramsey method. Overall, the dynamics are hydrogenic, since the dissociating wave packet is composed predominantly of a single $p(N')$ Rydberg series. This is in contrast with autoionising electron wave packets in NO. The autoionising wave packets have already been shown to exhibit interesting interference effects due to the fact that they are composed of almost equal proportions of $p(N')$ and $f(N' + 2)$ Rydberg states. Not only is this investigation of predissociating electron wave packet dynamics interesting in its own right, it also allows us to build a more complete picture of the dynamics of an electron wave packet in NO. Other channels do however still

need investigating, for example dissociation can also proceed to give ground state $N(^4S)$ and $O(^3P)$. Having an understanding of how the electron wave packet behaves in more than one channel, and of the influence of the intrinsic phase of the system on the dynamics in the different channels, allows us to design intuitive control schemes to select one decay route rather than another. We have demonstrated an intuitive control scheme for manipulating the ionisation/dissociation branching ratio in NO that exploits the relative ionisation and dissociation rates of the different angular momentum states in the superposition, and the relative phase evolution of the different angular momentum components of the electron wave packet. Although the control is rather crude, the mechanism is extremely simple and predictable, and demonstrates the viability of using coherent control schemes in Rydberg molecules to control a photoinitiated decay route.

4.7 References

1   R. A. L. Smith, V. G. Stavros, J. R. R. Verlet, H. H. Fielding, D. Townsend, and T. P. Softley, Journal of Chemical Physics **119** (6), 3085 (2003).

2   R. A. L. Smith, J. R. R. Verlet, E. D. Boleat, V. G. Stavros, and H. H. Fielding, Faraday Discussions (115), 63 (2000).

3   V. G. Stavros, J. A. Ramswell, R. A. L. Smith, J. R. R. Verlet, J. Lei, and H. H. Fielding, Physical Review Letters **83** (13), 2552 (1999).

4   V. G. Stavros, J. A. Ramswell, R. A. L. Smith, J. R. R. Verlet, J. Lei, and H. H. Fielding, Physical Review Letters **84** (8), 1847 (2000).

5   J. A. Fiss, L. C. Zhu, R. J. Gordon, and T. Seideman, Physical Review Letters **82** (1), 65 (1999).

6   J. A. Fiss, A. Khachatrian, L. C. Zhu, R. J. Gordon, and T. Seideman, Faraday Discussions (113), 61 (1999).

7   R. J. Gordon, L. C. Zhu, and T. Seideman, Journal of Physical Chemistry A **105** (18), 4387 (2001).

8   J. A. Fiss, L. C. Zhu, K. Suto, G. Z. He, and R. J. Gordon, Chemical Physics **233** (2-3), 335 (1998).

9   L. Zhu, K. Suto, J. A. Fiss, R. Wada, T. Seideman, and R. J. Gordon, Physical Review Letters **79** (21), 4108 (1997).

10   L. C. Zhu, V. Kleiman, X. N. Li, S. P. Lu, K. Trentelman, and R. J. Gordon, Science **270** (5233), 77 (1995).

11   S. P. Lu, S. M. Park, Y. G. Xie, and R. J. Gordon, Journal of Chemical Physics **96** (9), 6613 (1992).

12   R. W. Field, R. A. Gottscho, and E. Miescher, Journal of Molecular Spectroscopy **58** (3), 394 (1975).

13   A. Giustisuzor and C. Jungen, Journal of Chemical Physics **80** (3), 986 (1984).

14   I. Rabadan and J. Tennyson, Journal of Physics B-Atomic Molecular and Optical Physics **29** (16), 3747 (1996).

15   I. Rabadan and J. Tennyson, Journal of Physics B-Atomic Molecular and Optical Physics **30** (8), 1975 (1997).

16   M. Raoult, Journal of Chemical Physics **87** (8), 4736 (1987).

17   A. Fujii and N. Morita, Chemical Physics Letters **182** (3-4), 304 (1991).

18   A. Fujii and N. Morita, Journal of Chemical Physics **97** (1), 327 (1992).

19   A. Fujii and N. Morita, Laser Chemistry **13** (3-4), 259 (1994).

20   A. Fujii and N. Morita, Journal of Chemical Physics **98** (6), 4581 (1993).

21   A. Fujii and N. Morita, Journal of Chemical Physics **103** (14), 6029 (1995).

22   L. E. Jusinski, G. E. Gadd, G. Black, and T. G. Slanger, Journal of Chemical Physics **90** (8), 4282 (1989).

23   H. Umemoto and K. Matsumoto, Journal of the Chemical Society-Faraday Transactions **92** (8), 1315 (1996).

24   E. Miescher, Canadian Journal of Physics **54** (20), 2074 (1976).

25   Y. Anezaki, T. Ebata, N. Mikami, and M. Ito, Chemical Physics **89** (1), 103 (1984).

26   Y. Anezaki, T. Ebata, N. Mikami, and M. Ito, Chemical Physics **97** (1), 153 (1985).

27   J. R. R. V. R.A.L. Smith, R.S. Minns, V.G. Stavros and H.H. Fielding, Unpublished (2003).

28   L. D. Noordam, D. I. Duncan, and T. F. Gallagher, Physical Review A **45** (7), 4734 (1992).

29   M. Godefroid and C. F. Fischer, Journal of Physics B-Atomic Molecular and Optical Physics **17** (5), 681 (1984).

Chapter 5: Global MQDT representation of the NO molecule

5.1 Introduction

Multichannel quantum defect theory (MQDT) has proved extremely effective in explaining and predicting the structure of Rydberg series in atoms and molecules (see for example [1,2] and references therein). Entire Rydberg series can be accurately described with only a handful of parameters, which can be derived from experimental observations. Is it possible however, to describe accurately all the Rydberg series of a molecule by a single quantum defect matrix? Previous comprehensive treatments of atomic systems have proved successful, but these systems lack the complexities added by a rotating and vibrating core. By building a global representation of the Rydberg states of NO, including all series interactions, and eventually the valence (core excited) states, we aim to have a comprehensive understanding of the entire Rydberg spectrum of NO. The extension of MQDT to molecular systems [3-7] follows a similar derivation as that for atoms. Again two regions of interaction space are set-up; a collision region, where the electron sees the complex potential of the core electrons and nuclei, and the asymptotic region where the Rydberg electron only sees the resultant Coulomb potential of the core. In the asymptotic region the radial motion of the electron can be described as a linear combination of regular and irregular Coulomb waves. The amount of

irregular character is controlled by the interaction of the Rydberg electron with the core in the collision region. This formulation is so far identical to the atomic formulation of MQDT; however, the electron will see different core states depending on the exact internuclear distance at the time of collision. The internuclear distance will affect the amount of irregular character in the wavefunction and therefore the quantum defect. The quantum defect is therefore a function of internuclear distance, R. The electron-ion collision takes place extremely quickly due to the large speeds achieved as the Rydberg electron is accelerated back to the core, and the electron, therefore, sees a fixed internuclear distance for the period of interaction. For each internuclear distance, a separate quantum defect can be calculated, so instead of having one quantum defect we now have a set of quantum defects; one for each R position, and we have essentially used the Born-Oppenheimer approximation to separate nuclear and electronic motion. This formulation by Ross and Jungen [4,5,8] is the basis of the work presented here. All relevant equations will be given in section 5.2 as well as a description of how series interactions are introduced and vibronic energy levels calculated.

A unified representation should make it possible to design future coherent control experiments, as well as helping to explain the finer details of molecular wave packet dynamics in the bound, autoionising and dissociating states of NO. Knowledge of the weaker interactions may also help explain the observation of rotational autoionisation of NO by the Zare group [9-12]. In the experiments of the Zare group the partial wave character of outgoing photoelectrons did not match that predicted by angular momentum selection rules. For example, ionisation from the $3s\sigma$ state, which has 94% s character, 5% d character and smaller contributions from odd angular momentum states, produced a photoelectron of 70% p character, 21% f character and 9% s and d character. This may seem reasonable, however, the s and d contribution is

an order of magnitude larger than expected by angular momentum arguments alone. Gilbert and Child suggested l mixing could be a possible cause for this discrepancy. By modelling the entire Rydberg series, it should be possible to see which interactions are most important and why these discrepancies occur. Previous MQDT studies of the NO molecule have concentrated on small energy ranges or individual series contained within the Rydberg spectrum of NO, for example, extensive studies of the f states have been carried out by a number of authors [13-15], while a large study of the s-d super-complexes has been undertaken by Fredin et al [16]. Initial attempts to model the s and d series individually failed to predict the observed structure and this is due to the large coupling between the sigma components of the two series.

5.2 Methodology

In this work, the f and h Coulomb functions and associated η defects have been used instead of the more common f and g Coulomb functions and associated μ defect. This choice is made as it removes unphysical energy levels with $\ell > n$, which are allowed when using the more common basis set [1]. In a one-channel problem (a channel is defined as all the bound and continuum states that belong to a particular core + electron configuration) we saw in section 1.2.1 how an atomic Rydberg wavefunction can be written as a linear combination of regular and irregular Coulomb waves, with the irregular component being due to the interaction of the Rydberg electron with the remaining ion core. The same applies to molecular systems and equation 5.1 gives an example of such a Rydberg wavefunction for a molecule.

$$\Psi(\theta,l,R,r) = \Psi(\theta,R)\{f_l(R) + \tan[\pi\eta(R)]h_l(R)\}$$ (5.1)

θ represents all degrees of freedom except the radial position of the Rydberg electron, r, and the internuclear distance, R, f and h are the regular and irregular Coulomb functions. As the effect the core has on the electron depends on its geometry, the quantum defect is a function of the internuclear distance; this is essentially the only difference between equation 5.1 and equation 1.6. By looking at the asymptotic forms of the Coulomb waves and imposing the bound state boundary condition, that is $r \rightarrow \infty, \Psi \rightarrow 0$, eigenenergies occur when,

$$\left| \tan[\pi\eta(R)] - \frac{\tan[\pi\nu(R)]}{A_i(\nu(R))} \right| = 0 \tag{5.2}$$

where A is Ham's scaling function [3], which is introduced as the η defect is used instead of the more common μ defect, and has the form,

$$A_i(\nu, R) = \prod_{j=0}^{l} \left[1 - \frac{j^2}{\nu^2} \right] \tag{5.3}$$

and ν is the effective principle quantum number and is given by,

$$\nu(R) = \left[-\frac{1}{2\varepsilon(R)} \right]^{1/2} \tag{5.4}$$

In equation 5.4, $\varepsilon(R)$ is the energy of the Rydberg electron (for bound states this is negative), and is related to the ion core energy, $E^+(R)$, and the total energy, E, by,

$$\varepsilon(R) = E(R) - E^+(R) \tag{5.5}$$

If the ion state potential curve and η defect are known for a range of R, electronic potential curves for the Rydberg states can be obtained in the following way. For a particular value of R the total energy of the system is scanned. For each energy value, v and A are calculated from equation 5.4 and 5.3 respectively, and equation 5.2 is evaluated. If the expression is equal to zero then the trial energy is an eigenenergy of the molecule at that internuclear distance. This process can then be repeated over a suitable grid of R-values. The eigenenergies can then be splined together to give the potential energy curves of the molecule. By solving the problem at particular geometries, we have effectively clamped the nuclei for the time the Rydberg electron is in the core region. This is the Born-Oppenheimer approximation and is valid as the electron-ion collision is extremely rapid. As the energy is not specified until the final step, the wavefunction is valid for the entire Rydberg series and its associated continuum.

The wave packets discussed in chapters 3 and 4, contained more than one Rydberg series, so this derivation must be generalised for many channels. Each channel, i, will now have its own basis function which is again a superposition of regular and irregular Coulomb waves,

$$\Psi_i = f_i(r)|i\rangle + \sum_j \{\tan[\pi\eta_{ij}(R)]\}h_j(r)|j\rangle$$

$$= f_i(r)|i\rangle + \sum_j K_{ij}(R)h_j(r)|j\rangle \tag{5.6}$$

the kets represent all degrees of freedom except the radial motion of the Rydberg electron. The collision of the Rydberg electron with the ion core can lead to electronic rearrangement, and the admixture of irregular Coulomb waves, due to the interaction of the core, must now also include irregular functions from other channels. The single quantum defect used for the one channel problem, is now replaced by a reaction matrix, K_{ij}, with the off diagonal elements accounting for the interactions with other channels, where,

$$K_{ij} = \tan[\pi \eta_{ij}(R)] \tag{5.7}$$

The total wavefunction can now be written as a linear combination of the basis wavefunctions,

$$\Psi = \sum_i Z_i \Psi_i \tag{5.8}$$

The bound state boundary condition now requires,

$$\left| K + \frac{\tan[\pi \nu]}{A(\nu)} \right| = 0 \tag{5.9}$$

where K is defined in equation 5.7 and has replaced $\tan[\pi \eta]$ from equation 5.2. $\tan[\pi \nu]$ and $A(\nu)$ are the diagonal matrix elements ,

$$[\tan(\pi v)]_{ij} = \delta_{ij} \tan(\pi v)_i$$
$$[A(v)]_{ij} = \delta_{ij} [A(v)]_i$$

(5.10)

where δ_{ij} is a Kronecker delta function. Then, as in the single channel problem, if the quantum defect matrix $\eta_{ij}(R)$ and ion state potential are known, then the Born-Oppenheimer potential curves can be obtained, including all series interactions. The strong interactions of the first few excited states of H_2 have been studied using this method [4,5]. The strong interactions lead to avoided crossings and double minimum potentials in the first few excited states of H_2. Even in this complex region, good agreement between experiment and the corresponding MQDT calculations have been achieved.

Of course electronic energy levels do not form the complete basis set for molecules; vibrational and rotational levels also need to be calculated. We must therefore calculate the full vibronic reaction matrix. The full vibronic matrix can be derived from the outset but contains around 20,000 parameters for a diatomic molecule, which is an unreasonable number of parameters to obtain or derive from the start. An alternative route to the vibronic matrix is to use the electronic reaction matrix described above and use a frame transformation to calculate the full vibronic matrix, this way a basis set of only ~40 parameters is needed. The frame transformation is achieved by considering the boundary between the collisional and asymptotic regions. In the asymptotic region, where the electron moves slowly in comparison to the nuclei, the wavefunction of the system is represented by the vibrational and rotational quantum numbers of the ion core, v^+ and N^+ respectively, and is labelled $|iv^+ N^+\rangle$, while in the collision region, where the electron moves quickly when compared with the nuclei, the

wavefunction contains the clamped nuclei quantum numbers. The internuclear distance, R, is used instead of the vibrational wavefunction as the nuclei are stationary during the collision, and the total orbital angular momentum around the molecular axis, Λ, replaces the rotational quantum number as the rotation of the core now couples the electron to the internuclear axis. The collision region wavefunction is therefore labelled $|iR\Lambda\rangle$. The relationship between the full rovibronic matrix and the electronic matrix has been derived by Jungen and Atabek [6] and has the form

$$K_{iv_i^+N_i^+,jv_j^+N_j^+} = \int dR^{JM} \left\langle iv_i^+N_i^+ \left| \left(\sum_\Lambda |iR\Lambda\rangle^{JM} K_{ij}(R)^{JM} \langle jR\Lambda| \right) \right| jv_j^+N_j^+ \right\rangle^{JM} \tag{5.11}$$

i labels the electronic state of the combined ion plus electron complex for a given total angular momentum, J, and z-axis projection, M. The system starts in the vibronic asymptotic channel $|iv^+N^+\rangle$, and the electron then enters the collision region and is best described using the clamped nuclei channels $|iR\Lambda\rangle$. The sum over Λ and the integration over R, describes how the incoming wave can be scattered into a number of collision channels. The interaction with the core causes the electron to scatter into channel $|jR\Lambda\rangle$, according to the electronic reaction matrix K_{ij}, which again is different for each R-value, and has off diagonal components that can lead to electronic rearrangement. Finally the scattered channel $|jR\Lambda\rangle$ is projected onto the asymptotic channel $|jv^+N^+\rangle$, corresponding to a particular rovibronic state of the molecule. The transition from the asymptotic to collision channel region and back again is contained withing the bra-kets of equation 5.11 and is a transformation from Hund's case d) to Hund's case b). The frame transformation requires the use of symmetrised basis

functions for both the asymptotic and collision channels, and the vibronic reaction matrix then takes account of all the interactions between different rotational, vibrational and electronic levels.

Once the rovibronic matrix has been obtained, the rovibronic energy levels can be calculated using the same procedure as before. Each channel is written as a superposition of regular and irregular Coulomb waves, and the total wavefunction is then the sum of the channel wavefunctions. As a final step the boundary conditions are imposed and the energy is calculated. The boundary conditions require that,

$$\left| K_{iv_i^+N_i^+,jv_j^+N_j^+} + \frac{\tan(\pi\nu)}{A(\nu)} \right| = 0 \tag{5.12}$$

where all terms have the same definitions as before. Again the energy can be scanned to find the rovibronic eigenenergies of the system. This derivation shows how from the electronic reaction matrix, whose values are derivable from experimental observation, entire ro-vibrational Rydberg spectra can be modelled and explained, including all vibronic interactions.

5.3. Fitting procedure and application

A non-linear least squares fit to experimental data is used to optimise the values in the quantum defect matrix. In all of the calculations the NO^+ ion state potential of Raoult [17] has been used. The experimental energy levels used are those of Miescher [25], Fredin [16], Pratt [18] and Eyler [13,19]. Although this is by no means an exhaustive basis set, it did prove sufficient to fit all parameters interrogated. The p-states with large

perturbations due to interactions with valence states have also been removed from the least squares fit, but will be reintroduced when the valence states are added to the system. The reason for removing these highly perturbed states, is that in many regions the p series is well behaved, and can be accurately modelled using the standard quantum defect parameters. The valence state interactions mask this, as they can induce large (up to 100's cm^{-1}) energy shifts on some members of the Rydberg series. Small interactions such as Λ doubling and spin-orbit splittings have been neglected, where small (< 1 cm^{-1}) spin-orbit splittings have been reported, the mid point between the two spin-orbit states has been taken as the origin.

In order to evaluate the electronic reaction matrix the ion state potential of Raoult was used, the energy levels of Raoult [17] differ from the experimentally observed levels by approximately 0.5 cm^{-1} and so were shifted to match the experimental energy levels. The p and f channels are initially treated independently, while the s and d series must be treated together, from the start, due to the strong interaction between them. Values for the η defect are initially optimised on a single vibrational state of the core. Once the η defect has converged the energy dependence of the system can also be obtained. The initial η defects and energy dependences used are obtained from Elden plots of the quantum defect against energy (in units of $1/n^2$), the quantum defect is then the y-intercept with the gradient being the energy dependence. Initially the p states were robustly fitted to separate the levels perturbed by the valence states. This procedure gives lower weightings in the fitting procedure to the outlying levels, essentially removing the perturbed levels from the fit. The perturbed states could then be removed from the rest of the calculation. Once both the quantum defect and energy dependence are stable, other vibrational states can be added and the R dependence of the quantum defect can be obtained. As the R dependence is often small

and mathematically well behaved, often the initial value can be set to zero and the least squares fit will find the absolute value. When this is not the case the calculation can be damped to stop the least squares fit running away to unreasonable numbers. Initial estimates of the quantum defects and energy dependences were calculated using the data of Miescher [25], Pratt [18] and Eyler [13,19] for the f and p series, and the data of Miescher [25] and Fredin et al [16] for the s and d series, the s-d off diagonal matrix element was also taken from Fredin et al [16]. Upon convergence all the series are combined in a large data file and the small coupling elements are interrogated. Small coupling between various series have been documented in specific regions of the Rydberg spectrum of NO. The magnitude of these deviations is small when compared to the s-d mixing or the valence states interactions, but could become significant when trying to explain the finer details of some experiments. The matrix elements associated with the small coupling have been calculated from the data of Miescher for the $s\sigma - f\sigma$ [14] and $s\sigma - p\sigma$ [20] interactions, from Biernacki, Colson and Eyler for the $f\pi - p\pi$ [19] interaction and both Pratt, Jungen and Miescher [18], and Huber et al [21] for the $f\pi - d\pi$ interaction. To the best of our knowledge no other series interactions have been documented in the literature, we therefore set these to zero, and the reaction matrix therefore contains 46 different elements to be evaluated.

5.4 Results

Using the rovibronic term values given in table 5.2 we have carried out a global least squares fit and determined 46 elements of the quantum defect matrix, $\eta_{ij}(R)$ of

equation 5.7. The quantum defect functions have been expanded as a double power

series in R and E,

$$\eta_{ij}(E,R) = \eta_{ij} + \frac{d\eta_{ij}}{dR}(R - R_X^+) + \frac{d\eta_{ij}}{dE}(E - U_{ij}^+) + \ldots$$

(5.13)

With the expansion in R centred on the equilibrium bond distance of the ion core, R_X^+,

of 2.0092 a.u. [17], and the expansion in energy, centred on the ion state potential U_{ij}^+

at R_X^+. All parameters are reported in table 5.1, which represents the main result of this

work. In table 5.2, the experimental term values are presented along with the observed

minus calculated residual errors. The average error is then presented at the bottom of

the table. An extremely good fit has been achieved with a standard error of just over 1

cm^{-1}, the error in the experimental data used is often not much better than this. In the

calculations over 5,000 energy levels are calculated covering 72 different channels with

$0 \le N^+ \le 18$ and $0 \le v^+ \le 3$. The energy range covered is from 53000-74550 cm^{-1} and

contains all energy levels from $n = 3$ up to the first ionisation limit and demonstrates the

viability of such comprehensive representations for other molecules. The inclusion of

the small couplings improves the standard error of the least squares fit by almost 0.5

cm^{-1}, thus proving that even these small interactions can provide reasonably large

perturbations in the high energy states of NO.

Comprehensive MQDT representation of the NO molecule.

	η	$\dfrac{d\eta}{dR}$	$\dfrac{d\eta}{dE}$	$\dfrac{d}{dR}\left(\dfrac{d\eta}{dE}\right)$
$s\sigma$	0.0966968545	0.00125465979	-0.0600413325	0.0542536970
$p\sigma$	0.666091709	0.269975343	-0.176445067	0.301856208
$p\pi$	0.742033039	-0.268915713	-0.0183156754	0.901174668
$s\sigma - p\sigma$	0.0000053			
$d\sigma$	0.0540774800	-0.0003586253	-0.415916839	-0.0841515633
$d\pi$	-0.0564183486	-0.000203063	-0.119703696	-0.0137897641
$d\delta$	0.0923919874	0.00742596467	-0.165909303	0.00015990976
$p\sigma - d\sigma$	0.0			
$p\pi - d\pi$	0.0			
$s\sigma - d\sigma$	0.132944978			
$f\sigma$	0.0204959522	0.00295432257	0.105740409	0.002137354
$f\pi$	0.0170649232	0.00256159179	0.0749333897	-0.0103419289
$f\delta$	0.0124581903	0.00168646624	0.04801011823	-0.008386964
$f\phi$	0.00792908	-0.0016140785	0.0648784311	0.00617457135
$d\sigma - f\sigma$	0.0			
$d\pi - f\pi$	0.001645			
$d\delta - f\delta$	0.00196			
$p\sigma - f\sigma$	0.0			
$p\pi - f\pi$	-0.0054			
$s\sigma - f\sigma$	0.00278			

Table 5.1. Quantum defect matrix elements from MQDT least squares fit to the experimental data in table 5.2. Entries of zero refer to parameters not included in the fit, as to the best of our knowledge no such couplings have been reported.

120

$T(\text{cm}^{-1})$	N^+	o - c	$T(\text{cm}^{-1})$	N^+	o - c	$T(\text{cm}^{-1})$	N^+	o - c
a) 3, 4, 5, 8, 9 and $10s\sigma$ $v = 0$								
69962.50	1	2.579						
71463.50	1	2.124						
72353.30	1	1.400						
72923.60	1	0.958						
73311.10	1	1.014						
73585.30	1	0.287						
a) 6, 7 and $8s\sigma$ $v = 0$								
71517.20	5	1.670	71540.10	6	1.045	71567.50	7	1.453
72406.30	5	1.121	72428.40	6	0.134			
72975.00	5	0.293	72996.80	6	-0.292			
71598.50	8	1.507	71632.70	9	1.037	71713.70	11	1.240
72485.50	8	0.448	72519.50	9	0.566	72598.30	11	0.623
71809.80	13	1.327						
a) $6d\sigma$ $v = 0$ and $3d\pi$ $v = 0$								
71816.70	5	-2.583	71846.10	6	-3.209	71801.80	7	-2.765
71829.30	8	-3.734	71937.60	11	-4.756	72031.20	14	-4.974
a) $6\,d\delta v = 0$								
71640.90	5	2.329	71661.60	6	0.042	71690.00	7	2.061
71720.40	8	1.016	71790.10	10	-0.209	71831.20	11	-0.756
71875.50	12	-1.955	71924.60	13	-2.221			
b) $5s\sigma$ $v = 1$								
69491.3	2	3.685	69503.1	3	3.779	69518.8	4	3.871
69538.2	5	3.777	69561.4	6	3.568	69588.9	7	3.766
69619.9	8	3.560	69655.2	9	3.762	69694.2	10	3.763
b) $6s\sigma$ $v = 1$								
72303.3	0	2.859	72306.3	1	1.987	72315.4	2	3.344
72326.8	3	3.129	72341.4	4	2.245	72360.6	5	2.092
72384.3	6	2.571	72411.1	7	2.285	72442.0	8	2.234
72476.9	9	2.323	72515.5	10	2.253			
b) $7s\sigma$ $v = 1$								
73804.3	1	2.369	73807.7	2	1.940	73815.4	3	-0.521
73827.0	4	2.097	73842.4	5	2.188	73861.3	6	1.959
73884.2	7	1.915	73910.9	8	1.860	73941.5	9	1.903
b)* $3d\sigma$ and $\pi v = 1$								
65044.0	1	-5.408	65048.1	2	-3.761	65054.9	3	-3.400
65065.6	4	-3.115	65080.1	5	-2.974	65098.6	6	-2.835
65121.0	7	-2.763	65147.4	8	-2.666	65177.7	9	-2.640
65212.0	10	-2.585	65250.3	11	-2.500	65292.5	12	-2.483

65338.6	13	-2.533	65064.1	1	-1.558	65076.9	0	-2.181
65114.8	4	-2.991	65139.6	5	-3.489	65169.5	6	-2.849
65239.3	8	-3.447	65325.1	0	-3.870	65426.7	12	-4.294
65483.4	13	-4.543	65080.3	-3	0.299	65096.3	-4	0.360
65116.2	-5	0.338	65140.2	-6	0.445	65167.3	-7	-0.343
65199.2	-8	-0.300	65234.9	-9	-0.447	65274.7	-10	-0.465

b) 4$d\sigma$ and $\pi v = 1$

70340.0	3	-0.279	70349.0	4	-2.006	70363.0	5	-2.779
70382.0	6	-2.633	70398.0	4	-0.057	70423.0	5	-0.304
70453.0	6	0.472	70404.0	7	3.301	70374.0	-4	0.338
70394.0	-5	0.263	70418.0	-6	0.176	70445.0	-7	-0.923

c) 5$d\pi v = 1$

72781.6	-3	0.024	72797.7	-4	-0.141	72818.2	-5	0.031
72842.6	-6	0.042	72871.3	-7	0.295	72903.8	-8	0.289
72940.5	-9	0.423	72981.1	-10	0.387			

c) 9$d\pi v = 1$ see 5dpi

64394.00	7	3.812	64423.40	8	1.875	64457.00	9	0.223
64494.45	10	-1.493	64535.90	11	-3.123	64581.65	12	-4.365
64631.15	13	-5.769	70755.85	2	4.528	70765.71	3	3.270
70778.96	4	1.680	70795.52	5	-0.482	70814.91	6	-3.409

b) $f\pi v = 0$ pi-

70756.26	-2	4.101	70766.77	-3	2.671	70780.87	-4	0.849
70798.22	-5	-1.700	70818.22	-6	-6.110			

b) $f\sigma v = 0$

53291.36	0	-0.868	53295.35	1	-0.831	53303.30	2	-0.787
53315.26	3	-0.686	53331.15	4	-0.606	53351.08	5	-0.742
53374.97	6	-0.564	53402.84	7	-0.591	53434.67	8	-0.374
53470.47	9	-0.136	53510.26	10	0.145	53554.03	11	0.460
53601.80	12	0.829	53653.48	13	1.165	53709.14	14	1.538

64659.10	0	2.097	4663.20	1	2.157	64671.20	2	2.078
64683.40	3	2.160	64699.60	4	2.204	64719.80	5	1.884
64744.00	6	1.852	64772.30	7	1.673	64804.40	8	1.474
64840.50	9	1.242	64880.50	10	0.881	64926.00	11	1.990
64974.10	12	1.673	65028.00	13	3.131	68915.10	6	-3.924
68943.10	7	-4.999	68829.40	0	-2.481	68833.60	1	-2.417
68841.70	3	-2.587	68854.00	3	-2.690	68870.30	4	-2.92
68890.70	5	-3.538						

70846.40	0	0.065	70850.50	1	-0.072	70858.90	2	-0.141
70871.50	3	-0.234	70888.30	4	-0.338	70909.10	5	-1.025
70932.70	6	-2.714	70965.20	7	0.209	70997.20	8	-1.369
71032.40	9	-3.869	71987.20	0	5.154	71992.15	1	5.654
71999.80	2	4.852	72013.50	3	4.833	72053.30	5	4.677

71070.20	10	-7.871						

73143.50	0	3.589	73148.00	1	2.832	73157.20	2	1.850
73171.40	3	1.299	73190.80	4	1.625	73213.70	5	0.785
73240.50	6	0.216	73713.40	2	0.335	73728.30	3	0.175
73747.70	4	0.254	73771.00	5	-0.431	73798.20	6	-0.726
73829.60	7	-0.920						

b) $f\pi\,v = 0$

52373.16	1	-0.643	52380.92	2	-0.977	68733.30	6	4.696
68756.40	7	0.669	68782.30	8	-4.030			

b) $3p\sigma\,v = 1$

55570.62	0	-0.747	55574.6	1	-0.683	55582.4	2	-0.713
55594.2	3	-0.659	55610.0	4	-0.519	55629.7	5	-0.398
55653.3	6	-0.286	55680.9	7	-0.091	55712.4	8	0.095
55747.8	9	0.271	55786.96	10	0.295			

b) $4p\sigma\,v = 1$

67013.4	4	-3.715	67034.2	5	-2.966	67058.2	6	-3.024
67086.1	7	-3.188	67118.2	8	-3.157	67154.1	9	-3.328

b) 6p,v=1

73200.5	2	3.727	73231.1	4	4.756	73252.3	5	5.683
73278.2	6	5.246	73307.2	7	6.793			

b) $8p\sigma\,v = 2$

73360.4	3	-1.836	73378.1	4	0.879	73400.6	5	-2.694
73427.0	6	3.831						

b) $4,6,8f\,v = 0$ $L = +3$

67823.90	3	0.853	67828.00	4	1.434	67835.40	5	1.188
71660.40	3	0.267	71663.80	4	0.286	71671.30	5	0.132
73001.40	3	0.153	73005.10	4	0.236	73012.50	5	-0.061
67847.30	6	1.389	67862.90	7	1.258	73060.10	8	-0.005
71742.50	9	-0.178	71683.10	6	0.177	71699.20	7	0.455
73083.30	9	-0.512	73024.50	6	0.096	73040.40	7	0.151
73111.50	10	-0.654	71802.10	11	-0.166	71837.70	12	-0.308
71877.50	13	-0.222	73144.60	11	0.649			

b) $4,6,8f\,v = 0$ $L = +2$

67840.20	-3	0.957	71676.00	-4	0.389	67858.50	-5	1.310
73014.80	-4	0.242	71687.70	-5	0.585	73026.50	-5	0.191
67873.50	-6	0.865	71722.40	-7	-0.057	71746.50	-8	-0.224
71774.40	-9	-0.065	71702.70	-6	-0.058	73061.40	-7	-0.341
73085.50	-8	-0.609	71806.20	-10	-0.018			

b) $4,6,8f\,v = 0$ $L = +1$

67825.00	2	1.187	73014.80	3	0.561	67863.30	4	0.919

| 71662.60 | 12 | 0.441 | 67878.30 | 5 | 0.574 | | | |

b) 4,6,8f v = 0   L = -1

71668.90	1	0.180	71684.40	2	0.406	71701.00	2	0.023
73011.60	2	0.188	73024.70	2	-0.114	73041.00	3	-0.148
71721.40	4	0.065	67917.90	5	0.215	67946.20	6	0.380
67978.80	7	0.979	73061.30	4	0.048	71745.70	5	-0.294
71773.40	6	-0.575	73086.00	5	0.235	73113.40	6	-0.268
68014.20	8	0.516	71841.10	8	-0.731			

b) 4,6,8f v = 0   L = -2

67843.10	-1	-0.379	67864.50	-2	1.248	67886.80	-3	1.315
71682.10	-1	0.263	71698.90	-2	-0.094	71719.40	-3	-0.081
73024.00	-1	0.114	73040.20	-2	-0.112	73060.40	-3	0.093
67911.70	-4	0.806	67940.10	-5	0.797	67972.20	-6	0.734
68008.40	-7	0.960	71743.50	-4	-0.723	71771.60	-5	-0.663
71803.60	-6	-0.579	71838.90	-7	-0.996	73084.40	-4	-0.711
73112.50	-5	-0.510	73144.30	-6	-0.570	73180.20	-7	-0.488
68048.70	-8	1.410	68092.30	-9	1.264	68140.20	-10	1.507
68191.90	-11	1.635	71878.90	-8	1.432			

b) 4,6,8f v = 0   L = -3

67838.40	0	0.389	67857.60	1	1.159	67879.40	2	1.915
71696.60	1	0.370	71716.60	2	0.182	73039.20	1	0.023
73058.90	2	-0.304	67903.90	3	1.416	67932.00	4	1.407
67963.90	6	1.423	67999.90	6	1.757	71740.90	3	-0.789
71768.80	4	-0.618	71800.70	5	-0.579	71836.40	6	-0.707
73083.40	3	-0.400	73111.20	6	-0.448	73143.00	5	2.411
73179.00	6	3.951	68039.90	7	-0.848	68183.30	10	1.092
68239.50	11	2.263						

b) 4f v = 1 L = 3, 2, 1, 0, -1, -2, -3

70167.3	3	-0.522	70170.8	4	-0.518	70178.5	5	-0.411
70190.1	6	-0.430	70205.7	7	-0.442	70225.4	8	-0.325
70248.8	9	-0.469	70276.2	10	-0.567	70307.8	11	-0.413
70183.7	-3	-0.209	70190.5	4	-0.100	70201.6	5	-0.131
70217.0	-6	-0.034	70236.4	-7	-0.004	70259.6	8	-0.192
70287.1	9	-0.070	70318.4	-10	-0.120	70167.9	2	-0.683
70196.0	3	-0.251	70206.8	4	-0.163	70221.9	5	-0.251
70241.4	6	-0.089	70264.8	7	-0.072	70292.1	8	-0.155
70323.5	9	-0.113	70358.7	10	-0.234	70398.1	11	-0.108
70440.9	12	-0.528	70488.2	13	-0.389	70539.2	14	-0.487
70182.5	-2	-0.304	70222.2	-4	0.225	70242.1	-5	-0.063
70265.8	-6	-0.006	70293.5	-7	0.122	70324.9	-8	0.019
70360.3	-9	-0.015	70399.8	-10	0.119	70442.7	-11	-0.276
70490.2	-12	-0.001	70541.1	-13	-0.254	70597.0	-14	0.568
70194.8	2	0.244	70216.3	3	-0.039			
70237.2	4	0.050	70261.3	5	-0.048	70289.4	6	0.136

70321.0	7	-0.002	70356.6	8	-0.007	70396.1	9	-0.004
70439.5	10	0.003	70486.9	11	0.104	70537.7	12	-0.303
70592.6	13	-0.516	70652.1	14	-0.025	70207.7	-2	-0.015
70229.9	-3	0.087	70254.4	-4	-0.135	70282.7	-5	-0.042
70314.6	-6	-0.065	70350.2	-7	-0.198	70389.8	-8	-0.184
70433.0	9	-0.451	70480.4	10	-0.406	70530.9	10	-1.160
70582.9	-12	-4.317	70200.5	1	-0.503	70221.3	2	-0.600
70245.8	3	-0.412	70273.8	4	-0.345	70305.7	5	-0.127
70341.1	6	-0.188	70380.6	7	0.173	70471.3	9	-3.214
70522.7	10	-1.601	70578.4	11	-0.654	70636.8	12	-1.134

b) $5fv = 1$ $L = 3, 2, 1, 0, -1, -2, -3$

72660.4	4	-1.772	72668.1	5	2.890	72679.7	6	2.891
72695.8	7	3.386	72685.4	-5	1.749	72700.4	-6	1.386
72658.0	2	2.284	72669.6	-2	1.947	72664.0	1	2.397
72681.3	2	2.424	72742.0	5	0.714	72769.5	6	0.378
72801.4	7	0.596	72836.8	8	0.437	72876.6	9	0.794
72676.2	-1	0.967	72693.8	-2	0.420	72714.3	-3	0.681
72738.3	-4	0.193	72766.1	-5	0.049	72797.9	-6	0.092
72833.2	-7	-0.223	72873.0	-8	0.084	72916.3	-9	0.006
72963.5	-10	-0.049	72689.7	1	0.869	72709.9	2	0.676
72733.4	3	0.223	72761.4	4	0.687	72793.0	5	-1.501
72828.6	6	-0.240	72867.9	7	-0.230	72958.0	9	-0.678
73009.4	10	-0.452						

b) $6fv = 1$ $L = 3, 2, 1, 0, -1, -2, -3$

74004.1	3	-0.444	74007.4	6	-0.491	74014.9	5	-0.569
74026.6	6	-0.511	74042.8	7	0.024	74061.7	8	-1.107
74085.4	9	-0.353	74112.7	10	-0.615	74144.2	11	-0.586
74179.8	12	-0.390	74219.1	13	-0.430	74262.3	14	-0.505
74012.5	-3	-0.365	74019.4	-4	-0.539	74030.8	-5	-0.528
74046.2	-6	-0.615	74066.0	-7	-0.324	74064.9	4	-0.308
74088.7	5	-0.406	74116.3	6	-0.528	74148.4	7	-0.468
74062.7	-3	-0.639	74086.1	-4	-1.217	74114.6	-5	-0.497
74146.3	-6	-0.417	74181.6	-7	-0.517	74221.4	-8	-1.167
74021.2	0	-2.149	74039.0	1	-1.266	74059.9	2	-0.377
74083.8	3	0.862	74111.4	4	0.459	74143.1	5	-0.701
74178.5	6	-0.790						

Table 5.2.   *Experimental term values taken from a)[16], b)[25] and c)[13,18,19] used in the least squares fit to obtain the MQDT quantum defect matrix given in table 5.1. Rotational quantum numbers are also given, where negative values are listed these states are of (-) Kronig symmetry. Observed minus calculated residual errors are given from the comparison of the experimental energies with the final results of the MQDT calculation, and * notes the values are averaged over the spin orbit splitting of approximately 1 cm^{-1}*

5.5 Summary

This work represents the most complete MQDT description of NO to date, simplifications have been made to allow for such a global representation, many of simplifications can be removed in future work. The main simplification made, is that large perturbations due to valence state interaction have so far been left out of the fit. It is possible to include these states as the low-lying Rydberg states of excited ion cores. Hiyama and Child combined R-matrix and MQDT methodologies to build Rydberg states based on both $^2\Pi$ and $^2\Delta$ cores [22,23], and this allows the interactions between the valence and Rydberg states of NO to be studied in a unified way. The calculations reproduced the main properties of the interaction, but contained a systematic error of approximately 15,000 cm^{-1} between the calculated and actual positions of the valence states. The valence states could be included in a similar way in our calculations, i.e. the low lying Rydberg states of core excited states, with the exact position, shifted up or down in energy to reproduce the experimental observations. The other important factor so far neglected is the ionisation continuum; this will of course become important when considering competing ionisation/dissociation processes.

We have however included the electronic interactions between the various series based on the $^1\Sigma^+$ core. The s-d mixing is extremely strong, similar to N$_2$ [24] with weaker interaction showing local importance and altering indirectly other channels. For example the p states affect the position of the d states, despite no direct interaction, due to the s-p and s-d interactions. We have also included all vibrational and rotational interactions and have achieved a global representation of the Rydberg states of NO with a standard error of ~1 cm^{-1}. As well as evaluating the small couplings in NO for the first time, this work should stand as a good base for future work on the autoionising and

dissociating states of NO, as well as providing insight into some already observed

phenomena.

5.6. References

1   M. J. Seaton, Reports on Progress in Physics **46** (2), 167 (1983).

2   C. H. Greene and C. Jungen, Advances in Atomic and Molecular Physics **21**, 51

     (1985).

3   C. Jungen, *Molecular applications of quantum defect theory*. (Institute of

     Physics, 1996).

4   S. C. Ross and C. Jungen, Physical Review A **49** (6), 4353 (1994).

5   S. C. Ross and C. Jungen, Physical Review A **49** (6), 4364 (1994).

6   C. Jungen and O. Atabek, Journal of Chemical Physics **66**, 5584 (1977).

7   U. Fano, Physical Review A **2**, 353 (1970).

8   C. Jungen, Physical Review Letters **53** (25), 2394 (1984).

9   H. Park and R. N. Zare, Journal of Chemical Physics **104** (12), 4568 (1996).

10   H. Park and R. N. Zare, Journal of Chemical Physics **106** (6), 2239 (1997).

11   H. Park, I. Konen, and R. N. Zare, Physical Review Letters **84** (17), 3819

     (2000).

12   H. Park and R. N. Zare, Journal of Chemical Physics **104** (12), 4554 (1996).

13   D. T. Biernacki, S. D. Colson, and E. E. Eyler, Journal of Chemical Physics **89**

     (5), 2599 (1988).

14   E. Miescher, Canadian Journal of Physics **54** (20), 2074 (1976).

15   D. Uy, C. M. Gabrys, T. Oka, B. J. Cotterell, R. J. Stickland, C. Jungen, and A.

       Wuest, Journal of Chemical Physics **113** (22), 10143 (2000).

16   S. Fredin, D. Gauyacq, M. Horani, C. Jungen, G. Lefevre, and F.

       Masnouseeuws, Molecular Physics **60** (4), 825 (1987).

17   M. Raoult, Journal of Chemical Physics **87** (8), 4736 (1987).

18   S. T. Pratt, C. Jungen, and E. Miescher, Journal of Chemical Physics **90** (11),

       5971 (1989).

19   D. T. Biernacki, S. D. Colson, and E. E. Eyler, Journal of Chemical Physics **88**

       (4), 2099 (1988).

20   E. Miescher, Canadian Journal of Physics **49**, 2350 (1971).

21   K. P. Huber, M. Vervloet, C. Jungen, and A. L. Roche, Molecular Physics **61**

       (2), 501 (1987).

22   M. Hiyama and M. S. Child, Journal of Physics B-Atomic Molecular and

       Optical Physics **36** (22), 4547 (2003).

23   M. Hiyama and M. S. Child, Journal of Physics B-Atomic Molecular and

       Optical Physics **35** (5), 1337 (2002).

24   C. Jungen, K. P. Huber, M. Jungen, and G. Stark, Journal of Chemical Physics

       118 (10), 4517 (2003).

25   E. Miescher, Files held in Paris by Ch. Jungen at the Universite Paris-sud,

       Laboratoire Aimee Cotton.

Chapter 6. Concluding remarks.

6.1. Summary of results

The work presented in this thesis represents the first experiments aimed at observing the decay of a Rydberg wave packet into chemically different channels. It also represents the first experimental implementation of coherent control over both the composition, and chemistry of a molecular Rydberg wave packet. We also present the basis of a complete theoretical description of the Rydberg series of the NO molecule.

In chapter 3 an experiment to control the rotational angular momentum of a Rydberg electron wave packet in NO was presented. The control mechanism was designed from the outset, with knowledge of the phase evolution of the two core rotational states contained within the wave packet. When the two core rotational states had a phase difference of π, a second pulse could be used to dump one or other core state down to the launch state, thus leaving a wave packet of pure rotational character. This was demonstrated experimentally by looking at the evolution of the wave packet following the pulse pair. When the wave packet contained one or other core state they demonstrated quite different recurrence times, and were easily distinguishable. The efficiency of the control mechanism was calculated by looking at the population

129

distribution of the wave packet following the pulse sequence, which proved the control mechanism was extremely effective with almost no remaining population from the dumped rotational state.

In chapter 4 we presented the first experimental observation of a dissociating Rydberg electron wave packet. The detection method employed a three-colour REMPI technique combined with the optical Ramsey method. The dynamics detected where hydrogenic as the wave packets contained a single $p(N)$ Rydberg series, where N is the rotational angular momentum of the ion core. This is in contrast to the autoionising dynamics, which show interference effects due to the mixed character of the wave packet; the autoionising wave packet contained both a $p(N)$ series and a $f(N+2)$ series. From these time-resolved experiments we can see that the p series dissociate and ionise, while the f states only ionise. An intuitive control scheme manipulating the ionisation/dissociation ratio has also been demonstrated. The scheme utilises the relative decay rates of the two angular momentum components contained within the wave packet. By selectively populating one or other angular momentum state it is possible to alter which bond is broken preferentially i.e. the N-O bond or the NO^+-e^- bond.

In chapter 5 an MQDT representation of the Rydberg states of NO was derived. The work represents the most complete description of NO to date, but does contain some simplifications. Most notably the valence state interactions have been left out and the continuum has also been neglected. The work does however contain all Rydberg series with $\ell \leq 3$ and all series interactions documented. The s-d interaction is extremely strong, while other weaker interaction show local importance. The final calculation provide an excellent theoretical description of the Rydberg states of NO with a residual error of ~ 1 cm^{-1}.

6.2 Future possibilities

6.2.1 Predissociation and autoionisation

The control scheme presented in chapter 4 does not allow complete control over the ionisation/dissociation ratio. By building an MQDT framework that includes the two competing processes, it should be possible to design from first principles a control scheme which allows either process to be stopped selectively. Chapter 5 represents the first step in this process, by calculating the quantum defect matrix we have also calculated the energy and Rydberg wavefunctions of over 5,000 levels which will become important when extending this work to coherent control. The next step involves the inclusion of the continuum and the valence states, this will allow the ionisation and dissociation process to be included in the description. As a final step the transition dipoles will be calculated between the ground and first excited state, and between the first excited states and the Rydberg states, this will then allow direct comparisons with our experimental results of both the autoionising and predissociating states of NO.

6.2.2 Interseries couplings

The MQDT analysis has also shown how important interseries couplings can be. Having designed a scheme that selectively populates one of two uncoupled series, it is tempting next to design a coherent control scheme which can decouple two series. A number of candidates are available for these experiments, the s and d series in NO [1], N_2 [2] are strongly coupled and a sound MQDT basis exists for both. Each possibility however has its own drawbacks, these are, either low transition dipoles or extremely

short wavelengths required to access the Rydberg states. A strong coupling also exists between the $p(1)$ and $p(3)$ Rydberg series of BH [3], but very little MQDT analysis has been done on this system so far. Despite these difficulties experiments to uncouple states will be the next major step in the control of molecular Rydberg wave packets, and should lead to a greater insight into the more complex waveforms obtained in feedback controlled experiments.

6.2.3 Bound states

We have also recorded frequency spectra of the bound states of NO via the $\left| v = 0, N = 0,1,2 \right\rangle$ levels of the A-state [4]. By moving to a region of the spectrum where dissociation is the only decay path open to the electron, we should be able to design a simple control scheme to stop this channel. The pulsed field ionising spectra however, showed some quite unexpected results with the p Rydberg series not being detected, presumably due to fast predissociation. The f states therefore dominate the spectra obtained. Other coherent control experiments therefore come to mind. Excitation via the $\left| v = 0, N = 2 \right\rangle$ level of the A-state gave a spectrum containing $f(0)$, $f(2)$ and $f(4)$ Rydberg series. Having controlled the composition of a wave packet containing two series, it is tempting to try and produce the same control over a wave packet containing three series. However, this proves harder than at first would be thought, and no intuitive pulse sequence could be calculated. A genetic algorithm developed within the group was then used to find the optimal solution to this problem. The pulse sequence is then compared with the fundamental motions of the wave packet to see if any intuitive arguments could be derived from the output. The output from the algorithm contained a

sequence of three pulses with specific time and phase relationships between them; the analysis of the pulse sequence is currently ongoing with the corresponding experiments to be done at a later date. In these experiments the control efficiency will be measured experimentally using state selective field ionisation, this allows one to directly measure the population of each Rydberg state removing the need to calculate this separately.

6.3 References

1   S. Fredin, D. Gauyacq, M. Horani, C. Jungen, G. Lefevre, and F. Masnouseeuws, Molecular Physics **60** (4), 825 (1987).

2   C. Jungen, K. P. Huber, M. Jungen, and G. Stark, Journal of Chemical Physics **118** (10), 4517 (2003).

3   A. T. Gilkison, C. R. Viteri, and E. R. Grant, Physical Review Letters **92** (17), 173005 (2004).

4   R. S. Minns, R. Patel, and H. H. Fielding, Unpublished work (2004).